Quantum criticality and superconductivity in the electron nematic FeSe$_{1\text{-}x}$S$_x$

Salvatore Licciardello

Printed by Ipskamp Printing, Enschede, the Netherlands, 2019

ISBN: 978-94-028-1605-1

Cover design by Salvatore and Daniela Licciardello

QUANTUM CRITICALITY AND SUPERCONDUCTIVITY IN THE ELECTRON NEMATIC $\mathrm{FeSe}_{1\text{-}x}\mathrm{S}_x$

PROEFSCHRIFT

ter verkrijging van de graad van doctor
aan de Radboud Universiteit Nijmegen
op gezag van de rector magnificus prof. dr. J.H.J.M. van Krieken,
volgens besluit van het college van decanen
in het openbaar te verdedigen op maandag 30 september 2019
om 16:30 uur precies

door

SALVATORE LICCIARDELLO

geboren op 24 mei 1989
te Catania, Italië

Promotor: Prof. dr. Nigel E. Hussey

Manuscriptcommissie:

Prof. dr. Alexey V. Kimel

Prof. dr. Jörg Schmalian
(Karlsruher Institut für Technologie, Duitsland)

Dr. Benoît Fauqué
(ESPCI Parijs, Frankrijk)

Het werk beschreven in dit proefschrift is uitgevoerd aan de faculteit der Natuurwetenschappen, Wiskunde en Informatica van de Radboud Universiteit Nijmegen en maakt deel uit van het onderzoekprogramma van de Stichting voor Fundamenteel Onderzoek der Materie (FOM), die deel uitmaakt van de Nederlandse Organisatie voor Wetenschappelijk Onderzoek (NWO)

QUANTUM CRITICALITY AND SUPERCONDUCTIVITY IN THE ELECTRON NEMATIC $FeSe_{1-x}S_x$

DOCTORAL THESIS

to obtain the degree of doctor
from Radboud University Nijmegen
on the authority of the rector magnificus prof. dr. J.H.J.M. van Krieken,
according to the decision of the council of deans
to be defended in public on Monday, September 30, 2019
at 16:30 hours

by

SALVATORE LICCIARDELLO

born on May 24, 1989
in Catania, Italy

Supervisor: Prof. dr. Nigel E. Hussey

Doctoral Thesis Committee:

Prof. dr. Alexey V. Kimel

Prof. dr. Jörg Schmalian
(Karlsruhe Institute of Technology, Germany)

Dr. Benoît Fauqué
(ESPCI Paris, France)

The work described in this doctoral thesis was carried out at the Faculty of Natural Sciences, Mathemathics and Informatics of the Radboud University in Nijmegen and is part of the research programme of the Foundation for Fundamental Research on Matter (FOM), which is part of the Dutch Research Council (NWO)

A Loredana e Nino

Contents

CHAPTER 1

Introduction

Fe-based superconductors (FBS) form nowadays a well established field in condensed matter physics. Shortly after the discovery of superconductivity (SC) below 3.2 K in LaOFeP over a decade ago by Hideo Hosono and co-workers [1], chemical doping was employed by the same scientific group to obtain a dome-like superconducting phase in La($O_{1\text{-}x}F_x$)FeAs [2], with the superconducting transition temperature T_c peaking at 26 K. Since then, many families of Fe-based compounds have been investigated in the hunt for materials that superconduct at even higher temperatures and in an effort to gain a better understanding of the mechanisms of high-T_c superconductivity.

The crystal structure of FBS consists of corrugated layers of Fe-A atoms, where A can be either As or a chalcogen, which then stack vertically along the crystallographic c-axis (Fig. 1.1a). What makes FBS particularly interesting is the high tunability of their superconducting properties by simply *adding* different atoms or groups of atoms in between those layers. Moreover, a common feature in FBS is the complex interplay of different forms of ordered phases, such as antiferromagnetism (AFM), charge (spin) density waves (C(S)DW), together with structural and possibly Fermi surface (FS) distortions [3]. These phases and their mutual relations can be tuned by changing a control parameter g – e.g. applied pressure, magnetic field, chemical composition/doping. It is customary that SC emerges from AFM when the latter is sufficiently suppressed upon tuning g (Fig. 1.1b). The antiferromagnetic state is usually anisotropic in the plane and exists in an orthorhombic lattice, but it would be erroneous to link the lattice distortion to the magnetic transition. Indeed, in many materials the tetragonal-to-orthorhombic structural transition is clearly decoupled from the magnetic transition, as the two occur at two fairly distinct temperatures, T_s and T_m respectively [4–8]. These experimental findings strongly suggest that the structural transition is actually related to another form of symmetry breaking – namely a rotational symmetry breaking or a *nematic* order – as sketched in Fig. 1.1b, which onsets at T_s [9–11].

Classical nematics are generally found in systems of oblong molecules which, under certain conditions, can orient along preferential axes thereby generating spacial anisotropy. Such anisotropy is, for example, the basic working principle of liquid crystal displays that were responsible for a major breakthrough in modern technology.
Similarly, in condensed matter physics, strong transport anisotropies measured in two-dimensional electron systems in high magnetic fields [12, 13] as well as in a variety of other families of materials such as ruthenates [14], Fe-pnictides [15], cuprates [16] and heavy-fermions [17], have been ascribed

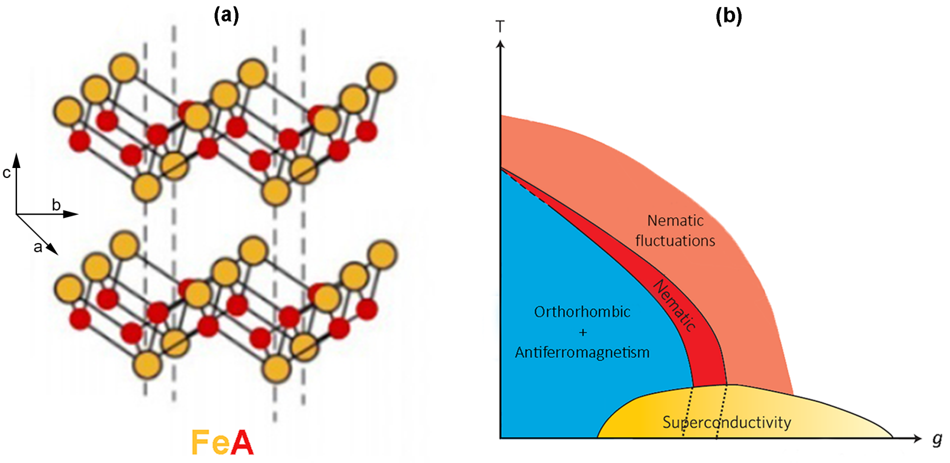

Figure 1.1: Crystal structure and phase diagram of a typical Fe-based superconductor. *(a) (from ref. [3]) Basic atomic arrangement in a FBS. The Fe-A layers form the basic crystal structure of a FBS. (b) (adapted from ref. [11]) The T vs. g phase diagram of a model FBS. Upon tuning the control parameter g, the interplay between the different phases can be explored.*

to the presence of a nematic electron fluid [18–20]. An electron nematic is often defined as a unidirectional self-organized state [21].

In many of the above mentioned materials though, nematicity is often intertwined at low temperatures with other forms of order, which naturally hinder a study of nematicity itself. An exception in this respect is represented by FeSe, in which nematic order appears in isolation. Therefore, FeSe offers an unprecedented experimental opportunity to study this mysterious form of order and the possible role of nematic fluctuations in mediating the superconducting pairing. This thesis is devoted to a detailed transport study of a family of S-doped FeSe single crystals.

A quadratic temperature dependence of the limiting low-T resistivity (ρ) is the expected form for a correlated Fermi-liquid, where electron-electron scattering is the dominant scattering mechanism. However, deviations from this classical behaviour have been reported in a number of materials. A T-linear ρ has been observed, for instance, in cuprates [22–24], organic compounds [25], ruthenates [26, 27], heavy-fermions [28, 29] and FBS [30, 31]. Those harbouring such non-Fermi-liquid behaviour are usually referred to as *strange metals*. More precisely, such a system can maintain its T-linear ρ over a broad, usually fan-shaped portion of its phase diagram centred around a specific value of the control parameter g_c. This situation, sketched in Fig. 1.2a, is often interpreted in the general framework of quantum criticality [32–34].

Classical phase transitions are usually governed by thermal fluctuations, which induce some form of long-range order when the critical temperature is reached. In contrast, a *quantum* phase transition happens at zero temperature in which case, a system is tuned by the non-thermal control parameter g, to undergo a transition at the quantum critical point (QCP) g_c. Theory has predicted [35] and experiments have demonstrated [36] that it is the interplay of quantum and thermal fluctuations that leads to the characteristic fan-shaped quantum critical region that can extend up to considerably high temperatures [37].

For strongly correlated electrons, a QCP can be obtained when g-tuning depresses the onset temperature of a certain ordered phase (spin-, charge-, or orbital-like) to 0 K. In FBS, this ordered phase is usually of magnetic origin (e.g. AFM, SDW). A prominent example of this is the Fe-pnictide system $BaFe_2(As_{1-x}P_x)_2$ [30, 31, 38]. As shown in Fig. 1.2b, the end point of the line of transitions to the SDW phase lies beneath a dome of SC. The

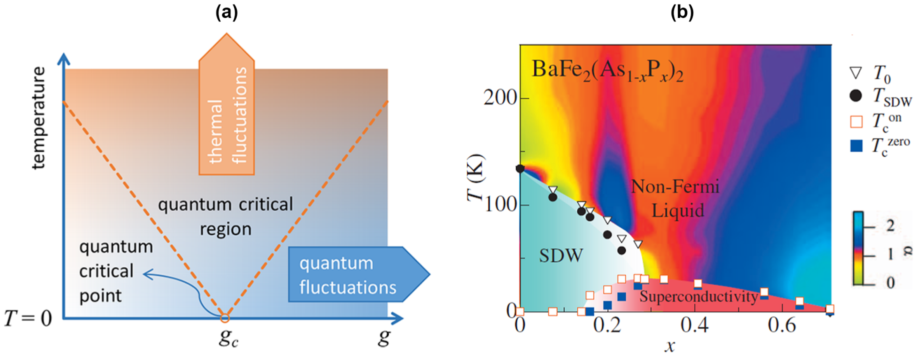

Figure 1.2: Quantum criticality. *(a) (from ref. [37]) Sketch of a model quantum critical phase transition. (b) (from ref. [30]) Phase diagram of* $BaFe_2(As_{1-x}P_x)_2$*.* T_0 *and* T_{SDW} *are the structural transition temperature and the SDW transition temperature, respectively.* T_c^{on} *is the onset temperature of SC and* T_c^{zero} *is the zero resistivity temperature. The color scale represents the temperature exponent of the resistivity* α*, according to the equation* $\rho(T) = \rho_0 + T^{\alpha}$*. Note the similarity with the paradigmatic phase diagram in (a), if one replaces* g_c *with* $x_c \approx 0.3$.

mutual interplay between SDW and SC is attested by the peak in T_c at $x_c \approx 0.3$, the same doping level at which the SDW transition temperature is suppressed to zero. Transport measurements in high magnetic fields have uncovered the existence of a quantum critical fan of T-linear ρ (see color map of Fig. 1.2b), indicative of a QCP right at x_c. Although large nematic fluctuations have been reported in $BaFe_2(As_{1-x}P_x)_2$ and are enhanced when approaching the QCP [39, 40], suggesting that there might be a nematic QCP very close to – if not coinciding with – the magnetic QCP, a consensus has been reached in the community that quantum criticality in the pnictides is due to magnetic fluctuations.

In contrast to e.g. $BaFe_2(As_{1-x}P_x)_2$, in $FeSe_{1-x}S_x$ there is no real maximum in T_c at the putative QCP [41], suggesting that the type of quantum criticality in this system is of a different nature. In light of this, S substituted FeSe has emerged as a candidate for a purely nematic form of quantum criticality, as will be explored in the course of this dissertation.

Specifically, this thesis is divided into two parts. The first part contains two chapters and is meant to set the scene for the rest of the book. Chap. 2 contains an overview on FeSe and $FeSe_{1-x}S_x$, materials which will be experimentally studied in the last three chapters of this manuscript. The basic chemical and physical properties of this family of materials are discussed, based on an up-to-date body of work from the literature. In Chap. 3, the experimental techniques for growth, characterization and electrical transport measurements in (high) magnetic fields used to perform our experiments are presented.

The second part of this thesis consists of three experimental chapters. In Chap. 4, the low-temperature resistive state of $FeSe_{1-x}S_x$ will be explored while suppressing the superconducting state by means of strong in-plane dc magnetic fields. Measurements revealing the evolution of the form of the low-T resistivity as a function of sulphur concentration x will be discussed. Strong evidence for a purely nematic QCP at a $x_c \approx 0.16$ will be presented. The magnetoresistance induced in the materials series when applying transverse magnetic fields will be studied in Chap. 5. Its non-conventional form will be analysed and compared to similar observations in other materials studied in the literature. In particular, a composite magnetoresistance containing both a conventional and a *quantum critical* component, will be exposed. The findings of Chap. 4 and 5 collectively provide a snap-shot of the effects of (nematic) quantum criticality on the electrical transport properties of $FeSe_{1-x}S_x$. Finally, Chap. 6 will focus on the mechanisms whereby superconductivity is destroyed in $FeSe_{1-x}S_x$ under both in-plane and transverse applied magnetic fields. The temperature and S-doping dependence of the relevant field scales will be systematically studied and the possible presence of a quantum vortex liquid state, developing at high x values, will be argued.

References

[1] Y. Kamihara *et al.*, *J. Am. Chem. Soc.* **128** 31, pp. 10012–10013 (2006).

[2] Y. Kamihara *et al.*, *J. Am. Chem. Soc.* **130** 11, pp. 3296–3297 (2008).

[3] A. E. Böhmer and A. Kreisel, *J. Phys. Condens. Matter* **30** 023001 (2018).

[4] C. De La Cruz *et al.*, *Nature* **453**, pp. 899–902 (2008).

[5] N. Ni *et al.*, *Phys. Rev. B* **80** 024551 (2009).

[6] D. R. Parker *et al.*, *Phys. Rev. Lett.* **104** 057007 (2010).

[7] P. C. Canfield and S. L. Bud'ko, *Annu. Rev. Condens. Matter Phys.* **1**, pp. 27–50 (2010).

[8] M. G. Kim *et al.*, *Phys. Rev. B* **83** 134522 (2011).

[9] R. M. Fernandes *et al.*, *Phys. Rev. B* **85** 024534 (2012).

[10] R. M. Fernandes and J. Schmalian, *Supercond. Sci. Technol.* **25** 084005 (2012).

[11] R. M. Fernandes, A. V. Chubukov and J. Schmalian, *Nat. Phys.* **10**, pp. 97–104 (2014).

[12] M. P. Lilly *et al.*, *Phys. Rev. Lett.* **82** 2, pp. 394–397 (1999).

[13] R. R. Du *et al.*, *Solid State Commun.* **109**, pp. 389–394 (1999).

[14] R. A. Borzi *et al.*, *Science* **315**, pp. 214–217 (2007).

[15] J.-H. Chu *et al.*, *Science* **329**, pp. 824–826 (2010).

[16] Y. Ando *et al.*, *Phys. Rev. Lett.* **88** 137005 (2002).

[17] F. Ronning *et al.*, *Nature* **548**, pp. 313–317 (2017).

[18] S. Kivelson, E. Fradkin and V. Emery, *Nature* **393**, pp. 550–553 (1998).

[19] E. Fradkin and S. A. Kivelson, *Phys. Rev. B* **59** 12, pp. 8065–8072 (1999).

[20] S. A. Kivelson *et al.*, *Rev. Mod. Phys.* **75** 4, pp. 1201–1241 (2003).

[21] S. Kasahara *et al.*, *Nature* **486**, pp. 382–385 (2012).

[22] R. A. Cooper *et al.*, *Science* **323**, pp. 603–607 (2009).

[23] N. E. Hussey *et al.*, *J. Phys. Conf. Ser.* **449** 012004 (2013).

[24] A. Legros *et al.*, *Nat. Phys.* **15**, pp. 142–147 (2019).

[25] N. Doiron-Leyraud *et al.*, *Phys. Rev. B* **80** 214531 (2009).

[26] S. A. Grigera *et al.*, *Science* **294**, pp. 329–332 (2001).

[27] J. A. N. Bruin *et al.*, *Science* **339**, pp. 804–807 (2013).

[28] H. v. Löhneysen *et al.*, *Phys. Rev. Lett.* **72** 20, pp. 3262–3265 (1994).

[29] J. Custers *et al.*, *Nature* **424**, pp. 524–527 (2003).

[30] S. Kasahara *et al.*, *Phys. Rev. B* **81** 184519 (2010).

[31] J. G. Analytis *et al.*, *Nat. Phys.* **10**, pp. 194–197 (2014).

[32] S. Sachdev, *Quantum Phase Transitions*, Cambridge University Press (1998).

[33] S. Sachdev and B. Keimer, *Phys. Today* **64** 2, p. 29 (2011).

[34] P. Coleman and A. J. Schofield, *Nature* **433**, pp. 226–229 (2005).

[35] A. Kopp and S. Chakravarty, *Nat. Phys.* **1** 53 (2005).

[36] A. W. Kinross *et al.*, *Phys. Rev. X* **4** 031008 (2014).

[37] M. Klanjšek, *Physics* **7** 74 (2014).

[38] T. Shibauchi, A. Carrington and Y. Matsuda, *Annu. Rev. Condens. Matter Phys.* **5**, pp. 113–135 (2014).

[39] H.-H. Kuo *et al.*, *Science* **352** 6288, pp. 958–962 (2016).

[40] M. Yoshizawa *et al.*, *J. Phys. Soc. Japan* **81** 024604 (2012).

[41] S. Hosoi *et al.*, *Proc. Natl. Acad. Sci. USA* **113** 29, pp. 8139–8143 (2016).

I

$\text{FeSe}_{1-x}\text{S}_x$: LITERATURE SURVEY AND INVESTIGATIONS IN HIGH MAGNETIC FIELDS

CHAPTER 2

State of the art

2.1 FeSe

Among FBS, much recent attention has been focussed on the iron monochalcogenide FeSe [1], especially because of its highly tunable T_c. The modest value of ~8-9 K under ambient conditions can be driven up to nearly 40 K under applied pressures above 6 GPa [2–4]. Ionic gating [5] and chemical intercalation with appropriate molecules [6] have the (indirect) effect of increasing the carrier density and can yield a T_c of around 43 K. As of today, the record superconducting transition temperature in FeSe has been achieved in monolayers grown on doped $SrTiO_3$, with reported T_c values in excess of 100 K [7].

As in other FBS (see Chap. 1), above T_s the layered structure of FeSe is arranged in a tetragonal lattice, as displayed in Fig. 2.1a, with the Fe-Se sheets conventionally assigned within the *ab* planes. According to band structure calculations [8, 9], the FS of FeSe comprises five cylindrical pockets (three hole- and two electron-like). However, three independent studies of quantum oscillations (QOs) [9–11] found only four fundamental frequencies and angle-resolved photoemission spectroscopy (ARPES) [9] measured pockets that are smaller than predicted, suggesting that the theoretical models were not accurate. Further details on this issue, along with a comparison with our own experimental results, will be discussed in Chap. 4.

At $T_s \approx 90\,\mathrm{K}$, the system undergoes a transition to an orthorhombic lattice [1, 12] and ρ exhibits a kink [13] (see Fig. 2.1b). Thermodynamic measurements have reported a second-order jump in the specific heat at T_s [14, 15]. The nematic character of this transition has been provided by elasto-resistance experiments, through which a finite nematic susceptibility was observed [16]. This quantity, describing the development of a resistive anisotropy between a and b when strain is applied, diverges at T_s [9], reflecting the onset of long-range nematic order. Moreover, ARPES experiments have unveiled a splitting of the bands with d_{xz} and d_{yz} orbital character below T_s [9, 17–20]. Dramatic distortions of the FS, which transforms from four- to two-fold symmetry, with the hole and especially the electron pockets becoming much elongated, have also been reported [9, 21]. These phenomena are manifestations of so-called orbital order.

The findings listed above, summarized in Fig. 2.1b, strongly support the existence of an electron nematic phase in bulk FeSe below T_s. Although there is no long-range magnetic order in FeSe at ambient pressure, evidence for magnetic fluctuations has been reported in the literature. The muon-spin rotation (μSR) depolarization rate has been found to exhibit quantum critical behaviour between ~10-20 K and T_s [22]. This is attributed to magnetic fluctuations possibily due to the close proximity to a pressure-induced magnetic QCP. In fact, high pressure experiments involving μSR [23], nuclear magnetic resonance (NMR) [24], magnetotransport [25, 26] and ac magnetization [23, 25], have all confirmed the emergence of a magnetically ordered phase under pressure (p). As shown in the leftmost plot of Fig. 2.3, the T vs. p phase diagram of FeSe reveals interesting correlations between T_c, T_s and the magnetic ordering temperature T_m. The nematic phase is quickly suppressed with increasing pressure and it has essentially disappeared by 2 GPa. SC experiences a modest enhancement at low pressures, but remains roughly constant in the interval 2-5 GPa. In that same pressure range, a dome-shaped SDW phase emerges below a temperature T_m which reaches its maximum at ~4 GPa. Above 6 GPa, T_m is suppressed and T_c is strongly enhanced.

The high tunability of T_c suggests that superconductivity in FeSe is of unconventional origin. In fact, SC has been reported to be multi-band and anisotropic. For example, specific-heat studies have measured up to three different SC gaps (Δ), all anisotropic in momentum space [27]. Recent ARPES [28–31] and scanning tunnelling microscopy (STM) [32, 33] experiments have led to the proposal that pairing in FeSe does not involve all quasiparticles, but is weighted by the orbital character and predominantly involves d_{yz} orbitals. The existence of an anisotropic Δ

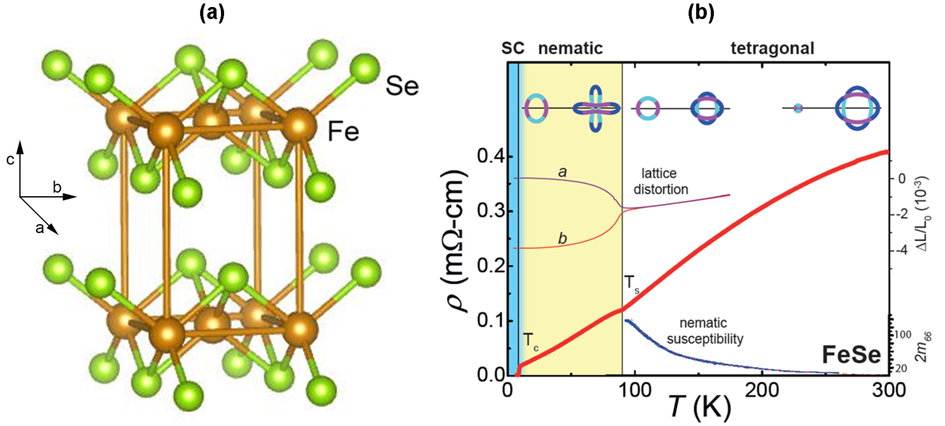

Figure 2.1: Crystal structure and electronic properties of FeSe. *(a) Schematic drawing of the crystal structure of FeSe showing the Fe (light brown) – Se (green) layers stacked along the c-axis. (b) (adapted from ref. [38]) The temperature dependence of the resistivity of FeSe. The kink at* $T_s \approx 90\,\mathrm{K}$ *and the superconducting transition at* $T_c = 8.5\,\mathrm{K}$ *are visible. In the insets, from top to bottom: a sketch of the FS distortion in the nematic state, the change in the lattice parameters a and b after the tetragonal to orthorhombic structural transition (quantified by the ralative distortion* $\Delta L/L_0$*) and the trend of the nematic susceptibility in terms of the elasto-resistivity coefficient* $2m_{66}$*.*

might as well be due to nematic order, which mixes s-wave and d-wave pairing channels giving rise to the observed anisotropy [34]. However, it is interesting to note that the suppression of the nematic phase – for example by S substitution for Se – has little influence on the magnitude of T_c, as will be discussed in the following sections of this chapter. Although there is no consensus yet on the origin of the anisotropy of Δ in FeSe, a proposal has been advanced that microscopic regions where SC has different structures can coexist in the same bulk sample [35]. This idea is reinforced by the observation of sizeable variations in T_c (between 3-9 K) in samples prepared with slightly different starting compositions and growth parameters [36]. Furthermore, a detailed STM study [37] has reported a sign change in Δ in proximity of orthorhombic domain boundaries, supporting the notion that distinct forms of SC at the microscopic level can coexist in bulk FeSe.

2.2 $FeSe_{1-x}S_x$

FeSe also provides the basic building block of a class of new materials obtained by substituting other elements for Fe or Se. The most common substitutions are Co and Ni for Fe and Te and S for Se. T_s is suppressed with doping in all four cases, while T_c is suppressed only in $Fe_{1-x}Co_xSe$ and $Fe_{1-x}Ni_xSe$ [39]. An enhancement of T_c of up to 75% was achieved with substitution of Te for Se; however, the difficulty of growing $FeSe_{1-x}Te_x$ with low Te content makes it hard to study the evolution from the parent compound continuously. Substitution of S for Se in $FeSe_{1-x}S_x$ has little effect on T_c and does cause a marked suppression of T_s, thereby generating an interesting phase diagram in which the evolution of nematicity with S content x, and possibly its interplay with SC, can be explored in the absence of concomitant magnetic order.

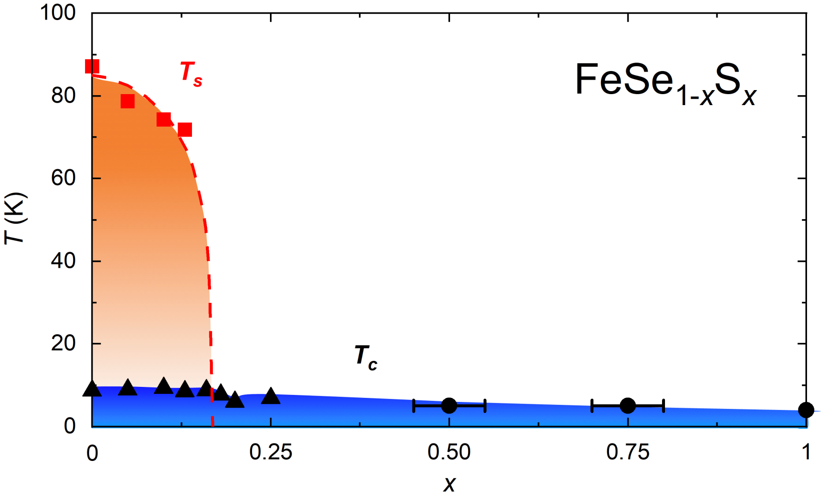

Figure 2.2: The temperature vs. S content phase diagram of $FeSe_{1-x}S_x$. *The values of T_s (red squares) and T_c (black triangles) up to $x = 0.25$ are obtained from the transport experiments presented in this thesis. The values of T_c for $x = 0.5$, 0.75 and for pure FeS (black circles) are reproduced from ref. [40]. The color shades are guides to the eye.*

2.2.1 Evolution of the nematic and superconducting phases

The progressive suppression of the nematic phase of FeSe due to S substitution has been reported via several independent experimental probes. Therefore, the evolution of T_s with increasing S content x can be robustly determined.

Standard electric transport measurements have shown that the kink in the temperature dependence of ρ is shifted to progressively lower temperatures as x grows, until it disappears at $x \approx 0.16$ [41–44] as displayed in Fig. 2.2, implying that $T_\mathrm{s} = 0\,\mathrm{K}$ and the nematic phase is entirely suppressed. Elastoresistance studies on $\mathrm{FeSe}_{1\text{-}x}\mathrm{S}_x$ crystals over a broad range of x could follow the peak at T_s until its disappearance at $x \approx 0.16$ [42]. The temperature at which the orbital order is suppressed has been measured by ARPES at different x values [45]. More specifically the amplitude of the splitting of the d_{xz} and d_{yz} bands, extracted from the energy distribution curves, and the elongation of the electron pocket, defined as the deviation of the Fermi wavevector from its value in the tetragonal phase, both begin to assume finite values below T_s. For $x \geq 0.16$ these parameters are zero down to the lowest temperatures studied.

ARPES and QOs have also tracked the evolution of the electronic structure as a function of x and T, both inside and outside the nematic phase [40, 44, 45]. The size of Fermi pockets and the Fermi velocities increase with increasing x outside of the nematic phase, indicating the suppression of electron correlations. Correlations are also found to be strongest inside the nematic phase itself.

In contrast to the striking evolution of the nematic phase with S substitution, the superconducting phase seems to be relatively insensitive to changes in x. SC persists throughout the entire series from FeSe to FeS with T_c diminishing only by a factor of two at high S concentrations (see Fig. 2.2), implying the lack of a superconducting dome that is characteristic of other FBS. Nevertheless, the existence of two distinct superconducting gap structures, separated by the nematic end point, has been demonstrated through measurements of both specific heat and thermal conductivity [43]. A recent STM study [46] has revealed that the gap magnitude falls abrutply to half of its value beyond a sulphur content of ~16%.

2.2.2 *Effects of applied pressure*

The magnetic fluctuations present in pure FeSe have been reported to become weaker with sulphur substitution [48]. The combination of *chemical* pressure induced by S substitution x and physical pressure p helps to gain a more complete picture in this regards, and generates an interesting set of phase diagrams (see Fig. 2.3). In particular, as already discussed above for pure FeSe, pressure reveals that $FeSe_{1-x}S_x$ lies in close proximity to a SDW phase. The nematic transition temperature T_s, already suppressed by increasing x, gets weakened further with increasing p. The magnetically ordered phase emerging at high pressure in FeSe appears to become progressively narrower as x increases. As a consequence, the nematic and magnetic phases, initially overlapping in the p-T plane for a certain pressure range, shift in opposite p directions and eventually decouple from one another as x increases [47]. The superconducting transition temperature T_c has a

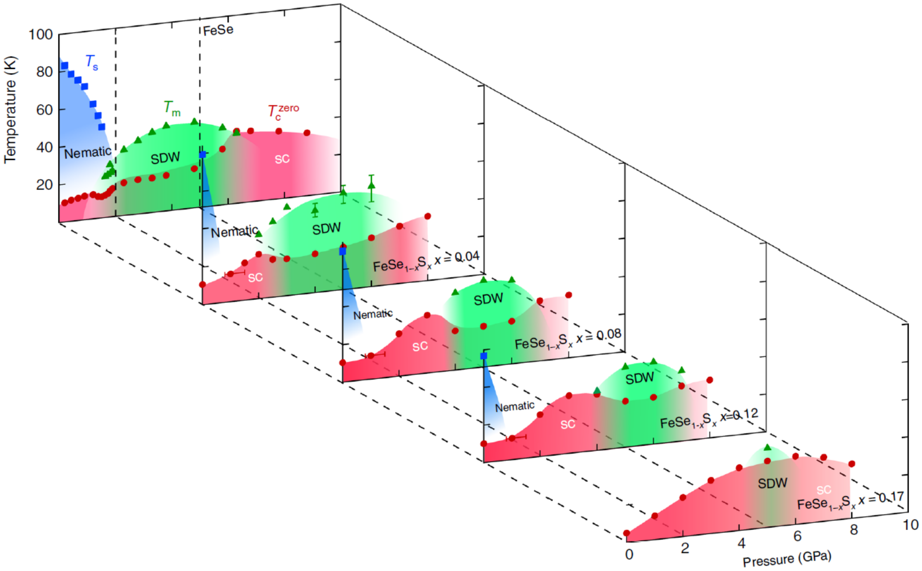

Figure 2.3: Temperature vs. pressure phase diagrams of $FeSe_{1-x}S_x$ for a selection of x values. *(from refs. [26, 47]) The five plots show the evolution of the nematic ordering temperature T_s (blue squares), the magnetic ordering temperature T_m (green triangles) and the superconducting transition temperature T_c (red circles) with increasing pressure for $x = 0,\ 0.04,\ 0.08,\ 0.12$ and 0.17. The color shades are guides to the eye.*

local minimum whenever the magnetic ordering temperature T_{m} has its maximum value, implying that magnetic order has a detrimental effect on SC. Therefore, chemical and physical pressure can together tune the temperature scales governing the different forms of order appearing in $\mathrm{FeSe}_{1\text{-}x}\mathrm{S}_x$, thus providing a powerful experimental handle to study their evolution and mutual interplay.

References

[1] F.-C. Hsu *et al.*, *Proc. Natl. Acad. Sci. USA* **105** 38, pp. 14262–14264 (2008).

[2] S. Medvedev *et al.*, *Nat. Mater.* **8**, pp. 630–633 (2009).

[3] H. Okabe *et al.*, *Phys. Rev. B* **81** 205119 (2010).

[4] J. P. Sun *et al.*, *Phys. Rev. Lett.* **118** 147004 (2017).

[5] B. Lei *et al.*, *Phys. Rev. Lett.* **116** 077002 (2016).

[6] M. Burrard-Lucas *et al.*, *Nat. Mater.* **12**, pp. 15–19 (2013).

[7] J.-F. Ge *et al.*, *Nat. Mater.* **14**, pp. 285–289 (2015).

[8] J. Maletz *et al.*, *Phys. Rev. B* **89** 220506(R) (2014).

[9] M. D. Watson *et al.*, *Phys. Rev. B* **91** 155106 (2015).

[10] T. Terashima *et al.*, *Phys. Rev. B* **90** 144517 (2014).

[11] A. Audouard *et al.*, *Europhys. Lett.* **109** 27003 (2015).

[12] S. Margadonna *et al.*, *Chem. Commun.* pp. 5607–5609 (2008).

[13] T. M. McQueen *et al.*, *Phys. Rev. Lett.* **103** 057002 (2009).

[14] A. E. Böhmer *et al.*, *Phys. Rev. Lett.* **114** 027001 (2015).

[15] S. Karlsson *et al.*, *Supercond. Sci. Technol.* **28** 105009 (2015).

[16] J.-H. Chu *et al.*, *Science* **337**, pp. 710–712 (2012).

[17] T. Shimojima *et al.*, *Phys. Rev. B* **90** 121111(R) (2014).

[18] P. Zhang *et al.*, *Phys. Rev. B* **91** 214503 (2015).

[19] Y. Suzuki *et al.*, *Phys. Rev. B* **92** 205117 (2015).

[20] Y. Zhang *et al.*, *Phys. Rev. B* **94** 115153 (2016).

[21] M. D. Watson *et al.*, *New J. Phys.* **19** 103021 (2017).

[22] V. Grinenko *et al.*, *Phys. Rev. B* **97** 201102(R) (2018).

[23] M. Bendele *et al.*, *Phys. Rev. Lett.* **104** 087003 (2010).

[24] P. Wiecki *et al.*, *Phys. Rev. B* **96** 180502(R) (2017).

[25] T. Terashima *et al.*, *J. Phys. Soc. Japan* **84** 063701 (2015).

[26] J. P. Sun *et al.*, *Nat. Commun.* **7** 12146 (2016).

[27] Y. Sun *et al.*, *Phys. Rev. B* **96** 220505(R) (2017).

[28] T. Hashimoto *et al.*, *Nat. Commun.* **9** 282 (2018).

[29] Y. S. Kushnirenko *et al.*, *Phys. Rev. B* **97** 180501(R) (2018).

[30] D. Liu *et al.*, *Phys. Rev. X* **8** 031033 (2018).

[31] L. C. Rhodes *et al.*, *Phys. Rev. B* **98** 180503(R) (2018).

[32] L. Jiao *et al.*, *Sci. Rep.* **7** 44024 (2017).

[33] P. O. Sprau *et al.*, *Science* **357**, pp. 75–80 (2017).

[34] J. Kang, R. M. Fernandes and A. Chubukov, *Phys. Rev. Lett.* **120** 267001 (2018).

[35] A. E. Böhmer and A. Kreisel, *J. Phys. Condens. Matter* **30** 023001 (2018).

[36] A. E. Böhmer and C. Meingast, *C. R. Physique* **17**, pp. 90–112 (2016).

[37] T. Watashige *et al.*, *Phys. Rev. X* **5** 031022 (2015).

[38] A. I. Coldea and M. D. Watson, *Annu. Rev. Condens. Matter Phys.* **9**, pp. 125–146 (2018).

[39] Y. Mizuguchi *et al.*, *J. Phys. Soc. Japan* **78** 074712 (2009).

[40] P. Reiss *et al.*, *Phys. Rev. B* **96** 121103(R) (2017).

[41] T. Urata *et al.*, *arXiv* **1608.01044** (2016).

[42] S. Hosoi *et al.*, *Proc. Natl. Acad. Sci. USA* **113** 29, pp. 8139–8143 (2016).

[43] Y. Sato *et al.*, *Proc. Natl. Acad. Sci. USA* **115** 6, pp. 1227–1231 (2018).

[44] A. I. Coldea *et al.*, *npj Quantum Mater.* **4** 2 (2019).

[45] M. D. Watson *et al.*, *Phys. Rev. B* **92** 121108(R) (2015).

[46] T. Hanaguri *et al.*, *Sci. Adv.* **4** eaar6419 (2018).

[47] K. Matsuura *et al.*, *Nat. Commun.* **8** 1143 (2017).

[48] P. Wiecki *et al.*, *Phys. Rev. B* **98** 020507(R) (2018).

CHAPTER 3

Magnetotransport experiments

3.1 Introduction

As Ohm's law reminds us, the measured voltage drop V between two points in a sample is related to the current I flowing through it by the simple relation $V = RI$, R being the electrical resistance of the given sample. From the resistance R of the measured specimen, which is an extensive quantity – i.e. it depends on the physical dimensions – the intensive quantity electrical resistivity (ρ) can be obtained by $\rho = \frac{S}{d}R$, with S the cross sectional area of the sample and d the distance over which the voltage drop is measured. It is therefore important to measure accurately the physical dimensions of a sample in order to obtain a precise resistivity value. Magnetotransport experiments, exploiting Ohm's law, aim to measure the resistivity of a certain material as a function of varying temperature and magnetic field. Such experiments can deliver important information on the microscopic interactions within the material that are responsible for its resistive state amd ultimately its superconducting state too. High-field magnetotransport experiments on $\mathrm{FeSe}_{1\text{-}x}\mathrm{S}_x$ have resulted in the work presented in Chap. 4, Chap. 5 and Chap. 6 of this thesis. Although transport experiments might sound easy to realize, much care needs to be devoted to their correct implementation in order to obtain the desired results. Especially when dealing with extreme conditions, such as low temperatures and high-magnetic fields, every detail has to be carefully prepared in order to avoid extraneous effects during the experiment and to ensure the reliability of the acquired data.

In this chapter, the techniques used for sample growth and sample preparation for the transport measurements are presented. The types of experiments which produced the results of the different chapters of this manuscript, and the way they were performed, are explained here. Additional characterization of some of the samples is reported in order to demonstrate the high quality of our crystals. In addition, $FeSe_{1-x}S_x$ parameters such as the nematic transition temperature T_s and the superconducting critical temperature T_c are defined and the way they were extracted from the data is clarified. Finally, precautions taken in the high-field environment, for example concerning the thermometry, are described in this chapter.

3.2 Sample growth and preparation for magnetotransport experiments

The samples employed in this work are $FeSe_{1-x}S_x$ crystals in the S substitution range $0 \leq x \leq 0.25$. Single crystals were grown by S. Kasahara at Kyoto University, using the chemical vapour transport technique. A mixture of Fe, Se and S powders together with KCl and $AlCl_3$ powders was sealed in an evacuated SiO_2 tube and heated to 390-450 °C on one end, while the other end was kept at 140-200 °C. All x values quoted in this book are the nominal values provided by the crystal grower. It has been shown that the actual sulphur composition, as determined by energy dispersive X-ray spectroscopy, is approximately 80% of the nominal x [1].

In preparation for the experiments, the crystals were cut into thin rectangular-shaped samples with the surface oriented in the *ab* plane. The size of a typical sample is $1\,\mathrm{mm} \times 300\,\mu\mathrm{m} \times 50\,\mu\mathrm{m}$. The sample was subsequently attached to a quartz substrate with a droplet of superglue. Six electrical contacts were then applied to each sample in a Hall bar geometry, two for current flow at the short sides and two on each of the longer sides to determine the longitudinal resistance (see Fig. 3.2 for a photo of a sample ready for experiment). The contacts were made manually by indium-soldering $25\,\mu\mathrm{m}$-diameter Au-wires on the samples with a sharp hot tip. The width w, the thickness t ($S = wt$) and the contacts distance d were measured with an optical microscope Olympus SZX10 equipped with a

camera model DP27 and connected to a graphics computer software. To ensure a uniform current flow, a layer of Dupont 4929 Ag-paint was applied to the two edges around the indium point contacts that were used for current injection. The voltage drop along both sides of each sample was measured simultaneously and invariably showed consistent behaviour, a further confirmation of homogeneous current flow through our samples. The data were acquired using a standard four-probe technique, applying an ac current of $1\,\mathrm{mA}$ for temperatures above 4.2 K, or $500\,\mu\mathrm{A}$ when lower temperatures were reached, and using lock-in amplifiers to measure the response of the samples.
All samples were preliminarily characterized in a 4-He cryostat inserted in a superconducting magnet with a maximum magnetic field of 16 T. The high field data were acquired in a combination of 4-He and 3-He cryostats inserted in a resistive Bitter magnet with a maximum field of 35 T (Chap. 4) and 38 T (Chap. 5 and Chap. 6). All high field measurements were performed employing the same transport stick, equipped with a rotating sample holder, a Cernox CX-SD temperature sensor, an RS Pro foil strain gauge heater and an Arepoc s. r. o. LHP-NUs Hall probe.

3.3 Observation of Shubnikov-de Haas oscillations

Quantum oscillations have been thoroughly investigated in FeSe [2, 3] and $\mathrm{FeSe}_{1\text{-}x}\mathrm{S}_x$ up until $x = 0.19$ [4]. In Chap. 4, existing results from the literature will be used to obtain the FS parameters needed for the discussion of our own results. In this section, the observation of QOs in the high-field resistivity of our samples will only be used as a characterization tool to confirm that they are of comparable quality. The oscillatory nature of the resistivity, known as the Shubnikov-de Haas (SdH) effect, is due to a more general phenomenon manifesting itself in high magnetic fields and low temperatures in a number of quantities such as, among others, the magnetic susceptibility (de Haas-van Alphen effect), the magnetostriction (variation of a sample size with increasing field), the Hall effect coefficient and the specific heat [5, 6]. These oscillations are due to the quantization of the electron states in Landau levels (LLs) under the application of a strong magnetic field. As the applied magnetic field is varied, the LLs are swept across the Fermi surface resulting in a periodic modulation of the density of states (DOS) with the inverse of the magnetic field [5]. This

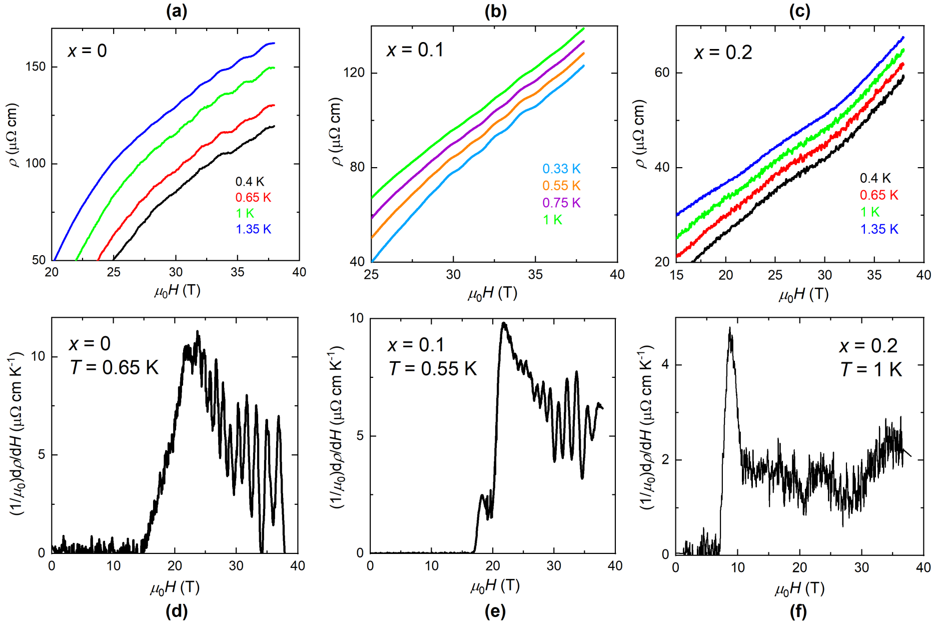

Figure 3.1: Shubnikov-de Haas oscillations in FeSe$_{1\text{-}x}$S$_x$. *High-field $\rho(H)$ curves of (a) FeSe, (b) FeSe$_{0.9}$S$_{0.1}$ and (c) FeSe$_{0.8}$S$_{0.2}$. The colors refer to different temperatures as defined in the legends. The SdH oscillations appear to become progressively slower in H as x increases. This point is clearer when plotting the field derivatives of the same resistivity curves over the entire measured field range (panels d-f).*

modulating effect can be experimentally observed as oscillations of the aforementioned quantities. QOs are a very useful tool to obtain important Fermi surface parameters, like the Fermi wavevector k_{F} from the Onsager relation [7] $F = \frac{A_{\mathrm{F}}\hbar}{2\pi e}$, where F is the oscillation frequency, $A_{\mathrm{F}} = \pi k_{\mathrm{F}}^2$ is any extremal cross-sectional FS area in a plane normal to the applied field, $\hbar$ is the reduced Planck's constant and e is the electron charge. The quasiparticle effective mass m^* can be obtained from a fit to the Lifshitz-Kosevich formula [8] of the temperature dependence of the amplitude of quantum oscillations. QOs can only be observed at low temperatures because, like most metallic properties, they are determined by an average over a range of energies within $k_{\mathrm{B}}T$ (here k_{B} is the Boltzmann's constant) of the Fermi energy E_{F}. If $k_{\mathrm{B}}T$ is too large, all LLs will contribute to the average and the oscillatory structure will disappear. Similarly, high electron scattering can also hinder the observation of QOs. The electron energy ϵ can be defined in terms of the scattering time τ as $\epsilon \approx \hbar/\tau$. If many scattering events occur over the time unit, then τ will be short and therefore ϵ will be large; if ϵ becomes larger than the spacing between the peaks in the DOS, the oscillations are smeared out [6]. Therefore, the observation of quantum oscillations is an indication of low impurity scattering.

In our samples, SdH oscillations could be tracked in the temperature interval 0.33-1.35 K for x values up to 0.2. Panels a-c of Fig. 3.1 show the high-field resistivity of a selection of samples. Relatively fast oscillations can be seen for $x = 0$ and $x = 0.1$, but become slower and less discernable at higher x vlaues, as exemplified in Fig. 3.1c for $x = 0.2$. To illustrate more clearly the oscillatory component of the resistivity, the field derivatives of the $\rho(H)$ curves of the same samples are plotted in panels d-f of Fig. 3.1 at selected temperatures. The SdH oscillations are amplified in the derivatives and can be now better distinguished even at the highest S concentration value $x = 0.2$.

While SdH oscillations are a good indication of the high quality of our samples, they also can be undesirable when, for example, the upper critical field H_{c2} needs to be precisely determined (this point will be touched on again in Chap. 6).

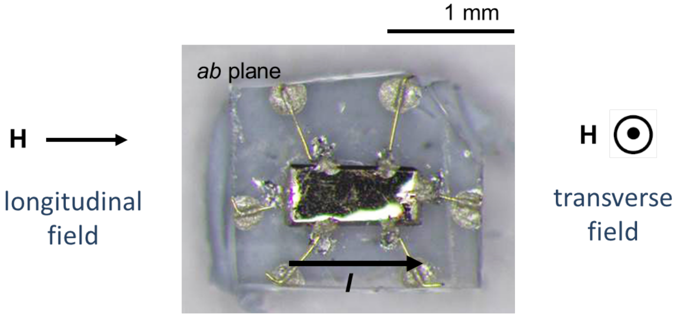

Figure 3.2: Schematic of experimental conditions. *Photo of a sample (glued onto a quartz substrate and already contacted) acquired with an optical microscope. The indium contacts between the sample and the Au wires can be seen. The current I is applied between the two contacts at the short sides of the sample, while the voltage V is measured between the two contacts applied on each of the two long sides of the sample. The longitudinal (transverse) magnetic field orientation used during the experiments is illustrated on the left (right) hand side.*

3.4 Types of experiments

The work presented in this book has mostly resulted from experiments performed at the High Field Magnet Laboratory (HFML) in Nijmegen, the Netherlands. All the experiments carried out during the work of this thesis have involved measurements of the longitudinal resistance, i.e. the resistance along the direction of current flow. The current I was always applied in the conducting planes of $\mathrm{FeSe}_{1\text{-}x}\mathrm{S}_x$, thus parallel to the *ab* crystallographic plane of the material. The experiments themselves can be divided into two main categories, depending on the orientaion of the applied field H with respect to the conducting planes: the longitudinal field configuration when $\mathbf{H}//I//ab$, which in the following will be referred to as simply $\mathbf{H}//ab$, and the transverse field configuration when $\mathbf{H} \perp I$, $\mathbf{H} \perp ab$ or equivalently $\mathbf{H}//c$. The anisotropy in the upper critical field is relatively small in $\mathrm{FeSe}_{1\text{-}x}\mathrm{S}_x$, reaching a maximum value of ~2 for $x = 0.25$ (at $T = 1.35\,\mathrm{K}$). An example is shown in Fig. 3.3 for $x = 0.2$. The ratio ${H_{c2}^{//ab}}/{H_{c2}^{//c}}$ is proportional to $\sqrt{\rho_c/\rho_{ab}}$, therefore the anisotropy in the resistivity is not larger than 4 across the measured series. Thus we can be

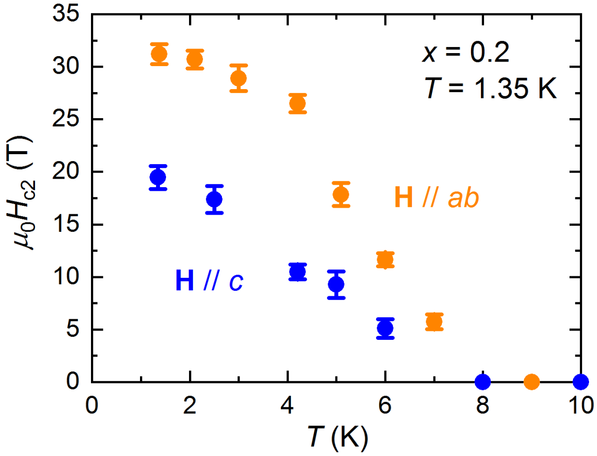

Figure 3.3: Anisotropy in the upper critical field. *The blue (orange) circles represent the transverse (longitudinal) upper critical field* $H_{c2}^{//c}$ ($H_{c2}^{//ab}$) *of a* $\mathrm{FeSe}_{0.8}\mathrm{S}_{0.2}$ *crystal at* $T = 1.35\,\mathrm{K}$. *In this case the anisotropy is* ${H_{c2}^{//ab}}/{H_{c2}^{//c}} \approx 1.6$, *implying a resistivity anisotropy* $\rho_c/\rho_{ab} \approx 2.5$.

confident that, even if there was any c-axis contamination in the resistivity measurements, it would have a negligible impact on the determination of the in-plane resistivity. Fig. 3.2 shows a photo of a contacted sample with a sketch of the two different field orientations. The above defined measuring configurations were determined by the following procedure. First, a constant magnetic field of typically 10 T was applied at a stable temperature of 4.2 K and a Hall probe signal was then used to align the rotating platform either parallel or perpendicular to the field. After that, the field was ramped back to zero. Secondly, the temperature was stabilized, by applying a constant heat to the sample space with a strain gauge, to a value at which the measured sample would be entirely in the normal state (typically 15-20 K). Then, a constant field of 10 T was applied again and the platform was fine-rotated while looking at the variations in the resistance of the sample. Indeed, as it will be shown in Chap. 4, the magnetoresistance (MR) of all samples has a maximum for $\mathbf{H}//c$ and a minimun for $\mathbf{H}//ab$, therefore allowing us to precisely locate the transverse and longitudinal field orientations.

3.5 Thermometer calibration in field

The Cernox resistance thermometer used for the high-field experiments was calibrated in zero magnetic field in the range 0.3-300 K. Most of the results displayed in Chap. 4 are obtained while varying the temperature in a constant magnetic field of 35 T. To obtain a reliable temperature reading in this high-field environment, the output of the Cernox was treated to remove any influence coming from its magnetoresistance. Field sweeps at constant temperature were employed to record the Cernox output at zero field (T(0 T)) and at 35 T (T(35 T)) at several temperatures. To stabilize the temperature in the range $0.3\,\mathrm{K} < T < 1.4\,\mathrm{K}$, the He-3 vapour pressure was varied without applying any heat into the sample space. For the range $1.4\,\mathrm{K} < T < 4.2\,\mathrm{K}$, He-4 vapour pressure was used in an analogous manner. The 4.2 K temperature point was recorded by putting the sample in good thermal contact with the liquid He-4 bath at ambient pressure. For temperatures above 4.2 K, a constant heater power was applied through the strain gauge heater, controlled by a Lakeshore temperature controller. Once the temperature had been stabilized at zero field (typically within a precision of a few millikelvin for 10 minutes), the field was then ramped. In

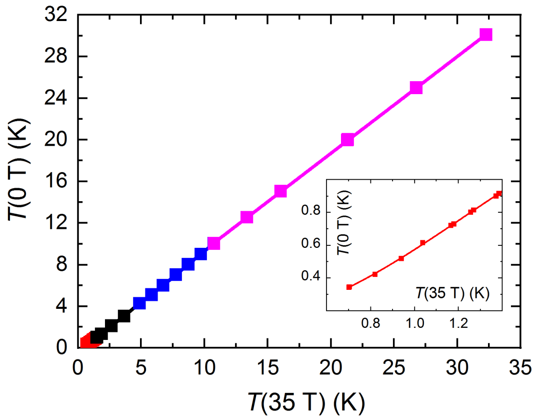

Figure 3.4: Calibration of the Cernox temperature sensor in a magnetic field of 35 T between 0.3 K and 30 K. *The coloured symbols in the graph are the data points taken at different constant temperatures as explained in the text. The points were then divided into four temperature intervals to calculate phenomenological fits, plotted here as lines. The inset shows a zoom of the lowest temperature range.*

the above described way, the plot in Fig. 3.4 was obtained. The data points are divided into four intervals (identified by different colours) in which the temperature dependence of the Cernox MR is slightly different. Third-order polynomial fits, with different fitting parameters, were calculated for the first three ranges, while a linear fit was calculated for the last range. The fits are represented by the solid lines in Fig. 3.4. The inset displays a zoom-in of the lowest temperature range. After acquiring the 35 T temperature ramps shown in Chap. 4, the temperature column was then converted to the actual temperature by means of the fitting functions plotted in Fig. 3.4.

3.6 Determination of T_c and T_s

Zero-field cool-down curves in the temperature interval 4.2-150 K were acquired for all samples and are displayed in Fig. 3.6. The superconducting critical temperature values T_c were determined from these $\rho(T)$ curves as exemplified in Fig. 3.5 for $x = 0.05$: T_c is defined as the temperature at which $\rho(T)$ first acquires a finite value above the noise level. In Fig. 3.6a-d, asymmetric kinks can be detected in the $\rho(T)$ curves; as explained in Chap. 2, those kinks are a signature of the nematic transition. To obtain a better measurement of the nematic transition temperature T_S, the temperature derivatives of all zero-field cool-down curves were obtained. Fig. 3.7 displays the derivatives $d\rho/dT$ of the resistivity curves of Fig. 3.6. The kink in the $\rho(T)$ curves corresponds to a dip in the derivatives, as indicated by the arrows in panels a-d. The sharpness of the resistive kinks is an indication that the S doping of our crystals is homogeneous. At $x = 0.16$ (Fig. 3.7e), the dip has become a shallow symmetric minimum which becomes progressively less pronounced as x increases further (remaining figure panels). This is in agreement with data from the literature [1, 9, 10], which locate the nematic end point at a S concentration of ~16%.

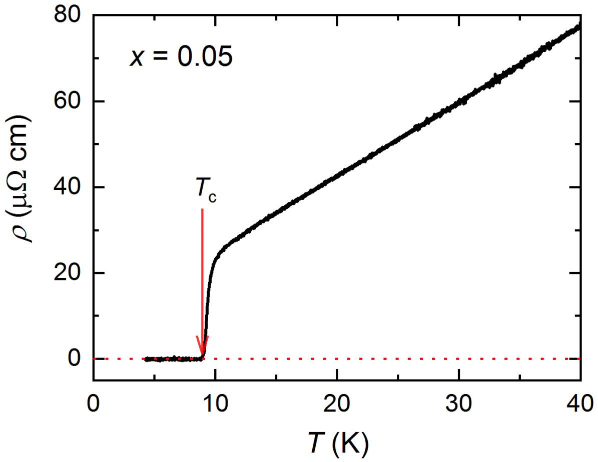

Figure 3.5: Determination of T_c. *$\rho(T)$ curve in the temperature interval 4.2-40 K for $x = 0.05$ (extracted from Fig. 3.6b). T_c is defined as the temperature at which the resistivity first rises above the noise level around zero in the superconducting state (see red arrow).*

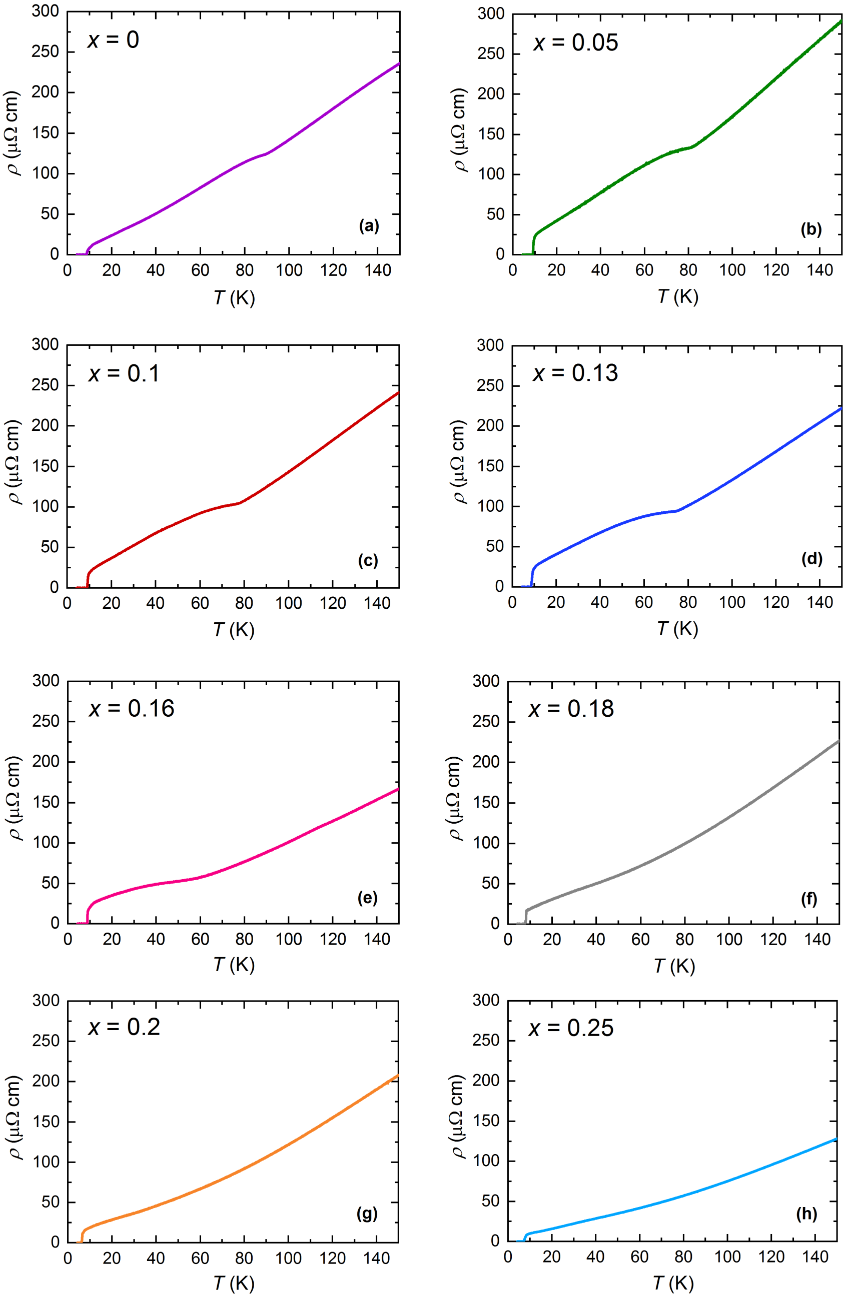

Figure 3.6: Temperature dependence of the resistivity of FeSe$_{1\text{-}x}$S$_x$. *$\rho(T)$ curves of all studied samples in the interval $4.2\,\mathrm{K} \leq T \leq 150\,\mathrm{K}$. The asymmetric kink, evident for $x < 0.16$ (panels a-d), leaves room to a progressively smoother change of slope at higher x values (panels e-h).*

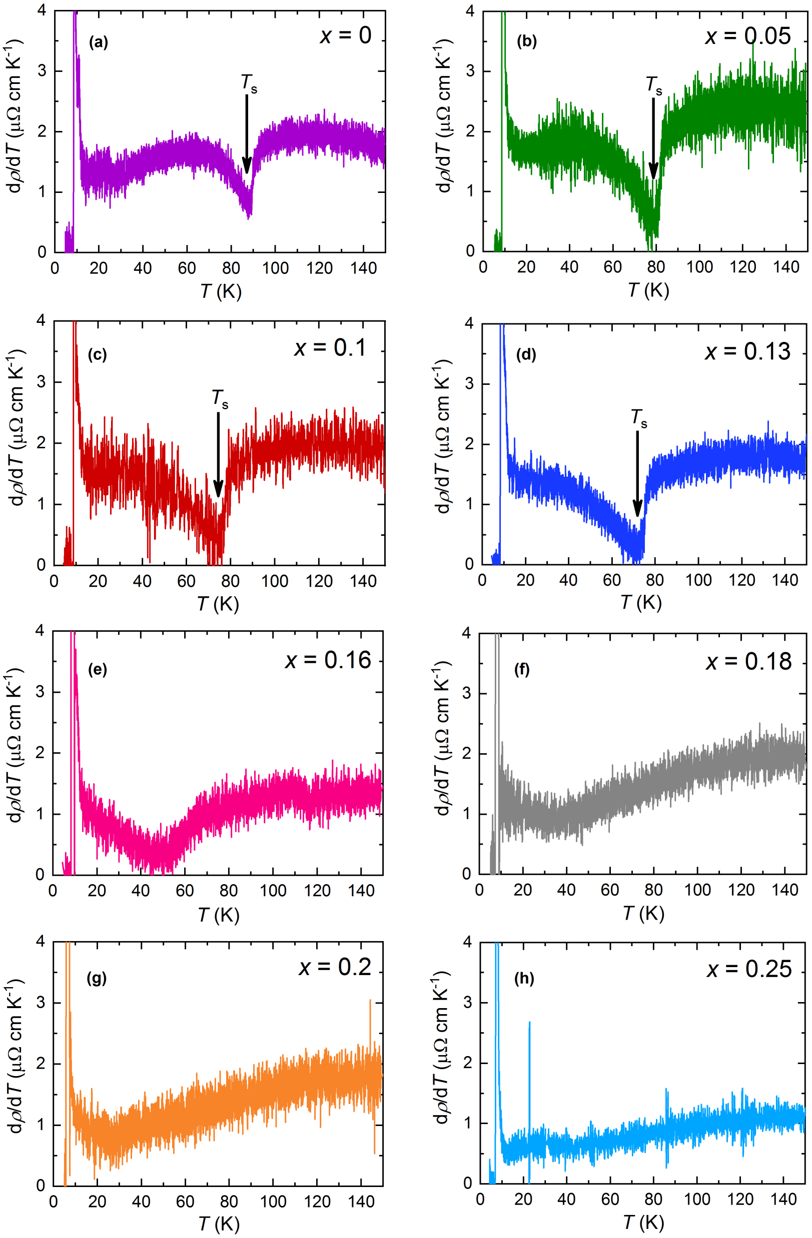

Figure 3.7: Determination of T_s. *The nematic phase transition temperature is determined from the temperature derivatives of the resistivity curves in the broad temperature range 4.2-150 K (see Fig. 3.6). The dip at T_s in the derivative curves for $0 \leq x \leq 0.13$ (corresponding to the kinks in Fig. 3.6a-d) is indicated by the arrows in panels a-d. For $x \geq 0.16$ (panel e), the dip is replaced by a shallow minimum, which becomes progressivelly less pronounced as x increases (panels f-h).*

References

[1] S. Hosoi *et al.*, *Proc. Natl. Acad. Sci. USA* **113** 29, pp. 8139–8143 (2016).

[2] T. Terashima *et al.*, *Phys. Rev. B* **90** 144517 (2014).

[3] M. D. Watson *et al.*, *Phys. Rev. B* **91** 155106 (2015).

[4] A. I. Coldea *et al.*, *npj Quantum Mater.* **4** 2 (2019).

[5] D. Shoenberg, *Magnetic oscillations in metals*, Cambridge University Press (1984).

[6] N. W. Ashcroft and N. D. Mermin, *Solid State Physics*, Harcourt College Publishers (1976).

[7] L. Onsager, *Phil. Mag.* **43** 344, pp. 1006–1008 (1952).

[8] I. M. Lifshitz and A. M. Kosevich, *Zh. Eksp. Teor. Fiz.* **21** 4, p. 730 (1955). [*Sov. Phys. JETP* **2** 4, p. 636 (1956)].

[9] T. Urata *et al.*, *arXiv* **1608.01044** (2016).

[10] Y. Sato *et al.*, *Proc. Natl. Acad. Sci. USA* **115** 6, pp. 1227–1231 (2018).

II

NORMAL STATE, MAGNETORESISTANCE AND SUPERCONDUCTIVITY OF FESE$_{1-x}$S$_x$

CHAPTER 4

Purely nematic quantum critical point

Abstract

Electron nematicity has been observed in many correlated electron systems such as the Fe-pnictides and the cuprates. The striking deviations from conventional Fermi-liquid behaviour as measured in those materials, however, are believed to be attributed to magnetic rather than nematic quantum criticality. In some cases, the existence of a nematic QCP has been argued but its close proximity to a magnetic QCP has made the link with nematicity itself difficult to identify. $FeSe_{1\text{-}x}S_x$ *is unique in this respect since nematic order appears to exist in isolation. The nematic phase is gradually suppressed by S substitution, until it vanishes completely at a S concentration of about 16%. The transition to the superconducting state has, until now, prevented access to the underlying normal state at low temperatures. In this chapter, static high magnetic fields (up to 35 T) are employed to destroy the superconducting state and follow the low-temperature evolution of the resistivity across the putative QCP. Classic signatures of quantum criticality, namely a divergence in the quasiparticle effective mass on approaching the QCP from either side and, at the QCP itself, a strictly T-linear in-plane resistivity, are revealed. Speculations on how nematicity could cause quantum critical behaviour in* $FeSe_{1\text{-}x}S_x$*, based on both existing experimental results and theoretical models, are proposed.*

Part of the work presented in this chapter is adapted from: S. Licciardello *et al.*, "Electrical resistivity across a nematic quantum critical point", *Nature* **567**, pp. 213–217 (2019).

4.1 Introduction

As already seen in Chap. 2, the nematic transition in $\mathrm{FeSe}_{1\text{-}x}\mathrm{S}_x$ at T_s, accompanied by a tetragonal-to-orthorhombic structural transition, is progressively suppressed by the chemical pressure exerted by S substitution until it disappears at $x \approx 0.16$, as visualized in the orange region of the phase diagram reprinted here for convenience in Fig. 4.1. The composition x acts in fact as a non-thermal tuning parameter which suppresses to 0 K the temperature scale responsible for the nematic transition in the material; $\mathrm{FeSe}_{1\text{-}x}\mathrm{S}_x$ thus emerges as a candidate quantum critical system. Moreover, there is no other form of order appearing at or in proximity of T_s, at least in the absence of applied physical pressure, making S substituted FeSe the ideal material to study the evolution of physical properties across a uniquely nematic quantum critical point.

One key aspect of quantum criticality is, as discussed in Chap. 1, the evolution of the electrical resistivity across the temperature vs. tuning parameter phase diagram. As one can see in Fig. 3.6 of Chap. 3, the resistivity curves of $\mathrm{FeSe}_{1\text{-}x}\mathrm{S}_x$ exhibit a quasi-T-linear trend over a (broad) temperature range above T_c and below T_s (when applicable). This temperature region is visually represented in Fig. 4.1 below the purple dashed line. Unfortunately, this strange metallic behaviour has only been studied to date above T_c, before superconductivity obscures it. In order to be able to follow the low-T behaviour of ρ of $\mathrm{FeSe}_{1\text{-}x}\mathrm{S}_x$ across the nematic QCP, one has first to remove the veil of SC by e.g. applying high magnetic fields.

Another hallmark of quantum criticality is a divergence or enhancement of the quasiparticle effective mass around the QCP. This enhancement is attributed to an increase of the quasiparticle scattering cross section as the QCP is approached and the fluctuations of the associated order parameter occur over increasingly long wavelengths [1]. Historically, this phenomenon was first observed through thermodynamic experiments [2]. The specific heat of a conventional metal grows linearly with temperature and the coefficient of this linear dependence is known as the Sommerfeld coefficient (γ_S). The Sommerfeld coefficient is a measure of the renormalized density of states and thus can be regarded as a rough measurement of the effective mass (m^*) of the highest-momentum electrons in the metal [3]. In a quantum critical system, on approaching the QCP, γ_S as measured along the (effective) zero-temperature axis has been found to increase abruptly while at the QCP itself, it is found to grow logarithmically with decreasing temperature [2]. Away from the QCP, the relation between γ_S and A, the T^2-coefficient of the resistivity (due to electron-electron scattering), is contained in the Kadowaki-Woods ratio (KWR) [4], which simply gives the proportionality $\gamma_S \propto \sqrt{A}$. Therefore the divergence of m^* (or better m^{*2}) around a QCP is also manifest as a divergence in A, which can be measured via transport experiments. The divergence in A is invariably found to coincide with a collapse in the temperature range over which the T^2 resistivity survives, a crude measure of the effective Fermi temperature of the quantum critical metal.

In this chapter, static high magnetic fields up to 35 T are employed to suppress SC in FeSe$_{1\text{-}x}$S$_x$ crystals with $0 \leq x \leq 0.25$ and follow the evolution of $\rho(T)$ down to temperatures as low as 0.3 K. The three key aspects of quantum criticality, i.e. a T-linear resistivity, a strong enhancement of the A coefficient and a collapse of the temperature range over which T^2-resistivity is observed, are reported. These findings constitute the first evidence of

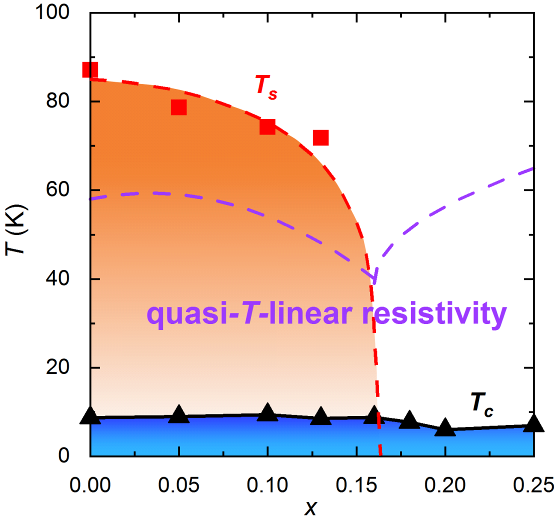

Figure 4.1: (Quasi) T-linear resistivity in FeSe$_{1\text{-}x}$S$_x$. *Phase diagram from Chap. 2, cut at $x = 0.25$. The values for T_c and T_s are determined as explained in Chap. 3. The quasi-T-linear resistivity regime is highlighted below the purple dashed lines.*

quantum critical behaviour in the electrical resistivity originating purely from nematic order. Though the role of nematic fluctuations on shaping this quantum critical behaviour is not yet clear, some conjectures are hereby discussed.

4.2 Longitudinal MR

When employing high magnetic fields to destroy SC in quasi-2D superconductors, the standard procedure is to apply the field perpendicular to the conducting planes ($\mathbf{H}//c$), as this orientation minimizes the upper critical field H_{c2} and thus enables access to the normal state without the need of excessively elevated fields. In $FeSe_{1-x}S_x$ the normal state can be reached with modest applied fields typically below 20 T if $\mathbf{H}//c$ [5]. In this orientation, however, the material also presents a sizeable MR [6] which in some cases has a non-trivial field and/or temperature dependence, making it difficult to subtract its contribution and consequently extract the normal-state resistive behaviour. When $\mathbf{H}//ab$, the high-field MR is found to be either negligible or small and temperature independent. The anisotropy in H_{c2}, as seen in Chap. 3, is only a factor 2 at most, implying that the normal state is still in principle reachable at low enough temperatures with the maximum magnetic field of 35 T available for our experiments. The high

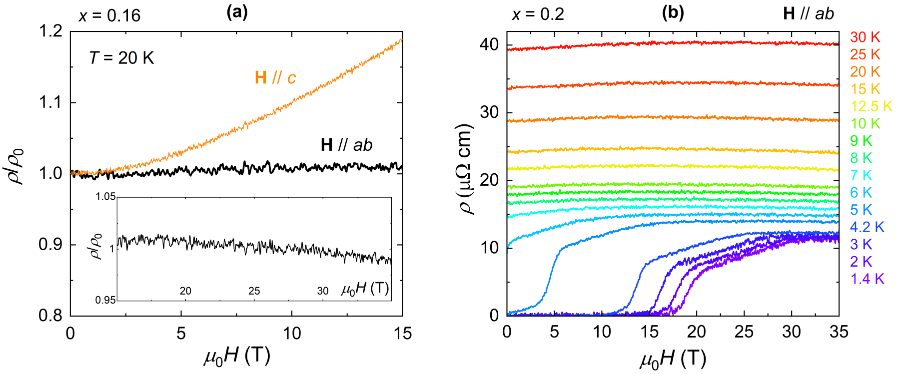

Figure 4.2: ***Longitudinal MR of*** $\boldsymbol{FeSe_{1\text{-}x}S_x}$***,*** $\boldsymbol{x} \geq 0.16$. *(a) Comparison between the transverse (orange) and the longitudinal (black) MR curves up to* $15\,\mathrm{T}$ *at* $20\,\mathrm{K}$ *for* $x = 0.16$. *The inset displays the continuation of the* $\mathbf{H}//ab$ *MR up to* $35\,\mathrm{T}$. *(b) Set of* $\rho(H)$ *curves up to* $35\,\mathrm{T}$ *for* $x = 0.2$*, recorded at several temperatures in the interval* $1.4\,\mathrm{K} \leq T \leq 30\,\mathrm{K}$.

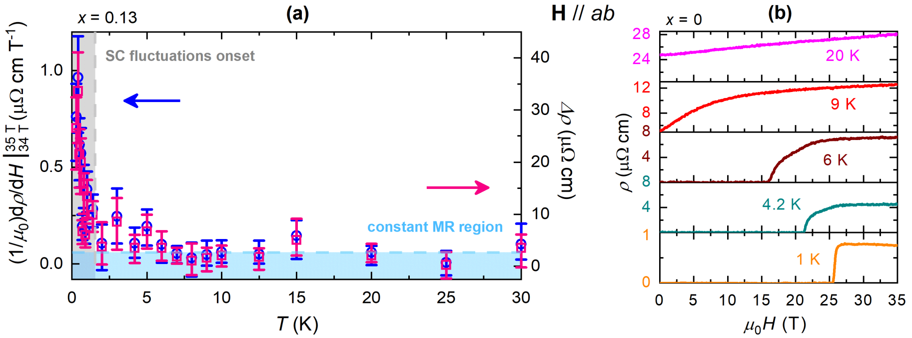

Figure 4.3: Longitudinal MR of FeSe$_{1\text{-}x}$S$_x$, $x < 0.16$. *(a) Slope of linear fits (calculated between 34 and 35 T) to the longitudinal MR curves ($(1/\mu_0)d\rho/dH$) of FeSe$_{0.87}$S$_{0.13}$ at different temperatures (blue circles), and difference between the 35 T resistivity and its extrapolated 0 T value from the same linear fits (pink circles). Vertical error bars represent a compound error of the difference in slope maxima and minima associated with the scatter in the data and uncertainty in the geometrical factors. (b) $\rho(H)$ curves of FeSe up to 35 T at a selection of temperatures between 1 and 20 K. Note that the extent of the y-scale is different for the 1 K curve because ρ is much smaller than at higher temperatures.*

field experiments described in this chapter were performed with $\mathbf{H}//ab$ with the aim of following the low-T form of the resistivity of FeSe$_{1\text{-}x}$S$_x$ while minimizing as much as possible any extrinsic effect – other than the suppression of the superconducting state – caused by the applied field. Because this point constitutes the foundations of the work presented below, it is hereby more precisely explained with the aid of some experimental data.

The absence of longitudinal MR for $x \geq 0.16$ is illustrated in Fig. 4.2. Panel a displays a comparison between the longitudinal and transverse MR of FeSe$_{0.84}$S$_{0.16}$ at $T = 20\,\mathrm{K}$. Already in the $0\,\mathrm{T} < \mu_0 H \leq 15\,\mathrm{T}$ field interval the transverse MR reaches about 20%, while the longitudinal one is essentially flat and remains so up to 35 T (see fig. inset). A set of $\rho(H)$ curves of FeSe$_{0.8}$S$_{0.2}$ for $\mathbf{H}//ab$ and for a selection of temperatures in the range 1.4-30 K, is shown in Fig. 4.2b. It is evident that the MR is negligible at all temperatures up to 35 T, ensuring that the high-field resistivity is equivalent to the zero-field resistivity in the absence of SC (of better said, *if* SC were absent).

For $x < 0.16$, FeSe$_{1\text{-}x}$S$_x$ exhibits a finite positive MR, though as Fig. 4.3a demonstrates, the MR has a negligible T-dependence over a broad temperature range and therefore results only in a vertical shift of the high field resistivity, while still preserving the correct form of the effective zero-field resistivity. In panel a the slope of $\rho(H)$ between 34 and 35 T (extracted from linear fits) is plotted as a function of temperature (blue circles) for $x = 0.13$. In the T-range 1.5-30 K, the slope is essentially constant (within error bars) and it only deviates from this behaviour at lower temperatures when superconducting fluctuations prevent the normal state from being fully accessed. This implies, as anticipated above, that the only effect of the applied magnetic field is to shift ρ to higher values, without affecting its T-dependence. A similar behaviour is found, and the same conclusion are drawn, when plotting $\Delta\rho = \rho(35\,\mathrm{T}) - \rho_{extrap}(0\,\mathrm{T})$ (pink circles in Fig. 4.3a), $\rho_{extrap}(0\,\mathrm{T})$ being the extrapolation at 0 T of the linear fits calculated between 34 and 35 T. The same trend is observed in all other crystals with $x < 0.16$, with the exception of pure FeSe, whose longitudinal MR does vary with temperature. In fact, this T-dependence becomes progressively smaller with decreasing temperature, until it vanishes at $T \leq 4.2\,\mathrm{K}$ (see Fig. 4.3b), allowing us to safely identify the high-field, low-temperature, $\rho(T)$ with the zero-field, non-superconducting state.

All the results presented in this chapter refer to measurements in the in-plane field orientation $\mathbf{H}//ab$, unless specified otherwise.

4.3 T^2 to T-linear to T^2 resistivity crossover in the phase diagram

Fig. 4.4 reveals the evolution of the low-T ρ of $FeSe_{1\text{-}x}S_x$, both at zero-field and in a 35 T magnetic field, for all measured x values. Note that, for $x < 0.16$ (panels a-d), the 0 T (blue) and the 35 T (black) curves are parallel to each other, confirming that the effect of the magnetic field is only to shift the resistivity to higher values without adversely affecting its temperature dependence. To begin our discussion, let us first focus on pure FeSe (Fig. 4.4a). The 35 T $\rho(T)$ curve decreases linearly with temperature until a temperature of ~10 K, below which it passes through an inflection point before developing a quadratic temperature dependence at the lowest T. Note the extremely low ($< 1\,\mu\Omega\,\mathrm{cm}$) residual resistivity in FeSe.

A similar resistivity behaviour is found for all sulphur concentrations up to $x = 0.13$ (Fig. 4.4b-d). The inflection point, especially pronounced

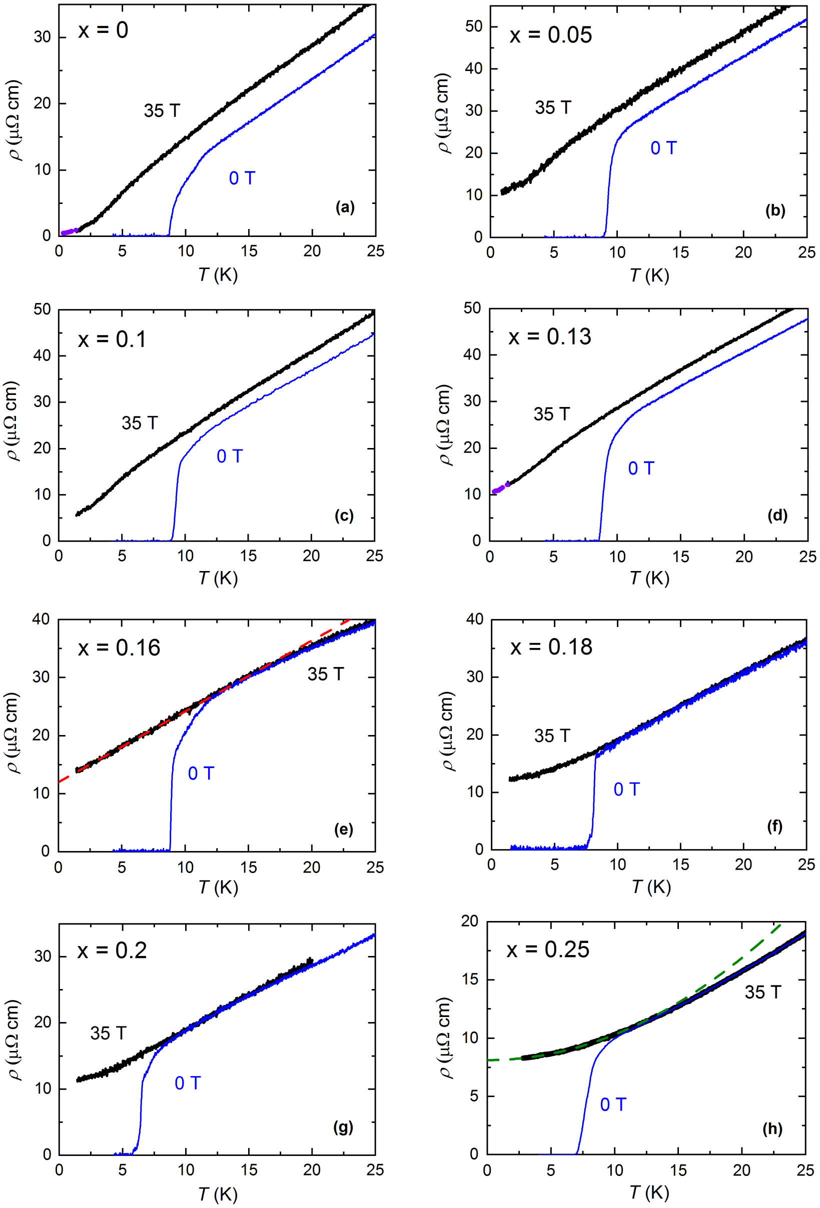

Figure 4.4: Evolution of $\rho(\boldsymbol{T})$ ***of FeSe***$_{1\text{-}x}$***S***$_x$ ***across the phase diagram.*** 0 T *(thin blue lines) and* 35 T *(thick black lines)* $\rho(\mathrm{T})$ *curves for all measured samples. The purple dots in (a) and (d) are obtained from individual field sweeps taken at lower temperatures. The red dashed line in (e) is a linear fit and the green dashed line in (h) is a quadratic fit.*

in $x = 0$, is arguably the only extrinsic feature introduced by the applied magnetic field and its magnitude is thus expected to be reduced as the strength of the applied field is reduced. Moreover, since the MR of FeSe becomes negligible below 4.2 K, the crossover to T^2 resistivity can be considered a robust feature of the data. For $x = 0.16$, the resistivity is strictly T-linear from ~14 K, as indicated by the linear fit in Fig. 4.4e (red dashed line), and it remains so until the lowest temperature at which the normal state could be accessed in 35 T (~1.5 K). Panels f-h show the temperature behaviour of $\rho(T)$ for x values up to 0.25. The T-linear to T^2 crossover appears again, but for these higher dopings the temperature region of the T^2 regime is more extended than it was for $x < 0.16$ and becomes progressively broader with growing x (as highlighted by the quadratic fit in Fig. 4.4h), while the T-linear regime is shifted to higher T. Note that for $x \geq 0.16$, the 35 T curves completely overlap with the zero-field curves, in the normal state region, leaving little doubt as to their extension to lower temperatures.

In summary, the low-T dependence of the resistivity of $\text{FeSe}_{1\text{-}x}\text{S}_x$ crosses over from T^2 for $x < 0.16$ to T-linear at $x = 0.16$ to T^2 again for $x > 0.16$. As introduced in Chap. 1, a quadratic T-dependence of the limiting low-T resistivity is expected for a correlated Fermi-liquid. The fact that the limiting behaviour of $\rho(T)$ for $x = 0.16$ is not T^2 is a clear signature of non-Fermi-liquid physics which might be attributed to quantum criticality.

4.3.1 The temperature scales T_1 and T_2

In order to determine more precisely the form of $\rho(T)$ at 35 T, its temperature derivatives have been examined as illustrated in Fig. 4.5. For all $x \neq 0.16$, $d\rho/dT$ is linear up to a temperature labelled T_2 and passes through the origin (as shown by the blue dashed lines), implying that the resistivity is strictly T^2 below T_2. After an intermediate regime, which presents a peak for $x < 0.16$ (corresponding to the inflection point of Fig. 4.4a-d), the derivative attains a constant value above a certain temperature T_1 (black dashed line) corresponding to the regime of strictly T-linear resistivity. Fig. 4.5e shows that the behaviour of $d\rho/dT$ for $x = 0.16$ is qualitatively different. The derivative is constant up to a temperature of ~14 K, indicated by the green arrow, implying that the resistivity is indeed T-linear for at least a decade in temperature at this x value, as already revealed by Fig. 4.4e and shown in more detail in Fig. 4.6e.

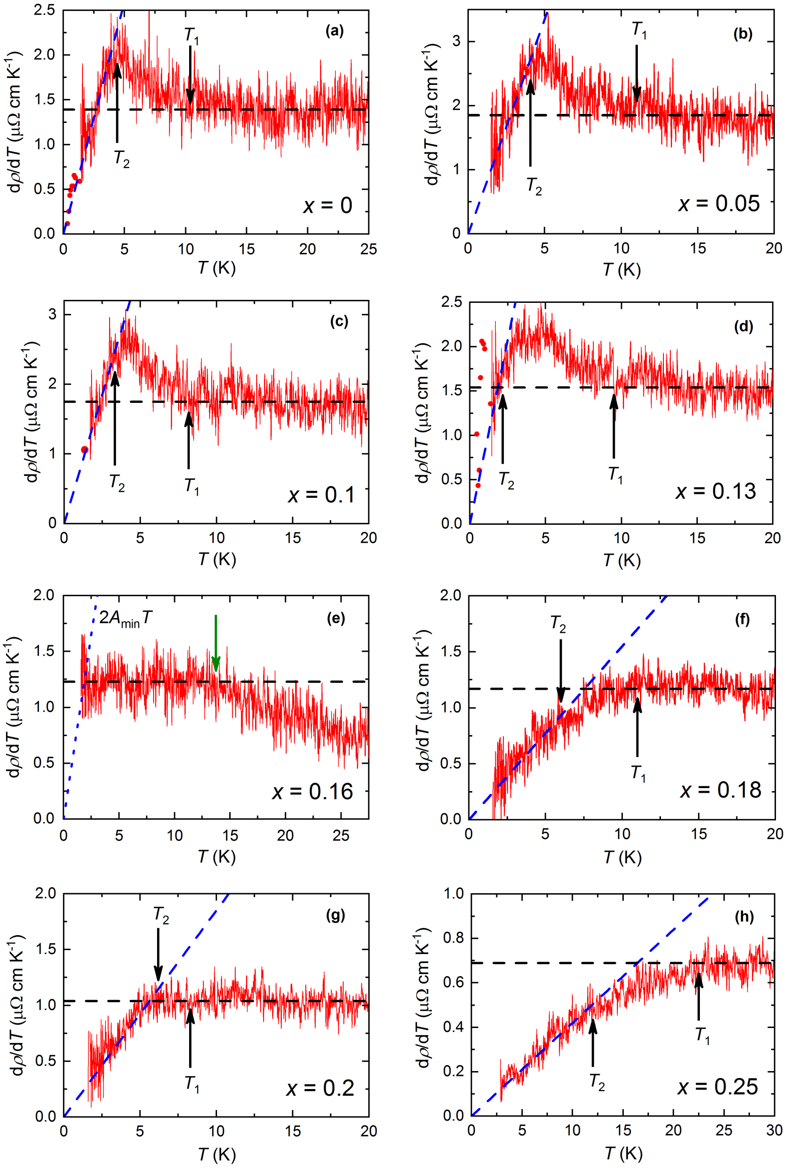

*Figure 4.5: **Evolution of** $d\rho/dT$ **of** $FeSe_{1\text{-}x}S_x$ **across the phase diagram.** Temperature derivative of the* $35\,\mathrm{T}$ *resistivity curves of Fig. 4.4. The blue (black) dashed lines represent the linear (constant) regimes of* $d\rho/dT$*. The temperature scales* T_1 *and* T_2 *are indicated by the black arrows. The slope of the linear regime corresponds to 2A, where A is the coefficient of the* T^2*-resistivity. The blue dotted line in (e) is employed to estimate a lower limit of A for* $x = 0.16$ (A_{min})*. The green arrow defines the extent of the strictly T-linear regime at this x value.*

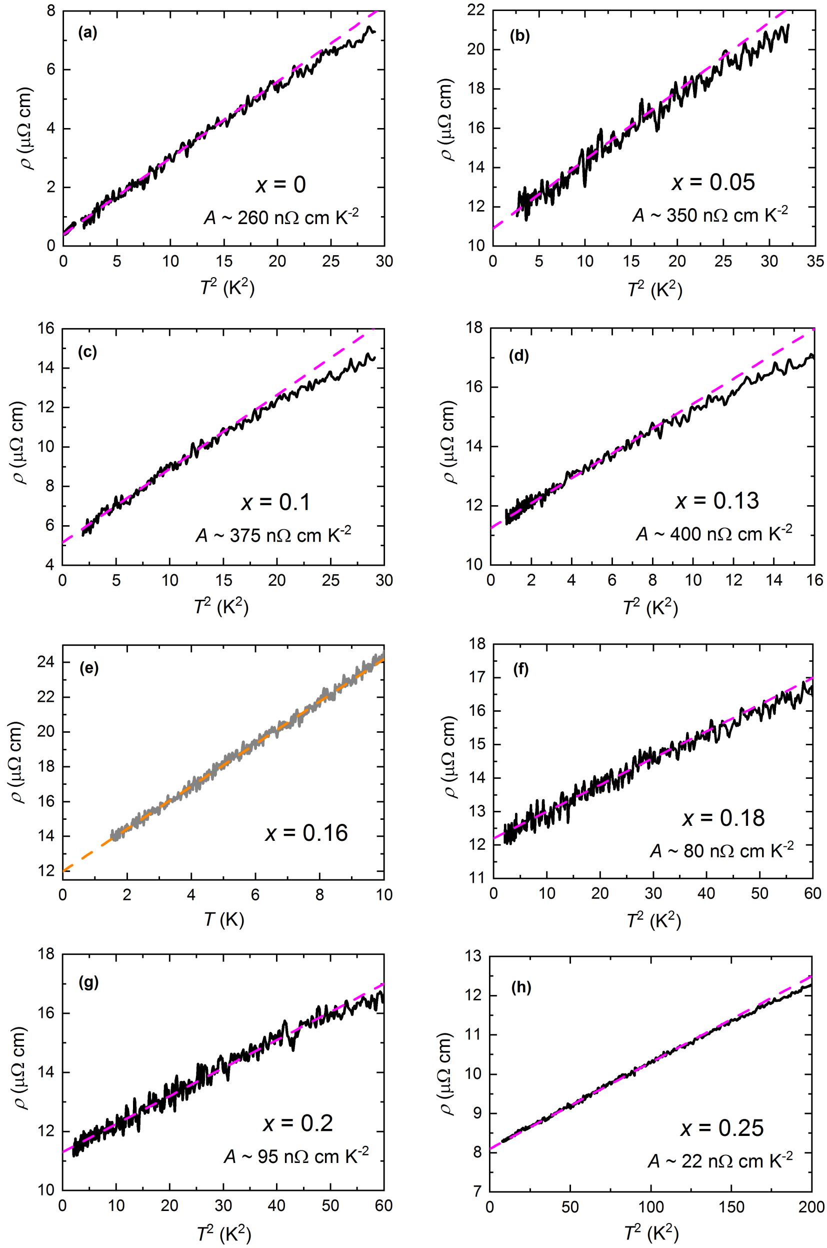

Figure 4.6: Determination of the A coefficients from the resistivity curves. 35 T *resistivity curves from Fig. 4.4 plotted as a function of* T^2*. The magenta dashed lines are linear fits up to* T_2^2*, the slopes of which give a measure of A. For* $x = 0.16$ *(panel e), a detail of the* 35 T ρ *vs. T curve of Fig. 4.4e is displayed, showing that there is no trace in our data of a crossover to* T^2*-resistivity at this doping level.*

4.3.2 The T^2-coefficient A

The coefficient A of the T^2 resistivity is given by half the slope of the linear fits of the $d\rho/dT$ curves up to $T = T_2$ (blue dashed lines in Fig. 4.5). An alternative determination of A can be obtained by plotting ρ against T^2, as displayed in Fig. 4.6. Linear fits are drawn between the lowest measured temperature and T_2^2 and A is extracted from their slopes. After repeating this procedure for all measured crystals, a plot of $A(x)$ can be generated. This is shown in Fig. 4.7 as solid black triangles. The evolution of $A(x)$ is found to follow closely the doping dependence of the average superconducting gap Δ (open green triangles), as measured by STM and reported in ref. [7]. Taken on face value, the drop in both A and Δ outside of the nematic phase, especially dramatic for the former, suggests that the scattering of

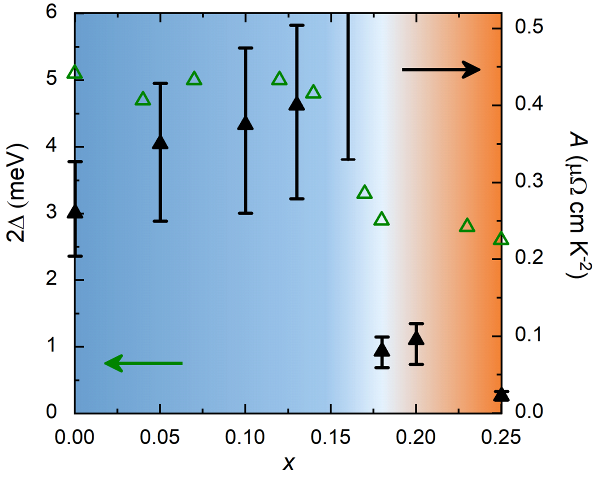

Figure 4.7: Influence of nematic fluctuations on the pairing strength. *Evolution of the T^2-coefficient A (solid black triangles) and of twice the superconducting gap Δ (open green triangles), reported here from ref. [7]. A exhibits a modest increase inside of the nematic phase, which could also be consistent with no increase within our error bars, but it experiences an abrupt fivefold reduction once outside of it. This trend compares with a two-fold reduction of Δ. Vertical error bars for A represent a compound of the difference in slope maxima and minima associated with the scatter in the $d\rho/dT$ curves and of uncertainties in geometrical factors.*

quasiparticles off the nematic fluctuations inside and outside of the nematic phase has a profound effect on the superconducting pairing strength. Note that in Fig. 4.7 there is no experimental point for $A(x{=}0.16)$, but only a lower limit. This is due to the fact that the limiting form of $\rho(T)$ is not quadratic but linear in T. The lower limit for $A(x{=}0.16)$ is obtained from Fig. 4.5e by drawing a straigth line (blue dotted line in the figure) passing through the origin and through the constant value (black dashed line) attained by the derivative for $1.5\,\mathrm{K} \leq T \leq 14\,\mathrm{K}$. Half of the slope of this line gives a lower limit $A_{\mathrm{min}} \approx 330\,\mathrm{n\Omega\,cm\,K^{-2}}$. In fact, by comparison with all the other x values, T_2 is always at least half of T_1. If this rule of thumb applies to $x = 0.16$ too, then our estimate of the lower bound for A should be doubled. Even though $A(x)$ does not present the expected divergence around the putative QCP, it will be shown in § 4.4 to contain in itself this key aspect of quantum criticality.

As explained in § 4.1, the coefficient A is related to the quasiparticle effective mass m^* as enshrined in the KWR. For a multiband system, the relation between A and m^* can be expressed in the following way [8]:

$$A = \frac{8\pi^3 \tilde{a} c k_{\mathrm{B}}^2}{N e^2 \hbar^3} \frac{1}{\sum\limits_i k_{\mathrm{F},i}^3 / m_i^{*2}}, \tag{4.1}$$

where c is the c-axis lattice parameter, N is the number of formula units per unit cell, $k_{\mathrm{F},i}$ and m_i^* are, respectively, the Fermi wavevector and the quasiparticle effective mass for each individual Fermi pocket i (the sum is calculated over the entire Fermi surface), and $\tilde{a}$ is the effective minimum mean free path ℓ (the Mott-Ioffe-Regel limit), which can be set (depending on the appropriate definition) as the a-axis lattice parameter ($\ell = a$) or as the inverse of the Fermi wavevector ($k_{\mathrm{F}}\ell = 1$) [9–11].

As anticipated in Chap. 2, band structure calculations for FeSe have determined that its FS is composed of five pockets [13, 14]. This theoretical conclusion, however, does not agree with quantum oscillations experiments, which reported only four fundamental frequencies [12, 13, 15] that could be attributed to the extremal areas of two quasi-cylindrical pockets. Using Eq. (4.1) and the QO data of the aforementioned references, an estimate of the A coefficient can be obtained for FeSe; we can then compare that estimate to the value extracted from our transport experiments (from Fig. 4.7). The measured QO frequencies F and effective masses m^* from refs. [12, 13] are listed in Table 4.1.

Fermi pocket label	F (kT) ref. [12]	m^* (m_e) ref. [12]	F (kT) ref. [13]	m^* (m_e) ref. [13]
α	0.06	1.9	0.11	3.0
β	0.20	4.3	0.20	4.1
γ	0.57	7.2	0.55	6.6
δ	0.68	4.2	0.66	4.3

Table 4.1: *Quantum oscillation frequencies F and effective masses m* (in units of m_e) of each measured Fermi pocket from refs. [12, 13].*

In order to calculate an estimate for $A(x=0)$, certain criteria have to be met. First of all, an estimate of the Sommerfeld coefficient γ_S, which can be obtained for FeSe from the sum of the (averaged) masses of each Fermi pocket, should be in agreement with the measured value [16–18]. Secondly, the cross-sectional areas of the electron and hole pockets should be equivalent in order to ensure charge neutrality. The pairing of frequencies in Table 4.1 that satisfies both criteria is α/δ and β/γ. This way, the resulting averaged effective masses for the two pockets are $3.35m_e$ and $5.55m_e$, which give $\gamma_S = 6.2\,\mathrm{mJ\,mol^{-1}\,K^{-2}}$, in excellent agreement with the range of reported values of $5.7 - 6.8\,\mathrm{mJ\,mol^{-1}\,K^{-2}}$ [16–18]. Moreover, the averaged frequencies (areas) are indeed equivalent to each other (~0.38 kT), thus ensuring that charge neutrality is preserved. These results support the two-band (one hole- and one electron-band) picture in FeSe, in agreement with the conclusions of the most recent and careful heat-capacity study of ref. [18]. Such a picture is considered in the following to finally calculate a value for the A coefficient of pure FeSe from QO data.

Having two Fermi pockets of equal cross-sectional area transforms Eq. (4.1) into a simpler expression:

$$A = \frac{8\pi^3 \tilde{a} c k_B^2}{N e^2 \hbar^3 k_F^3} \frac{1}{\sum_i 1/m_i^{*2}}. \tag{4.2}$$

Using the average frequency of 0.38 kT, based on the above assignment of the frequencies listed in Table 4.1, we obtain $k_F = \sqrt{2eF/\hbar} = 1.07\,\mathrm{nm^{-1}}$. From the crystal structure of FeSe we know that $N = 2$ and $c = 5.52$ Å. There are now two scenarios, depending on the two possible definitions of $\tilde{a}$: (i) $\tilde{a} = a$ or (ii) $\tilde{a} = 1/k_F$. Scenario (i) gives $A = 90\,\mathrm{n\Omega\,cm\,K^{-2}}$ (using $a = 3.76$ Å) while scenario (ii) gives $A = 230\,\mathrm{n\Omega\,cm\,K^{-2}}$. The latter is in excellent agreement with our experimentally determined value ($A = 260 \pm 55\,\mathrm{n\Omega\,cm\,K^{-2}}$) and suggests that the origin of the T^2 resistivity of FeSe is indeed electron-electron (e-e) scattering.

4.4 QCP at $x_c = 0.16$

From Eq. (4.2), it is clear that A not only depends on m^* but also on k_F. Although S substitution for Se is an isovalent substitution, band structure calculations and QO experiments have revealed that both the electron and hole pockets expand upon S substitution, giving rise to an increase in k_F with x (while still preserving charge neutrality). This implies that A alone is not a good *tracking parameter* for the evolution of the effective mass across the phase diagram. Therefore, in order to better track the evolution of $m^*(x)$, the influence of k_F on A as x increases must be taken into account. To achieve this, we refer to existing QO experiments which have followed the frequencies already found in FeSe as a function of increasing S content, up to $x = 0.19$ [19]. In the following, we assume that the new frequency ϵ ($F = 0.4\,\mathrm{kT}$ for $x = 0$), reported in ref. [19] is the second harmonic of β ($F = 0.2\,\mathrm{kT}$), rather than a signature of the emergence of a new pocket which, as seen in § 4.3.2, would be inconsistent with the measured specific

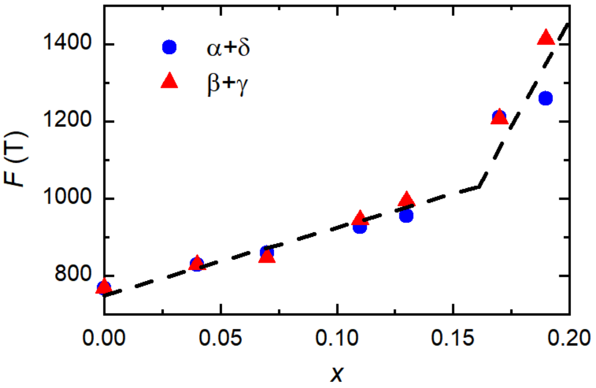

Figure 4.8: The x-dependence of the QO frequencies of FeSe$_{1\text{-}x}$S$_x$. *Sums $\alpha + \delta$ (blue circles) and $\beta + \gamma$ (red triangles) of the QO frequencies from ref. [19]. The two dashed lines are empirical fits.*

heat coefficient γ_S; we also assume that our two-band picture for FeSe applies equally to FeSe$_{1\text{-}x}$S$_x$. Fig. 4.8 displays the two sums $\alpha + \delta$ and $\beta + \gamma$ as a function of x. The two values are always found to overlap, implying that charge neutrality is still preserved as x grows. Only for $x = 0.19$ is $\alpha + \delta \neq \beta + \gamma$, maybe reflecting the emergence of a third pocket, associated with the measured frequencies χ and λ reported in [19]. From the dashed lines of Fig. 4.8 we can then interpolate the averaged $2F$ values and use these to deduce $k_F(x)$ for each studied sample. From this analysis, we can then obtain a modified A coefficient (normalized to the FeSe value):

$$A^* = \frac{k_F^3(x)}{k_F^3(0)} A, \tag{4.3}$$

where $k_F(0)$ is the Fermi wavevector of FeSe calculated in § 4.3.2. For $x = 0.16$, a lower limit for A^* has been obtained by applying Eq. (4.3) to the lower limit for A. A^* mimics the evolution of $m^{*2}(x)$ and is plotted

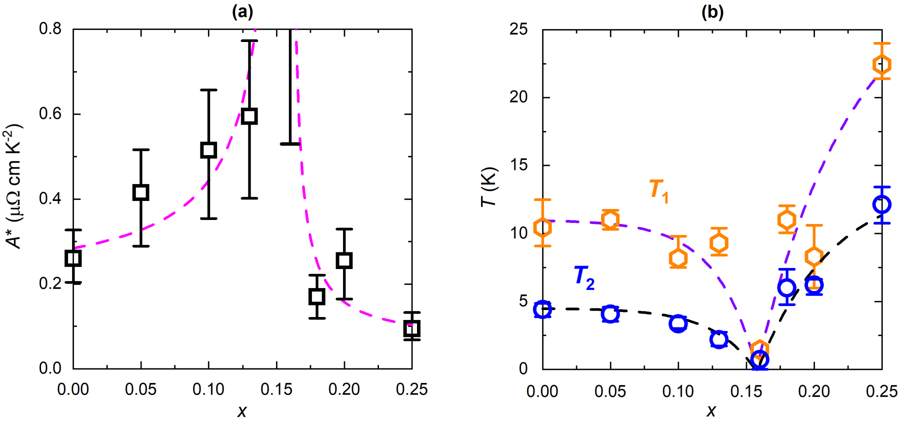

Figure 4.9: Quantum critical behaviour around $\boldsymbol{x_c = 0.16}$***.*** *(a) Evolution of the modified coefficient A* with x. Vertical error bars are the same as in Fig. 4.7, but rescaled by a factor A*/A. The magenta dashed lines represent the theoretical prediction for the divergence of the square of the quasiparticle effective mass around a nematic quantum critical point [20]. (b) Evolution of the temperature scales* T_1 *(orange hexagons) and* T_2 *(blue circles) with x. Vertical error bars originate from the standard deviation of the experimental data. The purple and black dashed lines are guides to the eye. The divergence of A* in (a) and the formation of the characteristic fan-shaped region in (b) point to a QCP at* $x_c = 0.16$*.*

in Fig. 4.9a. A^* is found to be enhanced on approaching $x = 0.16$ from either side, indicating a tendency of m^* to diverge around that x value. This finding, paired with the observation that the two temperature scales T_1 and T_2 – introduced in § 4.3.1 and plotted here in Fig. 4.9b – both approach zero at $x = 0.16$ to generate the characteristic fan associated with quantum criticality, provides evidence for all three manifestations of quantum criticality in the electrical transport of $\mathrm{FeSe}_{1\text{-}x}\mathrm{S}_x$, thus strongly suggesting the realization of a QCP at $x_\mathrm{c} \equiv 0.16$.

The dashed lines in Fig. 4.9a show the expected enhancement in ${m^*}^2$ near a nematic QCP [20]. The theoretical fit is in good agreement with our data points, within error bars, but what theory fails to explain is the presence of a T-linear resistivity at the nematic QCP itself. At the same time, based on discussions in Chap. 2, a magnetic origin for the observed QCP can be ruled out. Indeed, the pressure-induced SDW phase is found to be shifted to progressively higher pressures with increasing x [21] while the spin fluctuations in FeSe at ambient pressure [22] are strongly suppressed by S substitution [23]. Thus, at $x = x_\mathrm{c}$ the SDW phase is located far from the ambient pressure axis of our experiments and the spin fluctuations are believed to be strongly suppressed.

Once magnetic order has been excluded, nematicity is the only possible origin of the quantum critical behaviour in $\mathrm{FeSe}_{1\text{-}x}\mathrm{S}_x$. The Pomeranchuk instability, which generates nematic fluctuations, is a zero-momentum transfer ($Q = 0$) instability [24]. With this in mind, it seems hard to explain the appearance of a large T^2 resistivity below the quantum critical fan, that is consistent with dominant *e*-*e* scattering arising from umklapp processes with large-Q. However, if impurity scattering processes become more efficient than umklapp processes in relaxing momentum, both the quantum critical scaling of the Fermi-liquid-like T^2 resistivity on approaching the QCP and the non-Fermi-liquid (T-linear) resistivity within the quantum critical fan, could be accounted for [25, 26]. This scenario provides a possible explanation for disordered $\mathrm{FeSe}_{1\text{-}x}\mathrm{S}_x$, but does not work for pure FeSe. All these considerations suggest that a new viewpoint is perhaps needed to explain nematic quantum criticality. Such a viewpoint might be offered by the prediction of an antiferroquadrupolar (AFQ) order in FeSe. The theoretical proposal of ref. [27] foresees $(\pi, 0)$ magnetic excitations, which have been verified by inelastic neutron scattering experiments [28, 29]. En passant, the presence of an AFQ order, which according to theory would suppress any antiferromagnetic order, might offer a natural explanation for the absence of AFM in FeSe. Recent Raman spectroscopy experiments have proposed the development of a stripe quadrupole (SQ) order in $\mathrm{FeSe}_{1\text{-}x}\mathrm{S}_x$, whose fluctuations are strongest around x_c [30]. Although the evolution of the AFQ order as a function of S concentration is still unknown, a coupling between AFQ and SQ order is in principle allowed provided that they have the same ordering vector. However, whether or not that coupling, or the coupling between nematicity and either AFQ or SQ order might result in strange metallic behaviour, is a question that remains unanswered.

4.5 *T*-linear resistivity and scattering rate

The linear behaviour of $\rho(T)$ in the quantum critical fan above T_1 contains useful information on the transport scattering rate $1/\tau$ of the material. From the Drude expression for the electrical resistivity in a 2D system we can obtain the following equation:

$$\frac{d(\hbar/\tau)}{dT} = \frac{Ne^2}{2\pi c}\sum_i \left(k_{\mathrm{F},i} v_{\mathrm{F},i}\right)\frac{d\rho}{dT}, \tag{4.4}$$

where $v_{\mathrm{F},i}$ is the Fermi velocity of the i-th pocket. It can be argued that, since quantum criticality is associated with the depression of energy scales towards zero temperature, temperature itself becomes the only relevant energy scale [31]. This implies that the only characteristic energy becomes $k_\mathrm{B}T$ and, following theoretical proposals about T-linear scattering rate in quantum critical fluids [32, 33], that the characteristic scattering time is $\tau = \alpha_\mathrm{P}(\hbar/k_\mathrm{B}T)$ (the Planck time), with α_P a dimensionless parameter. Under the same assumptions of § 4.3.2 (one electron- and one hole-pocket, perfectly compensated and with the same Fermi wavevector) and using the relation $v_\mathrm{F} = \hbar k_\mathrm{F}/m^*$, from Eq. (4.4) we can then obtain an expression for α_P of FeSe:

$$\alpha_\mathrm{P} = \frac{Ne^2\hbar k_\mathrm{F}^2}{2\pi c k_\mathrm{B}}\sum_i {}^{1}/{m_i^*}\,\frac{d\rho}{dT}, \tag{4.5}$$

with $d\rho/dT$ our experimentally determined slope of the T-linear resistivity. Eq. (4.5) can be generalized to $\mathrm{FeSe}_{1\text{-}x}\mathrm{S}_x$ by using the $k_\mathrm{F}(x)$ values obtained from Fig. 4.8, while the $m^*(x)$ values can be obtained from A^* using the scaling relation $m^*(x) = \sqrt{\frac{A^*(x)}{A^*(0)}}m^*(0)$, $A^*(0)$ being the A^* coefficient of

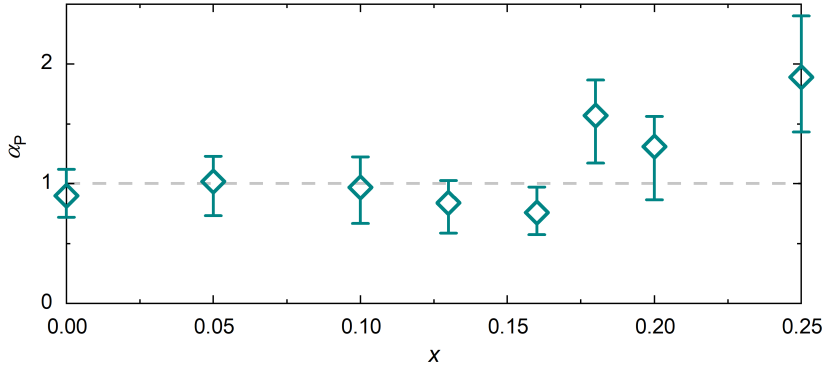

Figure 4.10: Planckian dissipation limit for the scattering rate of FeSe$_{1\text{-}x}$S$_x$. *Dimensionless parameter α_P (as defined in the text) vs. x. The calculated values fall all between 1 and 2. Vertical error bars represent a compound of the standard deviation in the derivatives and of uncertainties in geometrical factors.*

FeSe and $m^*(0) = (5.55 + 3.35)m_e/2$ the pocket-averaged effective mass of FeSe. The behaviour of α_P across the phase diagram is then plotted in Fig. 4.10. As it can be seen, α_P ranges in value from 1 to 2 for all x. A similar phenomenon has been found in many materials which, despite profound differences in the structure, microscopic interactions and dominating scattering mechanisms, all exhibit a T-linear resistivity regime with a similar magnitude of α_P [31]. Recently, this relation has been proposed for a number of cuprate superconductors with strange metallic behaviour as $T \to 0\,\mathrm{K}$, and the proposal that this so-called Planckian dissipation limit for the scattering rate is in fact the principle behind the T-linear resistivity – no matter what the scattering mechanism is – has been advanced [34]. The data presented here suggest that such Planckian dissipation is indeed a feature of the entire QC fan, not simply reserved to materials located presisely at the QCP.

4.6 Summary

In this chapter, the temperature dependence of the low-T in-plane normal state resistivity of FeSe$_{1\text{-}x}$S$_x$ has been studied using strong longitudinally oriented static magnetic fields. A schematic summary of the main findings of this chapter, visualizing the temperature dependence of the resistivity of

$FeSe_{1-x}S_x$ and of the evolution of A^* around x_c is displayed in Fig. 4.11. The observation of a non-Fermi-liquid-like linear-in-T resistivity in the characteristic fan-shaped quantum critical region, together with the evolution of the quasiparticle effective mass (quantified by the modified T^2-coefficient A^*) within the Fermi-liquid region below the fan, implies strongly the existence of a QCP at $x_c = 0.16$. Although the exact mechanisms behind this quantum critical behaviour are not yet known, experimental evidences all suggest that the QCP in the phase diagram of $FeSe_{1-x}S_x$ is purely nematic. It should be noted here that signatures of nematic quantum criticality have been recently reported in another Fe-based material [35]. A detailed theoretical model for electrical transport near an Ising nematic QCP has been developed by Wang and Berg [36], yet still the T-linear resistivity observed here is unaccounted for. This model, based on a memory matrix approach, considers also the effect of the critical fluctuations on the resistivity, through different scattering mechanisms, in a compensated metal and suggests that

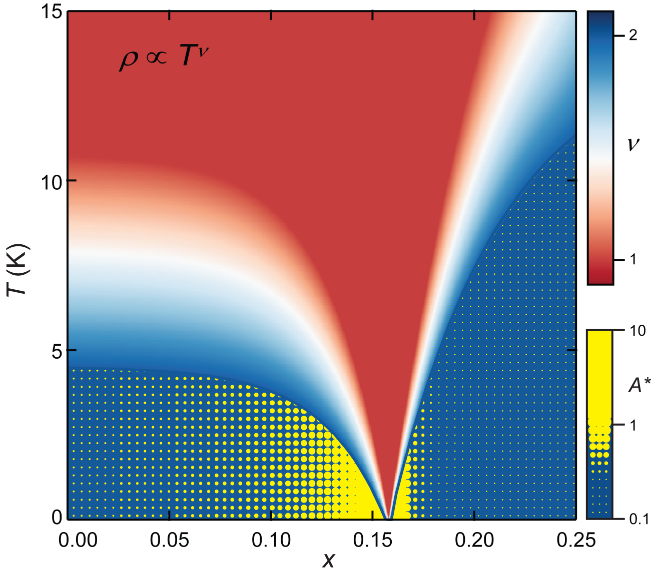

Figure 4.11: The low-T phase diagram of $FeSe_{1-x}S_x$. *Color plot indicating the temperature dependence of the resistivity $\rho \propto T^\nu$. Blue corresponds to T^2 and red to T-linear dependence. The colors in the intermediate region are interpolated. The evolution of A^* is schematically represented below the quantum critical fan by the yellow dots, whose size is logarithmically proportional to the fitting function of Fig. 4.9a.*

the resistivity is strongly affected by the presence of *cold spots* in the Fermi surface, due to the symmetry of the nematic order parameter. At low-T, the predicted behaviour is $\rho \propto T^{\nu}$, with $\nu = 2$, $5/3$ or $4/3$ depending on the location of the cold spots in the FS. Strikingly, no T-linear behaviour is predicted. The fact that a $Q \neq 0$ scenario, possibly mediated by AFQ order [27], is not included in Wang and Berg's model, might suggest that an explanation for the experimentally observed resistivity behaviour lies indeed in that direction, and should stimulate further theoretical work.
Finally, the test of the realization of the Planckian dissipation limit for the scattering rate, places $FeSe_{1-x}S_x$ alongside a host of other quantum critical materials, despite profound differences in their band structures, dimensionality and the origin of their quantum criticality.

References

[1] N. E. Hussey, J. Buhot and S. Licciardello, *Rep. Prog. Phys.* **81** 052501 (2018).

[2] H. v. Löhneysen *et al.*, *Phys. Rev. Lett.* **72** 20, pp. 3262–3265 (1994).

[3] P. Coleman and A. J. Schofield, *Nature* **433**, pp. 226–229 (2005).

[4] K. Kadowaki and S. Woods, *Solid State Commun.* **58** 8, pp. 507–509 (1986).

[5] T. Urata *et al.*, *arXiv* **1608.01044** (2016).

[6] M. L. Amigó *et al.*, *J. Phys. Conf. Ser.* **568** 022005 (2014).

[7] T. Hanaguri *et al.*, *Sci. Adv.* **4** eaar6419 (2018).

[8] N. E. Hussey, *J. Phys. Soc. Japan* **74** 4, pp. 1107–1110 (2005).

[9] A. F. Ioffe and A. R. Regel, *Prog. Semicond.* **4** 237 (1960).

[10] N. F. Mott, *Philos. Mag.* **26** 4, pp. 1015–1026 (1972).

[11] N. E. Hussey, K. Takenaka and H. Takagi, *Philos. Mag.* **84** 27, pp. 2847–2864 (2004).

[12] T. Terashima *et al.*, *Phys. Rev. B* **90** 144517 (2014).

[13] M. D. Watson *et al.*, *Phys. Rev. B* **91** 155106 (2015).

[14] J. Maletz *et al.*, *Phys. Rev. B* **89** 220506(R) (2014).

[15] A. Audouard *et al.*, *Europhys. Lett.* **109** 27003 (2015).

[16] J. Lin *et al.*, *Phys. Rev. B* **84** 220507(R) (2011).

[17] A. E. Böhmer *et al.*, *Phys. Rev. Lett.* **114** 027001 (2015).

[18] F. Hardy *et al.*, *Phys. Rev. B* **99** 035157 (2019).

[19] A. I. Coldea *et al.*, *npj Quantum Mater.* **4** 2 (2019).

[20] D. L. Maslov and A. V. Chubukov, *Phys. Rev. B* **81** 045110 (2010).

[21] K. Matsuura *et al.*, *Nat. Commun.* **8** 1143 (2017).

[22] P. Wiecki *et al.*, *Phys. Rev. B* **96** 180502(R) (2017).

[23] P. Wiecki *et al.*, *Phys. Rev. B* **98** 020507(R) (2018).

[24] D. L. Maslov, V. I. Yudson and A. V. Chubukov, *Phys. Rev. Lett.* **106** 106403 (2011).

[25] S. A. Hartnoll *et al.*, *Phys. Rev. B* **89** 155130 (2014).

[26] S. Lederer *et al.*, *Proc. Natl. Acad. Sci. USA* **114** 41, pp. 4905–4910 (2017).

[27] R. Yu and Q. Si, *Phys. Rev. Lett.* **115** 116401 (2015).

[28] M. C. Rahn *et al.*, *Phys. Rev. B* **91** 180501(R) (2015).

[29] Q. Wang *et al.*, *Nat. Mater.* **15**, pp. 159–163 (2016).

[30] W. L. Zhang *et al.*, *arXiv* **1710.09892** (2018).

[31] J. A. N. Bruin *et al.*, *Science* **339**, pp. 804–807 (2013).

[32] J. Zaanen, *Nature* **430**, pp. 512–513 (2004).

[33] T. Schäfer and D. Teaney, *Rep. Prog. Phys.* **72** 126001 (2009).

[34] A. Legros *et al.*, *Nat. Phys.* **15**, pp. 142–147 (2019).

[35] C. G. Wang *et al.*, *Phys. Rev. Lett.* **121** 167004 (2018).

[36] X. Wang and E. Berg, *arXiv* **1902.04590** (2019).

CHAPTER 5

Two-component transverse magnetoresistance

Abstract

The magnetoresistance of conventional metals is known to vary quadratically with field strength in low magnetic fields and often obeys Kohler's scaling, as inferred from the semiclassical theory of magneto-transport. In contrast, certain quantum critical systems are characterized by a linear-in-H magnetoresistance that obeys a different type of scaling between magnetic field and temperature (quantum critical scaling). Until now, these two distinct magnetoresistance behaviours have been considered to be independent, possibly associated with two opposite limits (far from and close to a QCP). In this chapter, the transverse magnetoresistance of $FeSe_{1-x}S_x$ *is studied through the application of magnetic fields up to 38 T. The coexistence of a conventional orbital component and a quantum critical component is observed, whose dependence on both temperature and sulphur substitution seems to be influenced by the proximity to the nematic QCP. While the quantum critical component appears to survive in the presence of disorder, the orbital component is effectively quenched. This raises the question whether the observation of the latter might have been obscured by disorder in other quantum critical metals.*

Part of the work of this chapter is submitted for publication as: S. Licciardello *et al.*, "Coexistence of orbital and quantum critical magnetoresistance in $FeSe_{1-x}S_x$". Preprint at *arXiv* **1903.05679** (2019).

5.1 Introduction

The magnetoresistance of a given material can be expressed as the ratio $\delta\rho/\rho(0) = \frac{\rho(H)-\rho(0)}{\rho(0)}$, where $\rho(H)$ is the resistivity of the material at a certain temperature under an applied magnetic field H and $\rho(0)$ is the zero-field resistivity at the same temperature. The low-field orbital MR of standard metals usually obeys the so-called Kohler's scaling rule [1]. This rule dictates that ratios $\delta\rho/\rho(0)$ obtained at different temperatures must all collapse onto a single curve when plotted as a function of $\left({}^{H}/_{\rho(0)}\right)^2$. This scaling relation is due to the proportionality $\delta\rho/\rho(0) \propto (\omega_c\tau)^2$, derived from the Boltzmann's theory of transport in magnetic fields; here, $\omega_c = \frac{e\mu_0 H}{m^*}$ is the cyclotron frequency, i.e. the frequency at which the magnetic field $\mu_0 H$ causes the charge carriers to sweep across the Fermi surface. Since $\rho(0) \propto \tau^{-1}$, one obtains $\delta\rho/\rho(0) \propto \left({}^{H}/_{\rho(0)}\right)^2$ [2, 3]. However, Kohler's rule strictly applies only when the scattering time is the same at all points of the FS. The existence of two separate scattering times with distinct temperature dependences, as predicted for example by Anderson in two-dimensional electron fluids [4] and first observed by Ong and co-workers in the cuprate $\mathrm{YBa_2Cu_{3\text{-}x}Zn_xO_{7\text{-}\delta}}$ [5], renders the above treatment inadequate. Further observations of the violation of Kohler's rule in cuprates [6, 7] as well as in quasi-2D organic conductors [8–11], then called for the search of a new, more generally applicable scaling relation. The so-called modified Kohler's rule, according to which plots of $\delta\rho/\rho(0)$ versus $\left({}^{H}/_{\tan(\theta_\mathrm{H})}\right)^2$, with θ_H the Hall angle, collapse onto a single curve, has been found to hold in cuprates [12] and in heavy-fermions [13, 14]. Recently a new type of MR scaling, seemingly peculiar to quantum critical systems, has been discovered in the Fe-pnictide $\mathrm{BaFe_2(As_{1\text{-}x}P_x)_2}$ with $x \approx 0.3$, that is close to the antiferromagnetic QCP where $\rho(T) \propto T$ (see Chap. 1). When subtracted from its zero-field, zero-temperature value obtained by a linear extrapolation of the the low-temperature resitivity, the magneto-resistivity appears to scale simultaneously with temperature and magnetic field [15, 16]. More specifically, the following quadrature scaling relation holds:

$$\Delta\rho = \rho(H,T) - \rho(0,0) \propto \sqrt{(\alpha_0 k_\mathrm{B} T)^2 + (\gamma_0 \mu_\mathrm{B} \mu_0 H)^2}, \tag{5.1}$$

where μ_B is the Bohr magneton and $\alpha_0 \approx \gamma_0 \approx 1$ are dimensional parameters. This implies that, when plotted as a function of $\mu_0 H/T$, curves of $\Delta\rho/T$ will fall on top of each other. A similar form of scaling has been reported in the electron-doped cuprate $La_{2-x}Ce_xCuO_4$, also near its antiferromagnetic QCP [17]. A common feature of these quantum critical systems with a *scale-invariant* MR, is a T-independence of their $\rho(H)$ curves, which at high field constitute a set of parallel straight lines that are simply vertically shifted with respect to each other [15–18]. All materials studied to date are found to exhibit either the quantum critical scaling encompassed in Eq. (5.1) or a quadratic-in-H resistivity (in low to intermediate field strengths), suggesting that these two forms of scaling are incompatible with each other, the former being due to the proximity to a QCP. Any relation with the modified Kohler's scaling is not clear.

In this chapter, a systematic study of the transverse MR of $FeSe_{1-x}S_x$ across the nematic QCP is presented. Two distinct contributions to the MR are observed: a purely H^2-part and a second component which, once the H^2-term is subtracted, is found to follow a quadrature relation of the form of Eq. (5.1). The evolution of these two components across the phase diagram is shown to be regulated by the presence of the QCP. Finally, a comparison of two samples with different disorder levels reveals that the two measured MR components exhibit a very different sensitivity to disorder.

5.2 Transverse MR

All the results shown in this chapter refer to measurements performed in the $\mathbf{H}//c$ experimental configuration, i.e. with the field oriented perpendicular to the conducting planes.

Fig. 5.1a displays a set of MR curves for fields up to 38 T in the temperature interval 1.35-50 K at the nematic QCP $x_c = 0.16$. In contrast to what has been observed in other QC systems, the $\rho(H)$ curves taken at different temperatures do not stack in a parallel fashion with respect to each other, but mutually cross at several points, implying that the MR has a marked temperature dependence. Nonetheless, from Fig. 4.4e of Chap. 4 we can extrapolate the $\rho(0,0)$ value needed to test the quantum critical scaling. The result of this test is shown in Fig. 5.1b. Clearly the $\Delta\rho/T$ curves do not collapse on each other at any temperature. Only in the intermediate T-range 4.2-20 K do they seem to approximate that condition, though even there, the scaling is not of the form displayed in Eq. (5.1). Kohler's rule is also strongly violated at all temperatures, as illustrated in Fig. 5.1c. Therefore, at first glance, neither $\delta\rho$ nor $\Delta\rho$ appear to show any relevant scaling.

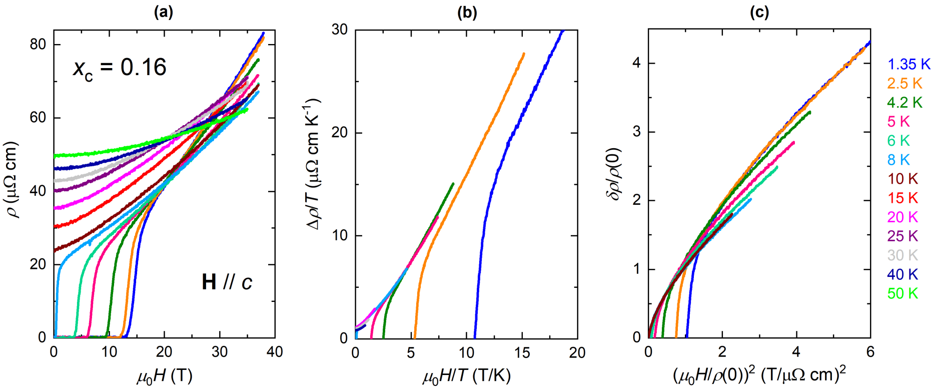

Figure 5.1: Transverse MR of FeSe$_{0.84}$S$_{0.16}$. *(a) Set of* $\rho(H)$ *curves up to* $\mu_0 H = 38\,\mathrm{T}$ *at several temperatures in the interval* $1.35 - 50\,\mathrm{K}$. *(b) Test for quantum critical scaling: plots of* $\Delta\rho/T = \frac{\rho(H,T)-\rho(0,0)}{T}$ *vs.* $\mu_0 H/T$. *(c) Test for Kohler's scaling: plots of* $\delta\rho/\rho(0) = \frac{\rho(H)-\rho(0)}{\rho(0)}$ *vs.* $(\mu_0 H/\rho(0))^2$.

However, this statement can be misleading particularly if one looks more carefully at the specific form of the MR of FeSe$_{1\text{-}x}$S$_x$. This can be done by analysing the field derivatives $d\rho/dH$, as exemplified in Fig. 5.2a-c for $x = 0.1,\ 0.16$ and 0.25 at a temperature ($T = 15\,\mathrm{K}$) at which any superconducting fluctuations have been suppressed. The derivatives exhibit three distinct regimes: a low-field regime ($0\,\mathrm{T} < \mu_0 H \lesssim 2\,\mathrm{T}$) in which the derivative is H-linear and passes through the origin, a high-field regime ($\mu_0 H \gtrsim 7\,\mathrm{T}$) with a linear dependence but a finite intercept, and an intermediate regime between the two. In terms of resistivities, this translates into a strictly H^2-dependence at low fields and a $(H + H^2)$-behaviour at higher fields that persists up to the maximum field strength of 35 T displayed in Fig. 5.2. At lower temperatures, the H-dependence was studied up to even higher fields of 38 T and was found to have the same trend. From the linear fits in panels a-c of Fig. 5.2 (dotted and dashed lines), it is possible to extract the low-H H^2-coefficient of $\rho(H)$ (β_0) as well as the high-H H-linear and H^2-coefficients (β_{QC} and β_{qp}, respectively). If the high-field H^2-terms $\beta_{\mathrm{qp}}(\mu_0 H)^2$ are subtracted from the full range ρ curves, the second component of the MR is revealed (Fig. 5.2d-f). Remarkably, this is found to follow precisely the same quadrature form $\sqrt{1 + (\alpha_1 \mu_0 H)^2}$ that was observed in other quantum critical systems and introduced in § 5.1 (black dotted lines in the figure). It is important to note that the same result was obtained for all studied samples on either side of the QCP, although with different values of the above defined coefficients. A selection of several x values and temperatures is shown in Fig. 5.3. Only for $x = 0$ does the form of the resistivity deviate from $(H + H^2)$ at high field, as exemplified in Fig. 5.4a for $T = 15\,\text{K}$. This behaviour is due to the fact that the transverse MR, being exceptionally large in pure FeSe, goes beyond the low-field limit. Notwithstanding that, the $(H + H^2)$ regime can still be measured at intermediate fields, as indicated by the red dashed line in Fig. 5.4a. Again subtracting off the H^2 dependence, one recovers the quadrature form up to ~7 T (inset of Fig. 5.4b). Moreover, if one assumes that the QC component

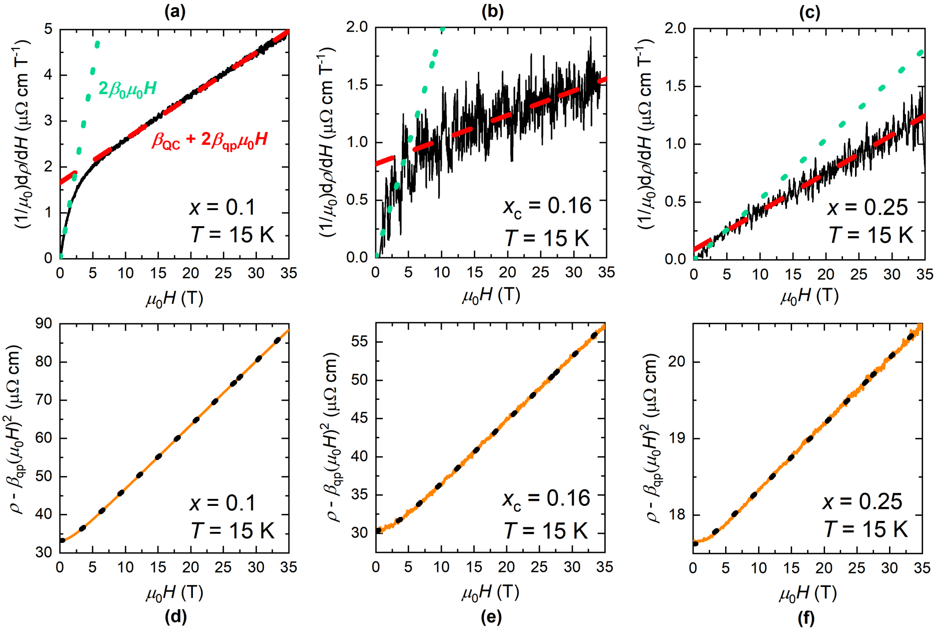

*Figure 5.2: **Distinct low- and high-field MR regimes in FeSe$_{1-x}$S$_x$ – part 1.** Magnetic-field-derivative of the MR curve for (a) $x = 0.1$, (b) $x_c = 0.16$ and (c) $x = 0.25$ at $T = 15\,\text{K}$. The low- and high-field distinct linear regimes are indicated, respectively, by the green dotted lines and the red dashed lines and the relevant coefficients (as defined in the text) are indicated in panel a. Panels d-f display, for the same x values and temperature as in (a)-(c), the quantum critical component of the MR obtained once the high-field H^2-term is subtracted. The black dotted lines are fits to the quadrature expression $\sqrt{1 + (\alpha_1\mu_0H)^2}$.*

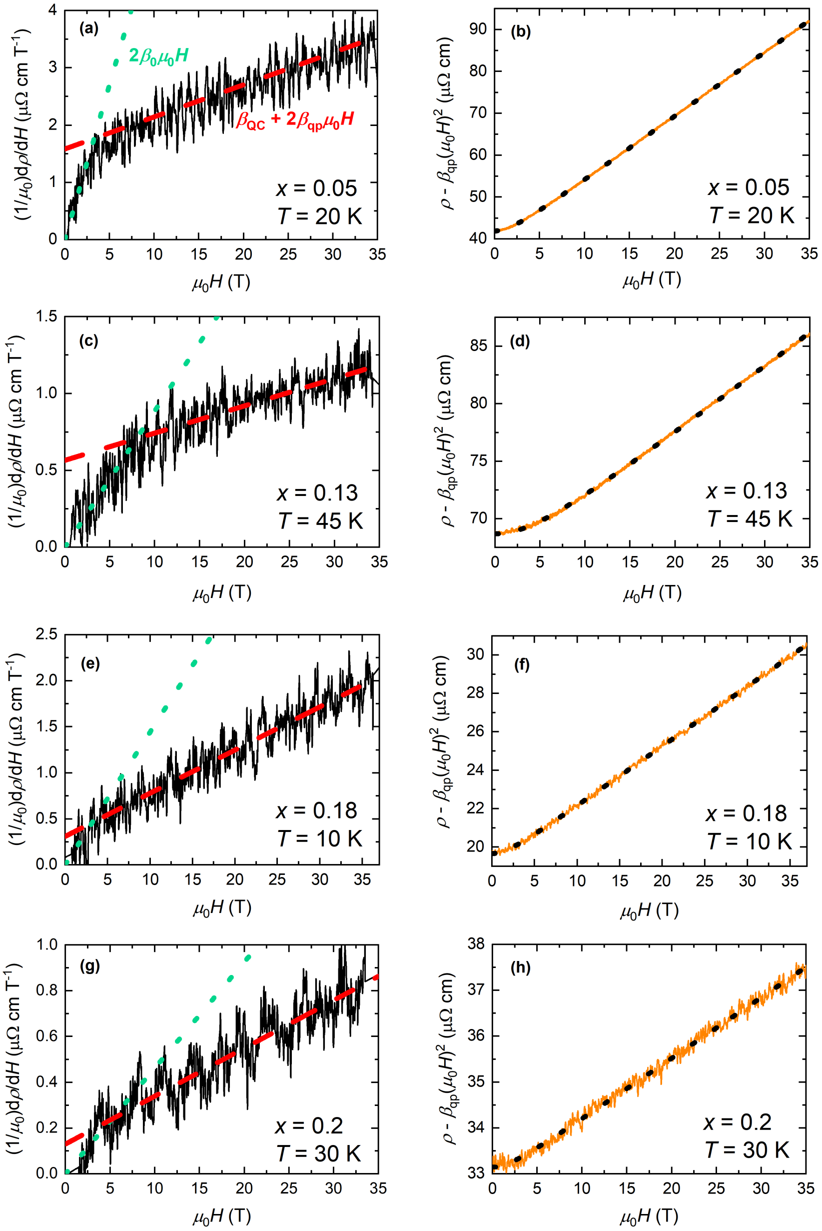

Figure 5.3: Distinct low- and high-field MR regimes in FeSe$_{1\text{-}x}$S$_x$ – part 2. *Magnetic-field-derivative of the MR curve for (a) $x = 0.05$ at $T = 20\,\mathrm{K}$, (c) $x = 0.13$ at $T = 45\,\mathrm{K}$, (e) $x = 0.18$ at $T = 10\,\mathrm{K}$ and (g) $x = 0.2$ at $T = 30\,\mathrm{K}$. Panels b, d, f and h display, for the same combination of x and T (next to the respective derivative curves), the QC component and quadrature fits as in Fig. 5.2.*

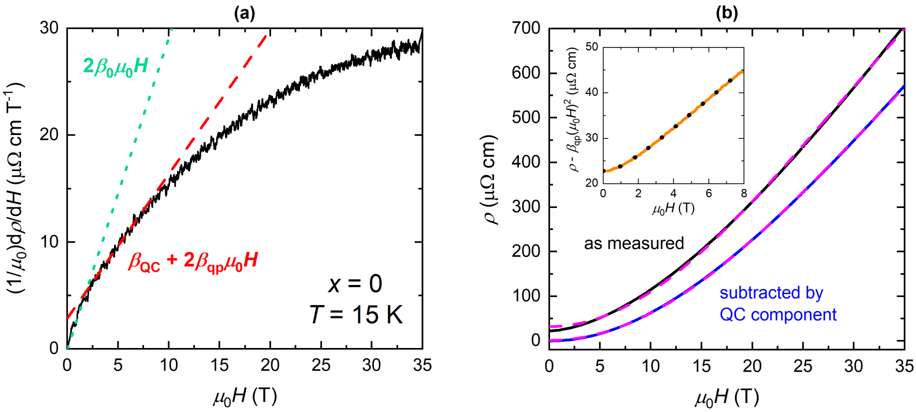

Figure 5.4: Anomalous transverse MR of pure FeSe. *(a) The high-field MR deviates from a* $(H+H^2)$ *behaviour, as exemplified here for* $T = 15\,\mathrm{K}$*. However, the coefficients* β_{QC} *and* β_{qp} *can still be extracted at intermediate fields. As shown in the inset of (b), the QC component of the MR of pure FeSe follows the same quadrature form as all other samples, but only up to ~*$7\,\mathrm{T}$*. The main panel in (b) shows that the MR curve (black) fails to follow a two-carrier model fit of the form* $\frac{c_1(\mu_0 H)^2}{1+c_2(\mu_0 H)^2}$ *(magenta dashed line), but the fit works perfectly once the QC component is subtracted (blue line). We assume that the QC component follows the same form up to* $35\,\mathrm{T}$*.*

obeys the same form in the entire measured field range, the remaining curve can be fitted perfectly to a standard two-carrier (electron-hole) fit to the MR [19, 20], which by contrast, fails to fit the total MR curve (see magenta dashed lines in Fig. 5.4b). Thus, the transverse MR of $FeSe_{1-x}S_x$ has two distinct components, one that is quadratic at all fields (for all $x \neq 0$) and another one that exhibits the quadrature form. The former component is somewhat reminiscent of the conventional metallic MR and is probably due to quasiparticle (qp) transport, while the latter appears to reflect some quantum critical (QC) character similar to what has been reported in $BaFe_2(As_{1-x}P_x)_2$ [15] and $La_{2-x}Ce_xCuO_4$ [17].

5.3 Quasiparticle and quantum critical components

The two MR components emerging from Fig. 5.2 – 5.4 imply that the total zero-field conductivity $\sigma_{\mathrm{tot}} = 1/\rho(0)$ also consists of two components, $\sigma_{\mathrm{tot}}(T) = \sigma_{\mathrm{QC}}(T) + \sigma_{\mathrm{qp}}(T)$. In such a scenario, the transverse magneto-conductance can be expressed as [21]:

$$\frac{\Delta\sigma_{\mathrm{tot}}}{\sigma_{\mathrm{tot}}} = \frac{\sigma_{\mathrm{QC}}}{\sigma_{\mathrm{tot}}}\frac{\Delta\sigma_{\mathrm{QC}}}{\sigma_{\mathrm{QC}}} + \frac{\sigma_{\mathrm{qp}}}{\sigma_{\mathrm{tot}}}\frac{\Delta\sigma_{\mathrm{qp}}}{\sigma_{\mathrm{qp}}}. \tag{5.2}$$

The MR can be obtained by inverting the conductivity tensor [3]:

$$\frac{\delta\rho}{\rho(0)} = -\frac{\Delta\sigma_{\mathrm{tot}}}{\sigma_{\mathrm{tot}}} - \left(\frac{\sigma_{\mathrm{xy}}}{\sigma_{\mathrm{tot}}}\right)^2, \tag{5.3}$$

where $\frac{\sigma_{\mathrm{xy}}}{\sigma_{\mathrm{tot}}} = \tan\theta_{\mathrm{H}}$, with σ_{xy} the Hall conductivity. Hall effect measurements have been carried out on FeSe$_{1\text{-}x}$S$_x$ samples grown in the same conditions as ours [22]. From those data, we can estimate the value of the cancellation term of Eq. (5.3) and compare it with our measured magnetoresistance. In the temperature interval $20\,\mathrm{K} \leq T \leq 50\,\mathrm{K}$, $\tan^2\theta_{\mathrm{H}}$ of $x = 0.17$ is 17-23% of the measured MR and its variation in temperature is ~20%; in the same T-range, the variation of the MR $\delta\rho/\rho(0)$ is 400% for $x = 0.16$ and 500% for $x = 0.18$. Therefore, the magnetoresistance appears to be dominated by the magneto-conductance term. In this case, we can safely neglect the cancellation term in Eq. (5.3) and use Eq. (5.2) to write a new expression for the MR:

$$\frac{\delta\rho}{\rho(0)} = \frac{\sigma_{\mathrm{QC}}}{\sigma_{\mathrm{tot}}}\frac{\delta\rho_{\mathrm{QC}}}{\rho_{\mathrm{QC}}(0)} + \frac{\sigma_{\mathrm{qp}}}{\sigma_{\mathrm{tot}}}\frac{\delta\rho_{\mathrm{qp}}}{\rho_{\mathrm{qp}}(0)}. \tag{5.4}$$

Having in mind that, at high fields, $\delta\rho = \beta_{\mathrm{QC}}\mu_0 H + \beta_{\mathrm{qp}}(\mu_0 H)^2$, we can then obtain:

$$\left(\frac{\sigma_{\mathrm{QC}}}{\sigma_{\mathrm{tot}}}\right)^2 \delta\rho_{\mathrm{QC}} + \left(\frac{\sigma_{\mathrm{qp}}}{\sigma_{\mathrm{tot}}}\right)^2 \delta\rho_{\mathrm{qp}} = \beta_{\mathrm{QC}}\mu_0 H + \beta_{\mathrm{qp}}(\mu_0 H)^2. \tag{5.5}$$

Eq. (5.5) implies that β_{QC} and β_{qp} represent the quantum critical ($\delta\rho_{\mathrm{QC}}$) and the quasiparticle ($\delta\rho_{\mathrm{qp}}$) terms of the total magnetoresistance, weighted by the square of the ratio between the respective conductivity term and the total conductivity.

5.4 Evolution across the phase diagram

Fig. 5.5 displays the evolution of the ratio of the coefficients β_{QC} and β_{qp} across the phase diagram (red circles). $\beta_{\mathrm{QC}}/\beta_{\mathrm{qp}}$ is plotted for each x at $T = 15\,\mathrm{K}$, the temperature at which superconducting fluctuations are supressed in all measured samples. Strikingly, $\beta_{\mathrm{QC}}/\beta_{\mathrm{qp}}$ evolves in a quantitatively similar manner to the coefficient A^* introduced in Chap. 4 and replotted here in Fig. 5.5 for convenience (black squares). Both quantities experience an enhancement at x_{c} and are markedly reduced beyond the QCP. Although they have been obtained from two very different experiments, the consistency shown in their evolution suggests that quantum critical fluctuations are responsible for both the normalized T^2-coefficient and the quadrature scaling form of the MR. In the two following subsections, the temperature dependence of the individual QC and qp components of the MR will be explored in more detail.

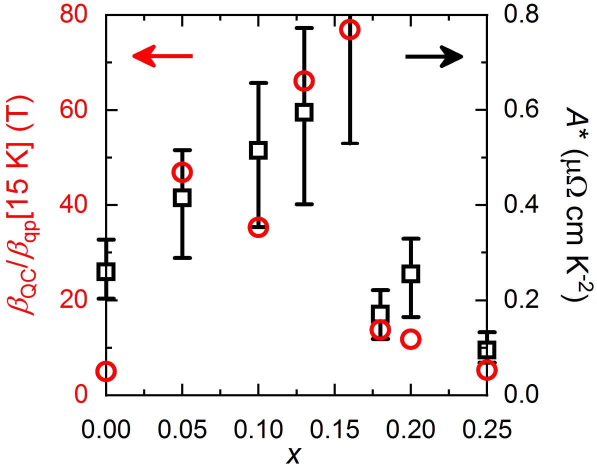

Figure 5.5: ***Mutual relation of the quasiparticle and quantum critical components of the conductivity on either side of the QCP.*** *The open red circles represent the variation of the ratio $\beta_{\mathrm{QC}}/\beta_{qp}$ as a function of x. The values of β_{QC} and β_{qp} for pure FeSe are extracted as illustrated in Fig. 5.4a. The open black squares are the same A^* values as in Fig. 4.9a of Chap. 4, re-plotted here for comparison with $\beta_{\mathrm{QC}}/\beta_{qp}$.*

5.4.1 QC component

As outlined in § 5.1, the quantum critical scaling relation of Eq. (5.1) is satisfied in materials that show an essentially T-independent MR. This condition (holding at high fields) can be expressed as $\Delta\rho_{\mathrm{QC}} = X_1\mu_0 H$, with X_1 a T-independent parameter. In FeSe$_{1\text{-}x}$S$_x$ this equation cannot be tested because, as seen above, the MR consists of two entangled contributions. Nevertheless, three observations strongly support the notion that quantum critical scaling is achieved. First of all, one can note that the QC components of all samples have the very same field dependence at a fixed temperature. This is displayed in Fig. 5.6 for $T = 15\,\mathrm{K}$, where the QC components have been normalized to their value at maximum field. Secondly, the QC components of the MR of an individual sample recorded at several temperatures, if appropriately renormalized, all collapse onto a single curve once the field axis is scaled by the temperature. Finally, as will be discussed in greater detail in § 5.6, a more disordered sample close to the QCP exhibits the same scaling reported in refs. [15–17]. Based on these observations, the

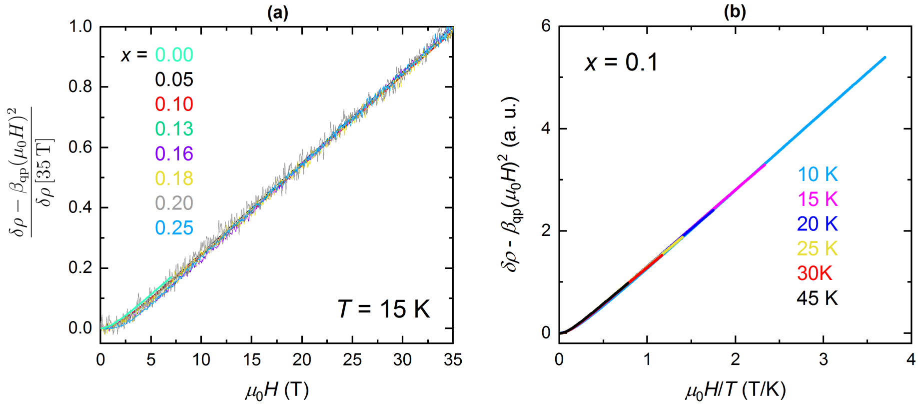

Figure 5.6: Scaling of the magnetoresistance with varying x and T. *(a) The plot is obtained by dividing the QC components of all samples at $T = 15\,\mathrm{K}$ (after the offset $\rho(H = 0)$ has been removed) by their value at $\mu_0 H = 35\,\mathrm{T}$. The curves obtained for all x values (as shown in the legend) all overlap on one another. (b) If x is fixed (here we show $x = 0.1$) the renormalized QC components at different temperatures all collapse onto a single curve when plotted as a function of $\mu_0 H/T$. Curves at $T < 10\,\mathrm{K}$ are not shown because the low-field normal state MR is obscured by superconductivity and therefore there is only a H-linear term left to the QC component.*

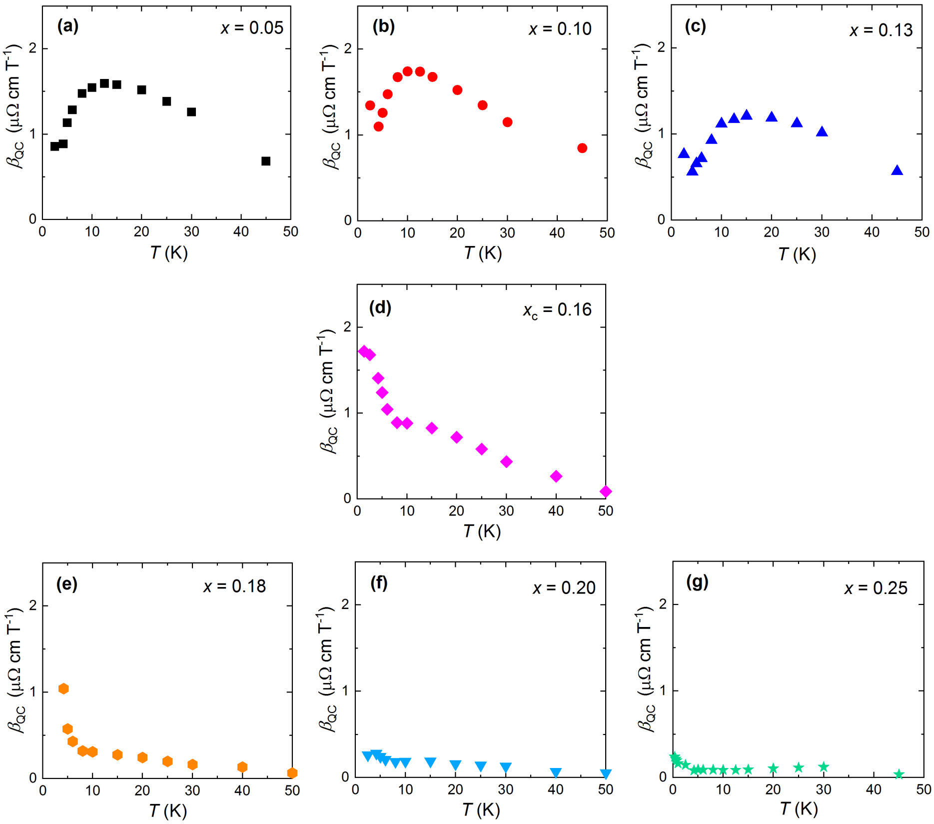

Figure 5.7: Variation with T and x of the QC contribution to the total conductivity. *The H-linear coefficient of the (high-field) MR is plotted as a function of temperature for each all x values except* $x = 0$. *The existence of two distinct behaviours in the two groups (a)-(c) and (e)-(g), parted by the behaviour at the QCP (panel d), is evident.*

assumption that the scaling condition holds for FeSe$_{1\text{-}x}$S$_x$ can be justified. Moreover, since $\Delta\rho$ and $\delta\rho$ only differ by a non-field-dependent intercept, and thus $d(\Delta\rho)/dH = d(\delta\rho)/dH$, the same condition can be applied to $\delta\rho_{\mathrm{QC}}$ as well. This leads to:

$$\beta_{\mathrm{QC}} = \left(\frac{\sigma_{\mathrm{QC}}}{\sigma_{\mathrm{tot}}}\right)^2 X_1. \tag{5.6}$$

The coefficient β_{QC} measures therefore the T-dependence of the ratio of the QC conductivity to the total conductivity (provided that X_1 itself has indeed no intrinsic T-dependence). Fig. 5.7 displays the evolution of $\beta_{\mathrm{QC}}(T)$ for all measured x values. $x = 0$ has been excluded from this figure because of its anomalous MR which implies that β_{QC} and β_{qp} can only be extracted at high-temperatures ($T \geq 10\,\mathrm{K}$), and the former exhibits much larger values than for all the other samples. Clearly, there are two distinct behaviours on opposite sides of the nematic QCP. For $x < x_{\mathrm{c}}$ (top row of Fig. 5.7), that is inside the nematic phase, β_{QC} appears to grow with decreasing temperature inside the quantum critical fan (see Fig. 4.11); at $T \approx 10\,\mathrm{K}$, which is close to T_1 (the temperature above which the resistivity is strictly T-linear, as defined in Chap. 4), β_{QC} experiences a peak, before falling to lower values as the T^2, Fermi-liquid regime of the resistivity is approached. In sharp contrast, at $x = x_{\mathrm{c}}$ (Fig. 5.7d), where the low-T ρ remains T-linear, β_{QC} keeps growing down to the lowest measured temperature. For $x > x_{\mathrm{c}}$ (remaining panels of Fig. 5.7), i.e. outside of the nematic phase, β_{QC} becomes significantly weaker, albeit with a slight upturn at the lowest temperatures. Hence, the evolution of the QC conductivity across the phase diagram is strikingly influenced by the proximity to the QCP.

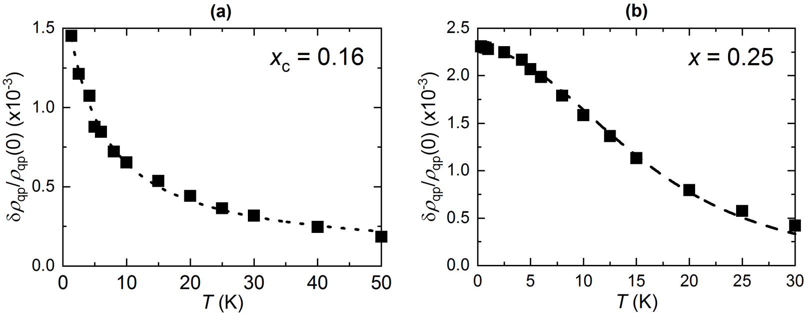

Figure 5.8: Non-Fermi-liquid vs. Fermi-liquid form of the quasiparticle resistivity at and far away from x_c. *T-dependence of $\delta\rho_{qp}/\rho_{qp}(0)$ (at $\mu_0 H = 1\,\mathrm{T}$) for (a) $x_c = 0.16$ and (b) $x = 0.25$. The dotted line in (a) is a guide to the eye, while the dashed line in (b) is a fit to the data to the expression $\delta\rho_{qp}/\rho_{qp}(0) = 1/(A + BT^2)^2$, as expected in a correlated Fermi-liquid.*

5.4.2 qp component

To obtain a measure of the trend of the qp component, one can look at the behaviour of $\delta\rho_{\mathrm{qp}}/\rho_{\mathrm{qp}}(0)$ at $\mu_0 H = 1\,\mathrm{T}$. This is equivalent to the ratio $\frac{\sigma_{\mathrm{qp}}(0)-\sigma_{\mathrm{qp}}}{\sigma_{\mathrm{qp}}}$; the procedure to obtain the estimate of σ_{qp} thereby employed is explained in § 5.5. The temperature dependence of $\delta\rho_{\mathrm{qp}}/\rho_{\mathrm{qp}}(0)$ is shown in Fig. 5.8 for $x = x_{\mathrm{c}}$ and $x = 0.25$. In the latter case, the zero-field resistivity varies quadratically with temperature over a broad temperature range up to 12 K (see again Fig. 4.11). $\delta\rho_{\mathrm{qp}}/\rho_{\mathrm{qp}}(0)$ also follows a Fermi-liquid form, as indicated by the fit to $1/(A + BT^2)^2$ (dashed line in Fig. 5.8b). In contrast, at the QCP, $\delta\rho_{\mathrm{qp}}/\rho_{\mathrm{qp}}(0)$ does not follow any physically relevant form (Fig. 5.8a), presumably due to the predominance of QC fluctuations at this x level.

5.5 Two additive components to the total resistivity

As mentioned in § 5.3, the appearance of two additive components in the magnetoresistance implies that the conductivity, and hence the resistivity, must also be composed of two separate contributions. Based on the above analysis, it is possible to obtain an estimate of the quasiparticle and quantum critical components of the resistivity. Making the assumption that the high-

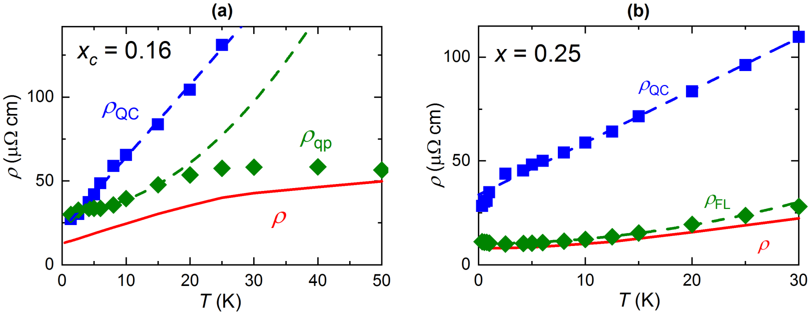

Figure 5.9: ***Deconvolution of the total resistivity into its two primary components.*** *The quantum critical component ρ_{QC} (blue squares) is obtained by inverting Eq. (5.6) and using $X_1 = 2.5$ for $x_c = 0.16$ (panel a) and $X_1 = 1.7$ for $x = 0.25$ (panel b). The quasiparticle component ρ_{qp} (green diamonds) is then obtained by subtracting ρ_{QC} in parallel from the total resistivity ρ (red curves). The blue dashed lines are linear fits and the green dashed lines are quadratic fits.*

field H-dependence of the MR is given by the T-independent parameter X_1, Eq. (5.6) can be employed to calculate $\rho_{\mathrm{QC}} = 1/\sigma_{\mathrm{QC}}$, and subsequently $1/\rho_{\mathrm{qp}} = 1/\rho(0) - 1/\rho_{\mathrm{QC}}$. The only ingredient missing here is the precise value of X_1; however, several scenarios can be tested by tuning X_1 and checking whether a self-consistent picture emerges. Fig. 5.9 shows two such scenarios for $x_{\mathrm{c}} = 0.16$ ($X_1 = 2.5$) and $x = 0.25$ ($X_1 = 1.7$). For both x values, the QC resistivity component (blue squares) is T-linear over a broad temperature range, as indicated by the linear fits (blue dashed lines). The qp component (green diamonds) behaves quadratically in a much broader T-range than the total resistivity (red curve) does. In fact, the as-measured resistivity of $\mathrm{FeSe_{0.84}S_{0.16}}$ never crosses over to T^2 down to the lowest temperatures measured during our experiments; ρ_{qp}, on the other hand, is approximately T^2 up to ~15 K (the green dashed line is a quadratic fit). Similarly for $\mathrm{FeSe_{0.75}S_{0.25}}$, while $\rho(T) \propto T^2$ only for $T \lesssim 12\,\mathrm{K}$, the temperature dependence of ρ_{qp} remains quadratic up to ~30 K, the same temperature range over which $\delta\rho/\rho(0) \propto 1/(A + BT^2)^2$.

5.6 Sensitivity to disorder

A comparison between the data presented in this chapter and other data obtained on a single crystal grown elsewhere and with a different level of disorder, brings into spotlight an interesting evolving pattern of the reciprocal weightings of the quasiparticle and quantum critical components of the magnetoresistance, as a function of increasing impurity scattering. The sample in question has a nominal x value of 0.18 and was grown by N. Maksimovic at the University of California, Berkeley, with the KCl flux technique described in ref. [23]. The sample composition was confirmed by energy dispersive X-ray spectroscopy. The $\rho(T)$ curves (normalized to the room temperature resistivity) of this sample (labelled S018b) and of a sample from the same batch as all samples studied in this thesis (S018a), with the same nominal sulphur content $x = 0.18$, are compared in Fig. 5.10a. The two samples show a similar behaviour, though the residual resistivity $\rho(0)$ of S018b is about five times larger than the one of S018a, implying that the scattering rate is much larger in the former sample. Since the two samples have roughly the same chemical composition, a plausible reason for an enhanced scattering rate is an increased impurity-induced disorder. Fig. 5.10b displays a set of transverse MR curves of sample

S018b acquired at several temperatures in the interval 1.5-80 K. The data shown in this plot were obtained by N. Maksimovic at the National High Magnetic Field Laboratory in Los Alamos in a pulsed magnet with a field strength of 60 T. The MR curves at different T-points are all parallel at high fields and are just shifted vertically with respect to each other. This observation, contrasting with the MR curves with multiple crossing points of our samples (see Fig. 5.1a), suggests that the quantum critical scaling – which, as exemplified in Fig. 5.1b, fails to be followed by our samples – might be realized in sample S018b. It should be specified here that the Berkeley sample is assumed to retain its T-linear resistivity, observed in

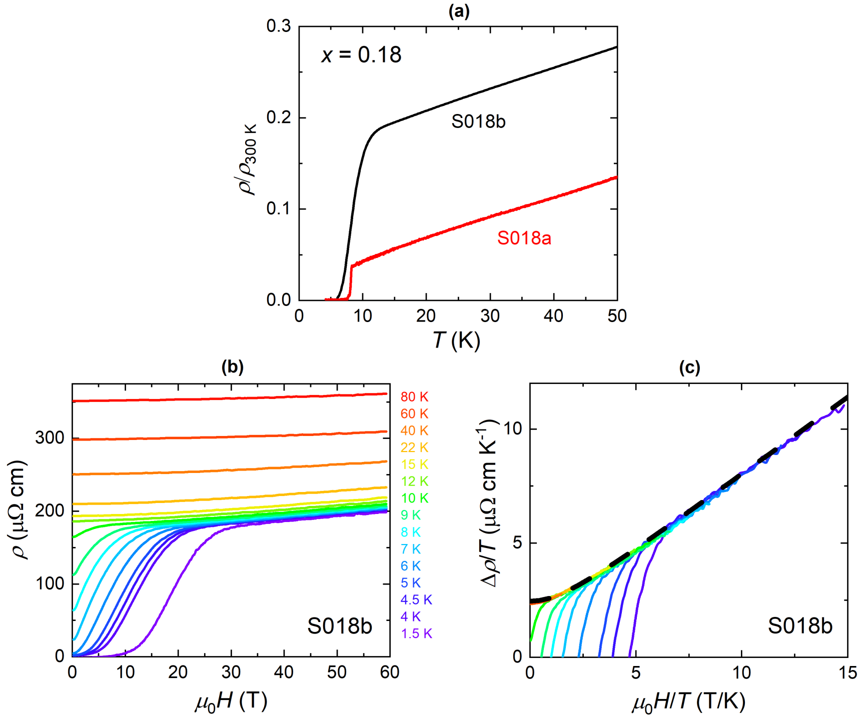

Figure 5.10: Disorder-dependence of QC scaling. *(a) Zero-field resistivity for two* $FeSe_{0.82}S_{0.18}$ *crystals grown with two different methods (see text in this section and § 3.2 of Chap. 3 for details). (b) Set of transverse MR curves of sample S018b up to* $\mu_0 H = 60\,\mathrm{T}$ *at several fixed temperatures. (c) Scaling plot of* $\Delta\rho/T$ *vs.* $\mu_0 H/T$ *for sample S018b. The dashed line is a fit to the quadrature form* $\sqrt{1 + (\alpha_1 \mu_0 H/T)^2}$, *with* $\alpha_1 = 0.5$.

a wide T-range above T_c (see Fig. 5.10a), down to the zero-temperature limit; the $\rho(T = 0, H = 0)$ needed to test the quantum critical scaling is then obtained by extrapolating the linear dependence to $T = 0\,\mathrm{K}$. The QC scaling test for sample S018b is reported in Fig. 5.10c and is found to work extremely well. If plotted against $\mu_0 H/T$, curves of $\Delta\rho/T$ overlap perfectly with one another and their behavior can be described by a fit to the same quadrature form $\sqrt{1 + (\alpha_1 \mu_0 H/T)^2}$ that is observed in the QC component of the MR of sample S018a. The orbital component of the MR, that precludes the observation of quantum critical scaling in the as-measured data of our cleaner samples, seems to have disappeared in the Berkeley sample – *quenched* by disorder. (Note that a five-fold increase in the residual resistivity in S018b corresponds to a 25-fold decrease in the magnitude of the orbital MR.)

5.7 Possible origins of the QC sector in $\mathbf{FeSe_{1\text{-}x}S_x}$

The fact that the quantum critical component of the MR appears to be only weakly affected by disorder, calls for a better theoretical understanding of the underlying physics causing its emergence. Such theories had been in fact stimulated already by the observation of QC scaling in $\mathrm{BaFe_2(As_{1\text{-}x}P_x)_2}$ [15], and have succeeded to reproduce the T-linear resistivity and some aspects of the MR scaling, either based on holography [24] or postulating the existence of a lattice formed by *quantum dots* of localized electrons, which randomly interact with itinerant fermions [25]. However, the coexistence of quantum critical and standard orbital contributions to the magnetoresistance has not been considered previously. Earlier experiments on both semiconductors and simple metals proposed that the observed linear MR in those systems could be due to variations in the Hall voltage along the length of the sample [26, 27], which might in turn arise from variations in the sample thickness [28, 29] or in the carrier density [26, 30]. Similar reasonings are used in ref. [27] to propose an explanation of the MR scaling of Hayes *et al.* [15]. The results presented in this chapter, however, suggest that $\mathrm{FeSe_{1\text{-}x}S_x}$ might belong to a separate category. Fig. 5.5 shows that the QC component strongly dominates over the qp component at the QCP. This behaviour is unlikely to be caused by a difference in carrier density, as the residual resistivities are comparable for all x values (see Fig. 4.4 of Chap. 4), save the exceptional case of pure FeSe. Moreover, the ratio $\beta_{\mathrm{QC}}/\beta_{\mathrm{qp}}$ is roughly the same for $x = 0$ and 0.25, even though their residual resistivities differ by one order of magnitude. The thickness variation scenario can also be excluded because all samples were prepared for experiments in the same way and therefore any variation in the thickness should be randomly present in every sample. Finally, the sharpness of the dips in the temperature derivatives $d\rho/dT$ of the resistivity curves at $T = T_s$ (in low S-doped crystals) strongly suggests that the doping levels in our samples are homogeneous (see Fig. 3.7a-d in Chap. 3).

Taking a cue from Anderson's idea introduced in § 5.1, the composite behaviour of the MR of $FeSe_{1-x}S_x$ may be ascribed to the existence of different excitations, possibly with different scattering times. These excitations could be hosted, for example, by the electron and hole pockets (see Chap. 2 and Chap. 4 for more details on the composition of the Fermi surface of (S-substituted) FeSe) and could give rise to the two observed conductivity components. The two excitations could also be present in both pockets, but generate two distinct scattering mechanisms at different points of the FS, one of which (the *hot spots*) may destroy the quasiparticles. However, this conjecture does not appear to be supported by the observation of QOs in $FeSe_{1-x}S_x$, as presented in Chap. 3 and reported in literature [31–33], inferring the presence of quasiparticle states in both the electron and hole pocket. In light of this, we speculate here that the quantum critical and the conventional quasiparticle characters, might co-exist in all the electronic states close to the Fermi level (like two flip sides of the same coin), though the QC component might only dominate or have a measurable effect on approaching the QCP.

5.8 Summary

In this chapter, clear experimental evidence for two separate, yet coexisting conductivity components in $FeSe_{1-x}S_x$ has been reported. These components are responsible for two distinct – though entangled – responses in the magnetoresistance: one gives rise to the conventional orbital MR, while the other one possesses the character recently uncovered in Fe-pnictide and cuprate superconductors near to their magnetic QCP. In $FeSe_{1-x}S_x$, this quantum critical component is found to persist throughout the whole series, and the way in which it evolves with x appears to be closely linked to the quantum criticality in the system, its strength being maximal at the QCP. Incidentally, unpublished data on our crystals found that the modified Kohler's scaling is close to being obeyed as x_c is approached [22], suggesting a potential link with the quantum critical scaling. The comparison with a more disordered crystal suggests that the QC component is only partially suppressed by increased impurity scattering, in contrast to the orbital component which appears to be fully quenched in the presence of disorder. Existing theories are taken into consideration to explain the coexistence of these two distinct components in the same system, but fail to provide a convincing explanation. Nevertheless, this work supplies a solid starting point for future careful investigations on new quantum critical materials as well as on materials in which the quantum critical scaling is known to be followed, yet in which the observation of an orbital MR component might have been precluded by elevated disorder in the studied samples. The key step now is to identify the origin of this coexistence.

References

[1] M. Kohler, *Ann. Phys.* **424** 211 (1938).

[2] J. M. Ziman, *Electrons and Phonons*, Oxford University Press (1960).

[3] A. B. Pippard, *Magnetoresistance in Metals*, Cambridge University Press (1989).

[4] P. W. Anderson, *Phys. Rev. Lett.* **67** 15, pp. 2092–2094 (1991).

[5] T. R. Chien, Z. Z. Wang and N. P. Ong, *Phys. Rev. Lett.* **67** 15, pp. 2088–2091 (1991).

[6] J. M. Harris *et al.*, *Phys. Rev. Lett.* **75** 7, pp. 1391–1394 (1995).

[7] T. Kimura *et al.*, *Phys. Rev. B* **53** 13, pp. 8733–8742 (1996).

[8] M. Doporto *et al.*, *Phys. Rev. B* **49** 6, pp. 3934–3943 (1994).

[9] A. Audouard *et al.*, *Europhys. Lett.* **34** 8, pp. 599–604 (1996).

[10] A.-K. Klehe *et al.*, *Synth. Met.* **86**, pp. 2003–2004 (1997).

[11] R. H. McKenzie *et al.*, *Phys. Rev. B* **57** 19, pp. 11854–11857 (1998).

[12] A. W. Tyler *et al.*, *Phys. Rev. B* **57** 2, pp. R728–R731 (1998).

[13] Y. Nakajima *et al.*, *J. Phys. Soc. Japan* **76** 024703 (2007).

[14] S. Nair *et al.*, *Adv. Phys.* **61** 5, pp. 583–664 (2012).

[15] I. M. Hayes *et al.*, *Nat. Phys.* **12**, pp. 916–919 (2016).

[16] I. M. Hayes *et al.*, *Phys. Rev. Lett.* **121** 197002 (2018).

[17] T. Sarkar *et al.*, *arXiv* **1810.03499** (2018).

[18] P. Giraldo-Gallo *et al.*, *Science* **361**, pp. 479–481 (2018).

[19] N. W. Ashcroft and N. D. Mermin, *Solid State Physics*, Harcourt College Publishers (1976).

[20] P. M. Rourke *et al.*, *Phys. Rev. B* **82** 020514(R) (2010).

[21] N. E. Hussey *et al.*, *Phys. Rev. B* **57** 9, pp. 5505–5511 (1998).

[22] S. Hosoi and S. Kasahara, *private communication* .

[23] M. W. Ma *et al.*, *Physica C* **506**, pp. 154–157 (2014).

[24] S. Cremonini, A. Hoover and L. Li, *J. High Energ. Phys.* **10** 133 (2017).

[25] A. A. Patel *et al.*, *Phys. Rev. X* **8** 021049 (2018).

[26] R. T. Bate and A. C. Beer, *J. Appl. Phys.* **32** 5, pp. 800–805 (1961).

[27] J. Singleton, *arXiv* **1810.01998** (2018).

[28] G. J. C. L. Bruls *et al.*, *Phys. Rev. Lett.* **46** 8, pp. 553–555 (1981).

[29] G. J. C. L. Bruls *et al.*, *Phys. Rev. B* **32** 4, pp. 1927–1939 (1985).

[30] T. Khouri *et al.*, *Phys. Rev. Lett.* **117** 256601 (2016).

[31] T. Terashima *et al.*, *Phys. Rev. B* **90** 144517 (2014).

[32] M. D. Watson *et al.*, *Phys. Rev. B* **91** 155106 (2015).

[33] A. I. Coldea *et al.*, *npj Quantum Mater.* **4** 2 (2019).

CHAPTER 6

Quantum vortex liquid and FFLO state

Abstract

The vortex liquid state is an intermediate state existing in type-II superconductors at applied magnetic fields between the irreversibility field and the upper critical field. In this state the vortices – non-superconducting droplets surrounded by supercurrent loops – become depinned from their previously fixed sites, causing the resistance of the material to begin to rise above zero. In this chapter, a systematic transport study of the vortex liquid phase of $FeSe_{1\text{-}x}S_x$ *is presented for both longitudinal and transverse applied magnetic fields. At low temperatures, the vortex liquid is found to persist, implying the presence of strong (quantum) fluctuations that depin the vortex solid. This quantum vortex liquid state appears to become more extended for high sulphur content* $x > x_c$*. When the field is applied parallel to the conducting planes, the upper critical field of pure FeSe rises above the Pauli limit, possibly signalling the formation of a so-called FFLO state. Strong nematic fluctuations are proposed as responsible for the observed expansion of the quantum vortex liquid state in* $FeSe_{1\text{-}x}S_x$ *(in the explored x range), and the theoretical requirements for the realization of a FFLO state are tested in FeSe.*

Part of the work presented in this chapter is in preparation for a manuscript.

6.1 Introduction

When an external field is applied to a type-II superconductor, superconductivity can be destroyed by two different, generally concurrent mechanisms: the orbital and the Pauli paramagnetic pair-breaking effects.

The orbital pair-breaking effect induces the formation of the so-called Abrikosov vortices [1] above the lower critical field H_{c1}. When $H < H_{c1}$, the magnetic field is completely expelled from the bulk of the material which remains therefore still fully superconducting (Meissner phase). Above this critical value, the field starts to penetrate into the material, effectively suppressing superconductivity in some regions of it and leading to the formation of the Abrikosov vortices. A vortex can be imagined as a disk-shaped core of normal (i.e. no longer superconducting) metal with radius ~ξ (coherence length) surrounded by a cylinder of radius ~λ (London penetration depth) around which supercurrents flow [2]. Vortices tend to repel each other, resulting in the formation of a periodic lattice (vortex lattice). The vortices, however, are not free to move with respect to each other but are crystallized in the lattice – *pinned* to certain sites, usually defects in the material – and form a vortex solid. If the applied field is not strong enough to overcome the pinning force, the bulk of the material still behaves as a superconductor exhibiting zero resistance. When the field reaches the irreversibility field H_{irr}, the vortex solid melts into a vortex liquid in which the vortices begin to move relatively to one another [3]. The resistance becomes finite and, as the field increases further, the period of the vortex lattice gradually decreases until it becomes of the order of ξ when the applied field reaches the orbital critical value H_{orb}, at which point the normal core regions are forced to overlap and the superconductivity in the material is ultimately destroyed. An empirical formula for the zero-temperature limit of H_{orb} is [4, 5]:

$$H_{orb}(0) = -0.7\,T_c \left.\frac{dH_{c2}}{dT}\right|_{T=T_c}, \tag{6.1}$$

which means that an estimate of $H_{orb}(T{=}0)$ can be obtained from the initial slope of the experimentally determined temperature dependence of the upper critical field H_{c2}.

The Pauli paramagnetic pair-breaking effect originates from the Zeeman splitting of single electron energy levels [6]. In the presence of a magnetic field, electrons in a metal are split into spin-up and spin-down due to the

Zeeman effect. This phenomenon is known as Pauli paramagnetism. In the superconducting state, Cooper pairs are not spin-polarized; thus, when a magnetic field is applied to a superconductor, the pairs must be broken for the electrons to split and the Pauli paramagnetism to occur. The critical field H_P (Pauli limit) at which the pairs are destroyed was first derived by Clogston [7] and Chandrasekhar [8]:

$$H_\mathrm{P} = \frac{\Delta}{\sqrt{2}\mu_\mathrm{B}}. \tag{6.2}$$

The actual upper critical field H_c2 is normally concurrently determined by both mechanisms.

In the zero temperature limit, due to the absence of thermal agitation, the vortex lattice is expected to freeze into a vortex solid or vortex glass phase. In other words, the vortex liquid phase is suppressed in the $T = 0\,\mathrm{K}$ limit and the H_irr and the H_c2 lines converge towards each other. However there can exist quantum fluctuations, in proximity of the zero temperature axis, which can depin the vortices even in the absence of thermal fluctuations, therefore resulting in the formation of a quantum vortex liquid at zero temperature. In § 6.2 – 6.3 of this chapter, the development of a quantum vortex liquid state in $\mathrm{FeSe}_{1\text{-}x}\mathrm{S}_x$ for $x > x_\mathrm{c}$ will be presented and discussed.

Based on the above definition, the Pauli limiting field H_P can be regarded as a theoretical upper bound for H_c2. However, a superconducting state which allows the superconductor to maintain its state above the Pauli limiting field has been predicted in two independent studies by Fulde and Ferrel [9] and by Larkin and Ovchinnikov [10], both in 1964, and adapted to the case of a type-II superconductor a couple of years later [11]. One of the criteria to establish whether this Fulde-Ferrel-Larkin-Ovchinnikov (FFLO) state can actually be achieved in a given superconductor is that H_orb should exceed H_P [12]. This excess is quantified by the so-called Maki parameter [13]:

$$\alpha_\mathrm{M} = \sqrt{2}\frac{H_\mathrm{orb}}{H_\mathrm{P}}. \tag{6.3}$$

In the last part of this chapter (§ 6.4), experimental evidence for a possible FFLO state in pure FeSe – supported by the fulfillment of several criteria, including a large Maki parameter – will be presented.

6.2 Quantum vortex liquid

The properties of the vortex lattice in a type-II superconductor depend on the pinning force present in the material. Several scenarios are schematically illustrated in Fig. 6.1. In the clean limit, i.e. in the absence of defects and hence pinning, no irreversibility field can be defined, but only the lower and upper critical fields. Above H_{c1}, the just formed vortices are unpinned and form a vortex liquid (VL) under applied fields up to H_{c2}. In the presence of strong pinning (the lower critical field will be neglected in the following discussion as the focus will be on the relation between the irreversibility field and the upper critical field), H_{irr} and H_{c2} nearly coincide. Therefore, the VL region is very thin and the vortex solid (VS) below H_{irr} dominates the T-H phase diagram. When pinning is weak, as is often the case in highly anisotropic superconductors, a broad VL phase appears between the irreversibility and the upper critical field lines. However, as mentioned in § 6.1, they nonetheless converge towards one another as

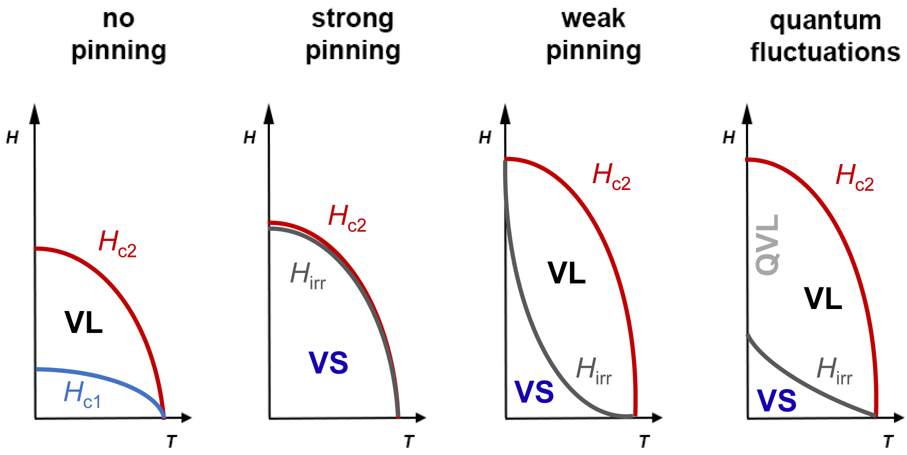

Figure 6.1: Properties of the vortex lattice in type-II superconductors. *Schematic H vs. T phase diagrams showing that, depending on the pinning strength in the material, the vortex lattice can form a vortex solid (VS) or a vortex liquid (VL) in different (T, H) regions. The VL phase, when present, is normally suppressed at zero temperature. When quantum fluctuations are present in the material, the VL can persist down to* 0 K *forming a quantum vortex liquid (QVL).*

$T \to 0\,\mathrm{K}$. An example of this behaviour is illustrated in Fig. 4.3b for FeSe in the field configuration $\mathbf{H}//ab$. Just below T_c, the flux-flow regime is found to extend over a very broad field range. As the temperature scale approaches 0 K, however, the superconducting to normal state transition sharpens up once more, indicating a convergence of the H_{irr} and H_{c2} field scales. Finally, in the presence of strong quantum fluctuations and weak pinning, the vortices can be mobile even in the absence of thermal fluctuations, in which case a quantum vortex liquid (QVL) phase can emerge. The QVL is therefore a very special vortex state, evidence for which has been reported only in a few layered materials, such as the organic superconductor κ-(BEDT-TTF)$_2$Cu(NCS)$_2$ [14] and the cuprate $\mathrm{La}_{2-x}\mathrm{Sr}_x\mathrm{CuO}_4$ [15], when the magnetic field is applied perpendicular to the conducting planes. While the predominance of quantum fluctuations over thermal fluctuations is expected to be responsible for the observed phenomenon, there has been little theoretical work carried out to fully explain its origin.

In the following, evidence for the occurence of a QVL state in $\mathrm{FeSe}_{1\text{-}x}\mathrm{S}_x$ is presented both in the longitudinal ($\mathbf{H}//ab$) and in the transverse ($\mathbf{H}//c$) field orientations, and possible candidates for its origin are examined.

6.2.1 QVL in $\mathrm{FeSe}_{1\text{-}x}\mathrm{S}_x$ ($\mathbf{H}//ab$)

From transport measurements, the H_{irr} and H_{c2} field values in a superconductor at a certain fixed temperature can be defined as, respectively, the field value above which the resistivity becomes finite and the field value above which the superconducting fluctuations are entirely suppressed and the system recovers its normal state, or equivalently the MR assumes its normal state form. As seen in Chap. 4, the longitudinal MR of $\mathrm{FeSe}_{1\text{-}x}\mathrm{S}_x$ is negligible for $x \geq 0.16$ and small and linear for $x < 0.16$, thus making it relatively easy to identify the value of H_{c2}. The procedure for obtaining the irreversibility field and the upper critical field is exemplified in Fig. 6.2 for $x = 0.13$ at $T = 7\,\mathrm{K}$ (panel a) and for $x = 0.25$ at $T = 1.35\,\mathrm{K}$ (panel c). From the field derivative of the MR curves (shown in Fig. 6.2b, d), we can extract H_{irr} as the field value at which the derivative rises above the noise level, and H_{c2} as the field value above which the derivative attains a constant value (within the noise level). Having done this procedure for all the studied samples, plots comparing the values of H_{irr} and H_{c2} as a function of varying temperature can be generated. In Fig. 6.3, such plots are shown for two x values, one inside the nematic phase ($x = 0.13$) and one beyond it ($x = 0.25$).

In both cases, the irreversibility line and the upper critical field line do not appear to converge at low temperature and in the case of $x = 0.25$, H_{irr} does not even reach 50% of the value of H_{c2} at low temperatures. Of course, we do not extend our measurements to the 0 K limit. However, plotting the irreversibility line on a log-linear scale suggests that H_{irr} saturates at a value which is significantly lower than $H_{c2}(0)$ (see inset of Fig. 6.3a). The

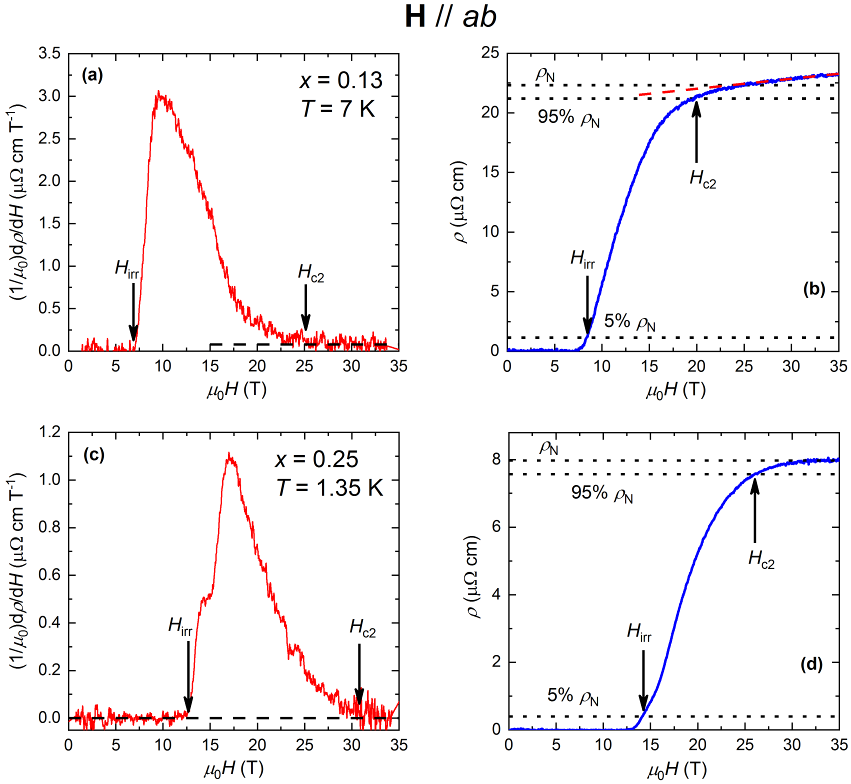

Figure 6.2: Two criteria for the determination of H_{irr} and H_{c2} in a longitudinal magnetic field. *First criterion: the field values are obtained from the field derivatives as explained in the text and indicated here by the arrows. Examples are shown for (a) $x = 0.13$ at $T = 7\,\mathrm{K}$ and (c) $x = 0.25$ at $T = 1.35\,\mathrm{K}$. The error bars are extracted from the noise level of the derivative curves. Panels b and d display the $\rho(H)$ curves from which the derivatives in (a) and (c) are obtained. The dashed line in (b) is a linear fit. The dotted lines define the normal state resistivity ρ_N, 95% and 5% of it. The corresponding field values represent the second criterion for obtaining H_{c2} and H_{irr}.*

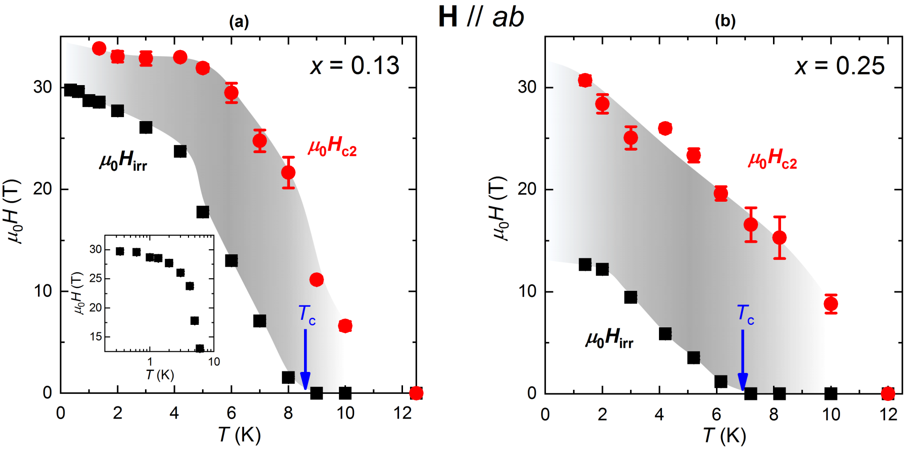

Figure 6.3: Temperature dependence of H_{irr} and H_{c2} in a longitudinal magnetic field. *H_{irr} (black squares) and H_{c2} (red circles) lines for (a) $x = 0.13$ and (b) $x = 0.25$. The vortex liquid (shaded region) persists at the lowest measured temperatures. T_c is indicated by the blue arrow. The inset in (a) displays the temperature dependence of the irreversibility field in a semi-log scale.*

ratios ${}^{H_{\mathrm{irr}}}/_{H_{\mathrm{c2}}}$ for all measured x values are presented in Fig. 6.4. The ratios are plotted at $T = 1.35\,\mathrm{K}$ (blue filled diamonds), the lowest temperature at which the normal state could be reached with the available magnetic field for all samples except $x_{\mathrm{c}} = 0.16$. For this particular sulphur content, $H_{\mathrm{c2}}(1.35\,\mathrm{K})$ was extrapolated by fitting the higher-T values to the expression $H_{\mathrm{c2}}(T) = H^0_{\mathrm{c2}}(1 - T/T_0)^2$, with H^0_{c2} and T_0 fitting parameters. The error bar was estimated by comparison with the higher-T points. The value of ${}^{H_{\mathrm{irr}}}/_{H_{\mathrm{c2}}}$ experimentally obtained at $T = 2.1\,\mathrm{K}$ is also shown for x_{c} in the figure (grey filled hexagon). For the two lowest x values, the ratio is also plotted at a lower temperature (green filled symbols), though still high enough for our maximal field to fully suppress any superconducting fluctuations. The ratios obtained at different temperatures are sufficiently close to each other in all three cases, suggesting that the observed effect is not an artefact of the measurement temperature being too high. Thus, we can be confident that they represent the zero temperature ratios ${}^{H_{\mathrm{irr}}(0)}/_{H_{\mathrm{c2}}(0)}$. The empty symbols in Fig. 6.4 represent the ratios ${}^{H_{\mathrm{irr}}}/_{H_{\mathrm{c2}}}$ obtained using a different definition for H_{irr} and H_{c2}. After defining the normal state resistivity ρ_{N} as the constant high-field ρ value for $x \geq x_{\mathrm{c}}$ and as the lowest ρ value at which $\rho \propto H$ (i.e. the normal state MR form) for $x < x_{\mathrm{c}}$, one can define H_{c2} as the field

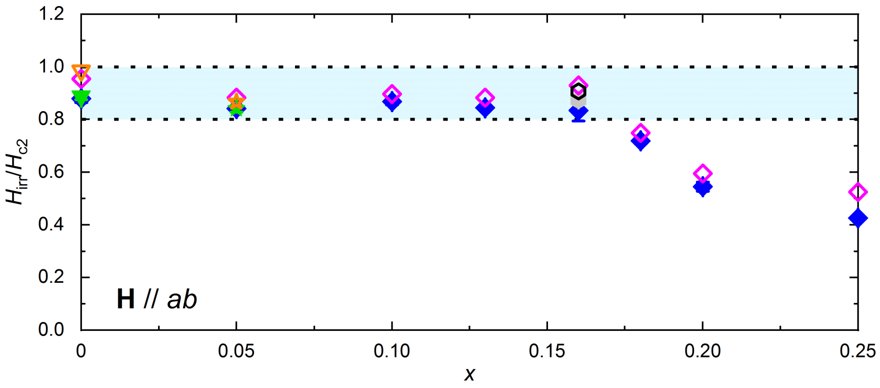

Figure 6.4: Development of a QVL state outside of the nematic phase in a longitudinal magnetic field. *Ratios $^{H_{irr}}/_{H_{c2}}$ calculated at different temperatures using the first (filled symbols) and second (empty symbols) criterion from Fig. 6.2. Hexagons: $T = 2.1\,\mathrm{K}$; diamonds: $T = 1.35\,\mathrm{K}$; stars: $T = 0.9\,\mathrm{K}$; inverted triangles: $T = 0.33\,\mathrm{K}$. The shaded region defines the condition $H_{irr}(0) = 0.8 - 1.0\,H_{c2}(0)$.*

value at which $\rho = 95\%\,\rho_N$ and H_{irr} as the field value at which $\rho = 5\%\,\rho_N$. This alternative procedure is illustrated in Fig. 6.2b, d. Fig. 6.4 shows that the separation between H_{irr} and H_{c2} is always present (the ratio is always smaller than 1), regardless of the criterion used to obtain the field values. For x values inside of the nematic phase, $H_{irr}(0) \approx 0.9H_{c2}(0)$. Once outside of the nematic phase, however, $^{H_{irr}(0)}/_{H_{c2}(0)}$ falls significantly and reaches a value about one half of its initial value for $x = 0.25$. In other words, a low-T vortex liquid state develops for $x > x_c$ and its extent appears to grow until at least $x = 0.25$.

6.2.2 QVL in FeSe$_{1\text{-}x}$S$_x$ ($\mathbf{H}//c$)

In the transverse magnetic field orientation, the MR of FeSe$_{1\text{-}x}$S$_x$ assumes the form presented and discussed in Chap. 5. Due to the large, positive MR and its unusual multi-component field dependence, the identification of a precise value for H_{c2} is less straightforward than in the longitudinal field orientation. Nevertheless, examining the field derivatives of the MR curves, it is reasonable to define H_{c2} as the inflection point, as indicated in Fig. 6.5a for $x = 0.13$ at $T = 6\,\mathrm{K}$ and in Fig. 6.5c for $x = 0.25$ at $T = 1.35\,\mathrm{K}$. The corresponding $\rho(H)$ curves are plotted in Fig. 6.5b, d. At the lowest measured temperatures, due to the presence of SdH oscillations (see Chap. 3), it is not possible to obtain a reliable estimate of H_{c2} (especially for $x < x_c$, where the oscillations are more prominent). Nonetheless, H_{c2} could still be determined down to 1.35 K for all x except $x = 0$. H_{irr}, on the other hand, can be determined unambiguously down to the lowest temperatures

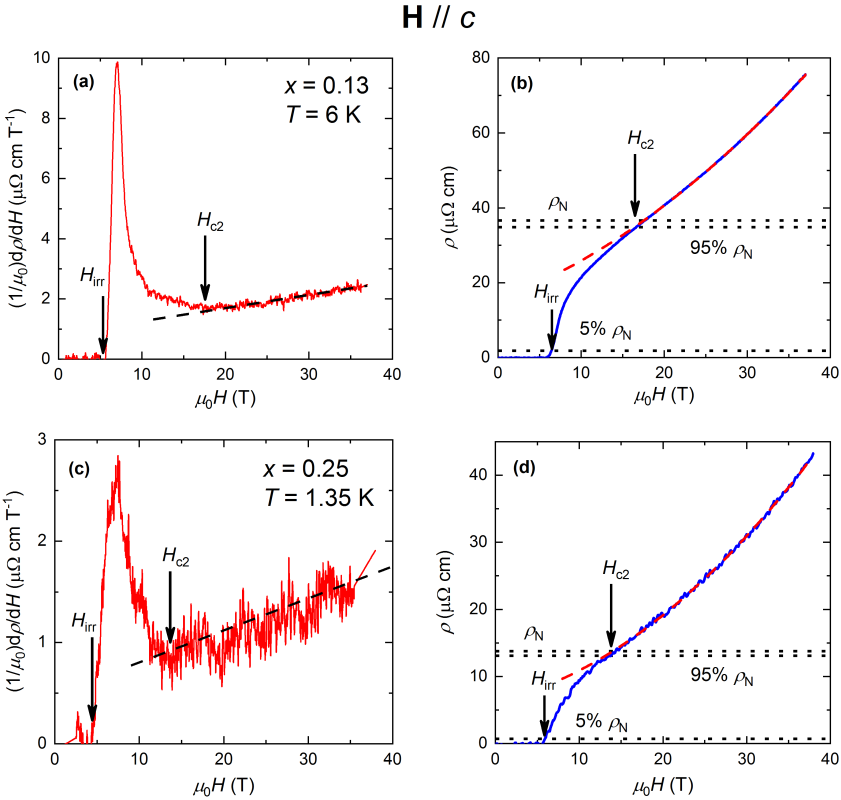

Figure 6.5: Two criteria for the determination of H_{irr} and H_{c2} in a transverse magnetic field. *First criterion: the field values are obtained from the field derivatives as explained in the text and indicated here by the arrows. Examples are shown for (a) $x = 0.13$ at $T = 6\,\mathrm{K}$ and (c) $x = 0.25$ at $T = 1.35\,\mathrm{K}$. The error bars are extracted from the noise level of the derivative curves. Panels b and d display the $\rho(H)$ curves from which the derivatives in (a) and (c) are obtained. The dashed lines are fits to the second order polynomial form $(H + H^2)$. The dotted lines define the normal state resistivity ρ_N, 95% and 5% of it. The corresponding field values represent the second criterion for obtaining H_{c2} and H_{irr}.*

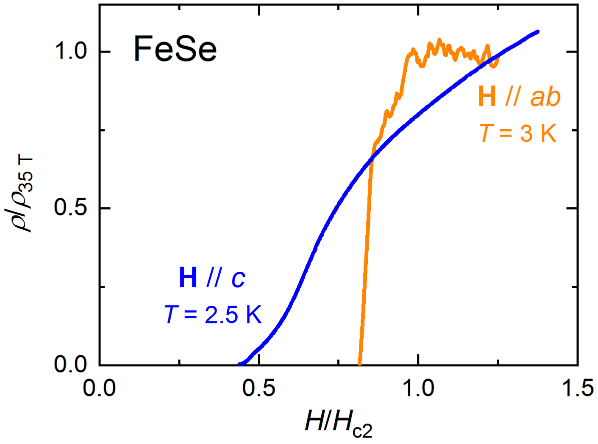

Figure 6.6: Comparison of the longitudinal and transverse MR of FeSe. *$\rho(H)$ curves for $H//ab$ at $3\,\mathrm{K}$ (orange) and $H//c$ at $2.5\,\mathrm{K}$ (blue), normalized to their respective $35\,\mathrm{T}$ value. The H-axis is scaled by the H_{c2} values of the two displayed MR curves.*

of our experiments ($T = 0.33$ K). For pure FeSe, SdH oscillations prevent an accurate determination of H_{c2} at temperatures lower than 2.5 K. By comparing the low-T MR of FeSe in the two different field configurations, we can conclude that the field broadening of $\rho(H)$ for $H//c$ is genuinely due to an enhancement of the vortex liquid phase rather than to inhomogeneity in the samples. Such a comparison is shown in Fig. 6.6 at two very similar temperatures. For $H//c$, H_{irr} is about 40% of H_{c2} at $T = 2.5\,\mathrm{K}$, while for $H//ab$ H_{irr} is 80% of H_{c2} (at lower temperatures the superconducting to normal state transition becomes even sharper). Fig. 6.7 shows paradigmatic H-T diagrams obtained with $\mathbf{H}//c$ for the same crystals presented in Fig. 6.3. In contrast to what is observed in longitudinal fields, a QVL state appears in transverse fields even for $x = 0.13$ while for the higher S concentration $x = 0.25$ the extent of the QVL state is greater than found for $\mathbf{H}//ab$. The resultant ratios $^{H_{\text{irr}}}/_{H_{c2}}$ are plotted for all measured samples in Fig. 6.8. The ratio is shown at $T = 2.5\,\mathrm{K}$ for pure FeSe (grey filled hexagon) and at $T = 1.35\,\mathrm{K}$ for all other x values (blue filled diamonds). For some samples, $^{H_{\text{irr}}}/_{H_{c2}}$ at 0.4 K or 0.33 K is also plotted (green filled triangles and inverted triangles, respectively). Again, the reasonable vicinity of data points obtained at different temperatures allows us to identify the ratios

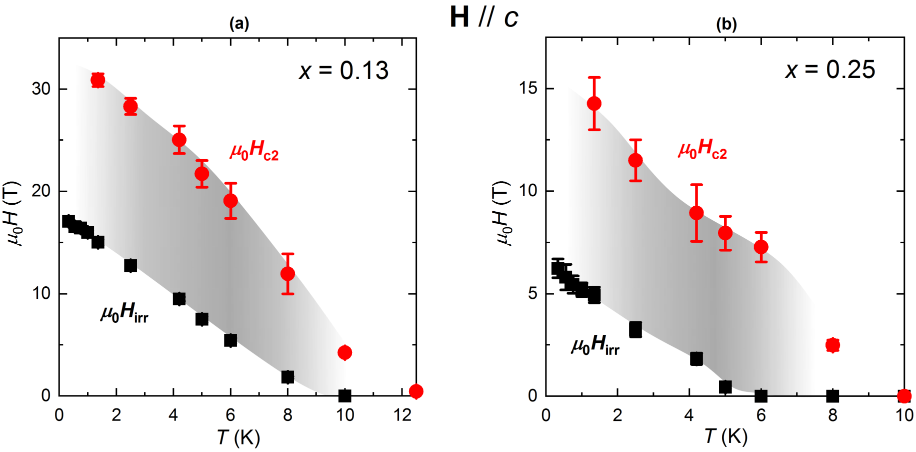

Figure 6.7: Temperature dependence of H_{irr} and H_{c2} in a transverse magnetic field. *H_{irr} (black squares) and H_{c2} (red circles) lines for (a) $x = 0.13$ and (b) $x = 0.25$. Also with this field orientation, the vortex liquid (shaded region) persists down to the lowest measured temperatures.*

with their 0 K value. Similarly to $\mathbf{H}//ab$, a second criterion to calculate the ratio has been employed. The procedure is illustrated in Fig. 6.5b, d. ρ_{N} is defined this time as the resistivity value at the field at which the MR begins to attain its (high-field) normal state $(H + H^2)$-behaviour (dashed red lines in figure). Then, H_{irr} and H_{c2} can be again defined as the field values at which, respectively, $\rho = 5\%\ \rho_{\mathrm{N}}$ and $\rho = 95\%\ \rho_{\mathrm{N}}$. The ${}^{H_{\mathrm{irr}}}/_{H_{\mathrm{c2}}}$ values obtained with this second criterion are represented by the empty symbols in Fig. 6.8. The most significant difference from the $\mathbf{H}//ab$ data is the observation that the quantum vortex liquid state is already present inside the nematic phase, though once again it becomes more enhanced beyond $x = x_{\mathrm{c}}$.

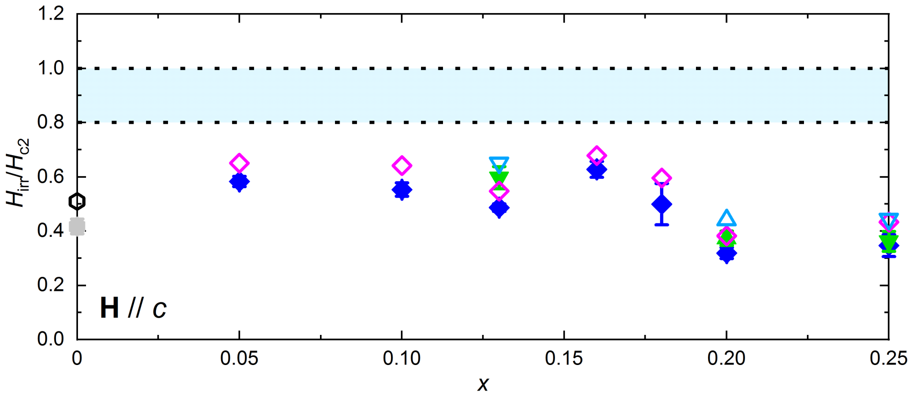

Figure 6.8: QVL state across the phase diagram in a transverse magnetic field. *Ratios* $^{H_{irr}}/_{H_{c2}}$ *calculated at different temperatures using the first (filled symbols) and second (empty symbols) criterion from Fig. 6.5. Hexagons:* $T = 2.5\,\mathrm{K}$*; diamonds:* $T = 1.35\,\mathrm{K}$*; triangles:* $T = 0.4\,\mathrm{K}$*; inverted triangles:* $T = 0.33\,\mathrm{K}$*. The shaded region defines the condition* $H_{irr}(0) = 0.8 - 1.0\,H_{c2}(0)$.

6.3 Discussion on the nature of the QVL phase

The observation of a low-T vortex liquid phase both in the longitudinal and transverse field orientations, has been previously reported in Cu_xTiSe_2 [16], although there, the authors did not regard the phenomenon as evidence of a QVL. Rather, the large width of the vortex liquid phase was attributed to weak, doping-independent pinning forces inside the vortex solid. In FeSe, vortex pinning is strong and is enhanced by S substitution [17], yet the QVL state develops at high x values.

FeSe has recently been argued to be at the BCS-BEC crossover [18, 19], a regime of superconductivity in which the realization of unusual phenomena is expected. Superconductors at the BCS-BEC crossover are located at the *border* between the Bardeen-Cooper-Schrieffer (BCS) coupling state of weakly bound Cooper pairs [20] and the Bose-Einstein condensate (BEC) of strongly coupled electrons which condense into a coherent quantum state [21]. A criterion to establish whether a superconductor is located at the BCS-BEC crossover is the ratio between its superconducting gap and its Fermi energy. At the crossover regime $^{\Delta}/_{E_F}$~1 [22]. The vast majority of known superconductors are located deep within the BCS limit ($^{\Delta}/_{E_F}$«1). For FeSe, although the experimental results supporting its location at the BCS-

x	0	0.05	0.1	0.13	0.16	0.18	0.2	0.25
Δ (meV) [26]	2.4	2.4	2.4	2.3	1.9	1.6	1.4	1.3
E_F (meV)	10	9	9	8	< 6	20	20	40
Δ/E_F	0.24	0.27	0.27	0.29	> 0.30	0.08	0.07	0.03

Table 6.1: *Estimated values of the superconducting gap to Fermi energy ratios of all measured crystals.*

BEC crossover are still very limited, several probes such as QOs [23, 24], ARPES [24] and STM [25, 26] have all independently revealed E_F to be of the order of 10 meV, compared to a superconducting gap magnitude of around 2-3 meV [26–28], yielding a Δ/E_F ratio of about $1/5$. Based on calculations presented in Chap. 4 for the Fermi wavevector k_F and the quasiparticle effective mass m^*, it is possible from our data to obtain an estimate of the Fermi energy $E_F = \frac{\hbar^2 k_F^2}{2m^*}$; then, using the average superconducting gap values measured in ref. [26], we can obtain an estimate of the ratio Δ/E_F for the entire $FeSe_{1-x}S_x$ series. The results are listed in Table 6.1. E_F (Δ/E_F) for $FeSe_{0.84}S_{0.16}$ is an upper (lower) limit obtained from the lower limit for the A coefficient. The ratio, initially slightly increasing towards a value of 0.30, becomes progressively smaller for $x > x_c$, reaching a value that is almost ten times smaller in $x = 0.25$ than in $x = 0$. This suggests that, although $FeSe_{1-x}S_x$ might well be located in close proximity to the BCS-BEC crossover at low x values, with S substitution the system moves away from the crossover regime, dismissing it as a possible origin of the development of a QVL phase above x_c.

A more plausible scenario can be proposed by supposing the existence of strong fluctuations in the region of the phase diagram where the QVL is observed. In $La_{2-x}Sr_xCuO_4$ a low-T vortex liquid phase is formed in the underdoped region [15], close to the antiferromagnetic end point, where antiferromagnetic fluctuations are strong. In $FeSe_{1-x}S_x$, there is evidence for both magnetic and nematic fluctuations across the relevant portion of the phase diagram. Recently, nematic fluctuations have been reported in FeSe up to room temperature [29], far away from T_s, suggesting that fluctuations might persist similarly in the sulphur concentration axis far away from the nematic phase. Moreover, as discussed earlier in this thesis, magnetic fluctuations in FeSe [30, 31], although they are progressively suppressed by S doping [32], might play a role at low x values; similarly, the pressure-induced SDW phase [33] moves farther away from the ambient pressure axis as x grows [34], but its fluctuations might still have an influence at low x. Quantum critical fluctuations are also present throughout the series, but grow in the opposite direction, that is towards the QCP. The diminishing strength of the magnetic fluctuations might be then counterbalanced by the growing strength of the quantum critical fluctuations, resulting in an effective suppression of the QVL state as x approaches x_c. Once the magnetic fluctuations have become weaker with increasing x, the nematic fluctuations might be strong enough then to induce the QVL state above x_c. Fig. 6.9 displays a comparison of the results in the two different field orientations. As x increases further beyond 0.25, the nematic fluctuations strength is expected to be progressively reduced, until the QVL state might presumably disappear in FeS. It should also be noted here that the pinning force in $FeSe_{1-x}S_x$ is expected to be suppressed for $x > x_c$. Indeed, the pinning force

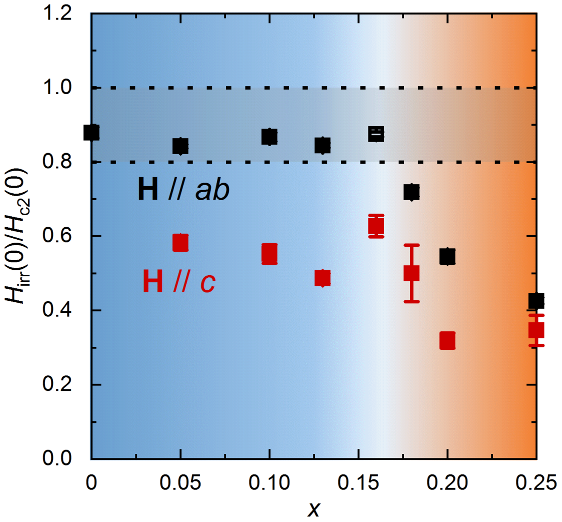

*Figure 6.9: **Evolution of the quantum vortex liquid state in both field orientations.** $^{H_{irr}(0)}/_{H_{c2}(0)}$ for applied longitudinal (black symbols) and transverse (red symbols) magnetic fields. The values shown refer to $T = 1.35\,\mathrm{K}$. For consistency, no value is displayed for pure FeSe in the $\mathbf{H}//c$ configuration, since in that case the lowest temperature at which $^{H_{irr}}/_{H_{c2}}$ could be obtained is $2.5\,\mathrm{K}$. The shaded region defines the condition $H_{irr}(0) = 0.8 - 1.0\,H_{c2}(0)$.*

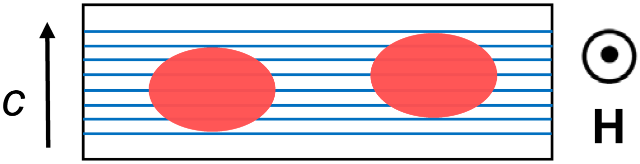

Figure 6.10: Enhanced pinning due to the layered structure for H//ab. *Sketch showing the position of the vortices (red ellipses) in a longitudinal applied field. The Fe-Se(S) layers are represented by the horizontal blue lines. The shape of the vortices is elliptical because of the anisotropy in the coherence length ξ, attested by the anisotropy in H_{c2} (see Chap. 3) and quantified by Eq. (6.4).*

is generally proportional to the square of Δ [35], which itself at $x = 0.25$ is reduced to about half of its initial value at $x = 0$ (see Table 6.1); therefore, the pinning force should drop by roughly a factor four above x_c.
Another interesting aspect of the findings of § 6.2.1, 6.2.2 is the different behaviour of the vortex liquid in FeSe$_{1\text{-}x}$S$_x$ below x_c in the two different field orientations studied. If in a longitudinal field the QVL state is basically absent inside the nematic phase ($^{H_{\mathrm{irr}}(0)}/_{H_{c2}(0)} \lesssim 1$), in a transverse field it is found to be already present and stable ($^{H_{\mathrm{irr}}(0)}/_{H_{c2}(0)} \approx 0.6$). This phenomenon might be explained by an enhanced pinning strength arising from the layered structure of the material, when the field is applied along the ab-plane. This is sketched in Fig. 6.10. The lamellar structure can act as an additional pinning center for the vortices (red ellipses), whose movement along the c-axis is limited by the presence of the Fe-Se(S) layers (blue horizontal lines). In a transverse field, the vortices lie in the planes and therefore are not expected to experience this extra pinning. Then, the less prominent fall of the ratio $^{H_{\mathrm{irr}}(0)}/_{H_{c2}(0)}$ at $x > x_c$ for $\mathbf{H}//c$ than for $\mathbf{H}//ab$ could be a consequence of this effect.

6.4 Possible FFLO state in FeSe for H//*ab*

The FFLO state is a low-temperature spatially modulated superconducting state at magnetic fields higher than the Pauli limiting field H_P. Despite its theoretical prediction in the early sixties, experimental evidence for its existence was reported only in the years 2000 in the heavy fermion system CeCoIn$_5$ [36, 37], and a few years later in the organic compound κ-(BEDT-TTF)$_2$Cu(NCS)$_2$ [38–42]. The FFLO state can occur in layered materials when the applied magnetic field is parallel to the layers and a number of additional requirements are satisfied [12]. First of all, the Maki parameter α_M (see Eq. (6.3)) should exceed the value of 1.8 [11]. Secondly, the superconductor should be in the ultra-clean limit, meaning that the mean free path ℓ should be much larger than the coherence length ξ. One

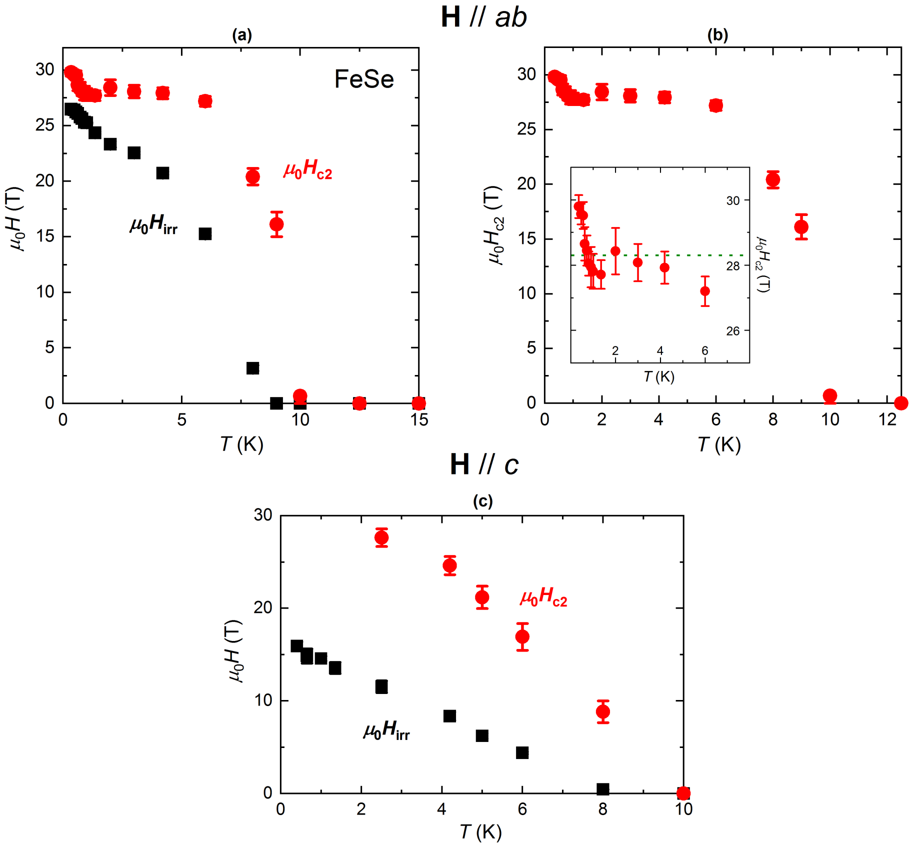

Figure 6.11: ***FFLO state in FeSe in a longitudinal magnetic field.*** *(a) Evolution of H_{irr} (black squares) and H_{c2} (red circles). (b) Temperature dependence of H_{c2}. The inset displays a zoom-in of the low-temperature region. The olive dotted line emphasizes the sharp low-T increase of H_{c2}. (c) Evolution of H_{irr} and H_{c2} of FeSe in a transverse magnetic field.*

manifestation of the FFLO state is a low-temperature enhancement of H_{c2} above the Pauli limit H_{P}.

Fig. 6.11a shows the temperature dependence of H_{irr} and H_{c2} in a longitudinal magnetic field for pure FeSe. For temperatures below ~1.35 K, the upper critical field exhibits a small but sharp increase and reaches a value just above 30 T at $T = 0.33$ K. This low-T enhancement is more clearly visible when plotting H_{c2} alone as a function of temperature and expanding the region below ~8 K (Fig. 6.11b). Using Eq. (6.2) with $\Delta \approx 2.4$ meV from Table 6.1, we obtain the estimate $H_{\mathrm{P}} \approx 29$ T for pure FeSe. The enhancement above the Pauli limit is therefore rather small but, in the following, the two theoretical criteria for the realization of the FFLO state are shown to be met. After calculating the orbital critical field H_{orb} from Eq. (6.1), we obtain $\alpha_{\mathrm{M}} \approx 5$, far exceeding the minimum value of 1.8. Due to the electrical anisotropy of FeSe, the in-plane and out-of-plane coherence lengths ξ_{ab} and ξ_{c} enter into the formulae for $H_{\mathrm{c2}}(0)$ [43]:

$$H_{\mathrm{c2}}^{//c}(0) = \frac{\Phi_0}{2\pi\xi_{\mathrm{ab}}^2} \tag{6.4a}$$

$$H_{\mathrm{c2}}^{//ab}(0) = \frac{\Phi_0}{2\pi\xi_{\mathrm{ab}}\xi_{\mathrm{c}}}, \tag{6.4b}$$

where $\Phi_0 = h/2e$ is the magnetic flux quantum. As explained in § 6.2.2, the lowest temperature at which we could determine $H_{\mathrm{c2}}^{//c}$ with confidence is 2.5 K (see Fig. 6.11c). For consistency, we will use here the value of $H_{\mathrm{c2}}^{//ab}$ at that same temperature. The coherence lengths will be therefore slightly overestimated. Using $H_{\mathrm{c2}}^{//c}(2.5\,\mathrm{K}) = 27.6\,\mathrm{T}$ and $H_{\mathrm{c2}}^{//ab}(2.5\,\mathrm{K}) = 28.4\,\mathrm{T}$ gives $\xi_{\mathrm{ab}} \approx 3.45\,\mathrm{nm}$ and $\xi_{\mathrm{c}} \approx 3.36\,\mathrm{nm}$. The average value $\bar{\xi} = 3.4\,\mathrm{nm}$ will be employed in the following. A formula for the mean free path ℓ can be obtained from the Drude expression that was already employed in Chap. 4 to obtatin Eq. (4.4). Considering that $\ell = v_{\mathrm{F}}\tau$ and assuming that the two Fermi pockets of FeSe are perfectly compensated and have the same wavevector $k_{\mathrm{F}} = 1.07\,\mathrm{nm}^{-1}$ and the same mean free path (isotropical approximation), we get:

$$\ell = \frac{\pi c\hbar}{Ne^2 k_{\mathrm{F}}\rho_0}, \tag{6.5}$$

where ρ_0 is the residual resistivity. Using the value $\rho_0 = 0.4\,\mu\Omega\,\mathrm{cm}$ (see Fig. 4.4a of Chap. 4) gives $\ell \approx 850\,\mathrm{nm}$. Consequently we obtain a lower estimate $\ell/\bar{\xi} \approx 250$, a large number implying that our FeSe crystals are ultra-clean superconductors.

The above arguments suggest that the observed upturn in H_{c2} could in fact be the manifestation of a FFLO state in pure FeSe. Its occurrence only in pure FeSe is probably due to the increased level of disorder present as soon as sulphur is introduced into the system – witnessed by larger residual resistivities – resulting in much shorter mean free paths.

6.5 Summary

In this chapter, two unexpected findings have been reported. Firstly, evidence for a quantum vortex liquid state has been found in $FeSe_{1-x}S_x$ for both the longitudinal and the transverse field orientations. The irreversibility field H_{irr} and the upper critical field H_{c2}, obtained by high field magnetotransport experiments, do not converge at low temperatures, therefore failing to *close* the vortex liquid regime in the $T = 0\,K$ limit. After considering the contributions of different kinds of fluctuations across the phase diagram, it is argued that nematic fluctuations, coupled with a marked reduction in the pinning energies, could boost the QVL state at S concentrations $x > x_c$. Secondly, in the $\mathbf{H}//ab$ orientation, a small enhancement of H_{c2} above the Pauli limit has been reported for pure FeSe at low temperatures. This effect has been tentatively attributed to the emergence of a FFLO state. The candidacy of FeSe for exhibiting a FFLO state is confirmed by its large Maki parameter and a large value of the ratio between its mean free path and coherence length.

This study suggests that the interplay of distinct fluctuations can lead to the formation of exotic phases, so far observed only in a handful of materials. The limited body of experimental work on these subjects prevents us to draw a conclusive picture, but our findings provide further matter to stimulate new theoretical models.

References

[1] A. A. Abrikosov, *Rev. Mod. Phys.* **76** 3, pp. 975–979 (2004).

[2] J. M. Ziman, *Principles of the theory of solids*, Cambridge University Press (1964).

[3] G. Blatter *et al.*, *Rev. Mod. Phys.* **66** 4, pp. 1125–1388 (1994).

[4] E. Helfand and N. R. Werthamer, *Phys. Rev.* **147** 1, pp. 288–294 (1966).

[5] N. R. Werthamer, E. Helfand and P. Hohenberg, *Phys. Rev.* **147** 1, pp. 295–302 (1966).

[6] Y. Matsuda and H. Shimahara, *J. Phys. Soc. Japan* **76** 051005 (2007).

[7] A. M. Clogston, *Phys. Rev. Lett.* **9** 6, pp. 266–267 (1962).

[8] B. S. Chandrasekhar, *Appl. Phys. Lett.* **1** 1, pp. 7–8 (1962).

[9] P. Fulde and R. A. Ferrell, *Phys. Rev.* **135** 3A, pp. A550–A563 (1964).

[10] A. I. Larkin and Y. N. Ovchinnikov, *Zh. Eksp. Teor. Fiz.* **47**, pp. 1136–1146 (1964). [*Sov. Phys. JETP* **20** 762 (1965)].

[11] L. W. Gruenberg and L. Gunther, *Phys. Rev. Lett.* **16** 22, pp. 996–998 (1966).

[12] J. Wosnitza, *Ann. Phys.* **530** 1700282 (2018).

[13] K. Maki and T. Tsuneto, *Prog. Theor. Phys.* **31** 6, pp. 945–956 (1964).

[14] T. Sasaki *et al.*, *Phys. Rev. B* **66** 224513 (2002).

[15] L. Li *et al.*, *Nat. Phys.* **3**, pp. 311–314 (2007).

[16] P. Husaníková *et al.*, *Phys. Rev. B* **88** 174501 (2013).

[17] Y. Sun, S. Pyon and T. Tamegai, *Physica C* **530**, pp. 55–57 (2016).

[18] S. Kasahara *et al.*, *Nat. Commun.* **7** 12843 (2016).

[19] T. Hanaguri *et al.*, *Phys. Rev. Lett.* **122** 077001 (2019).

[20] C. Kittel, *Introduction to Solid State Physics*, John Wiley & Sons (2005).

[21] A. J. Leggett, *Quantum Liquids*, Oxford University Press (2006).

[22] M. Randeria and E. Taylor, *Annu. Rev. Condens. Matter Phys.* **5**, pp. 209–232 (2014).

[23] T. Terashima *et al.*, *Phys. Rev. B* **90** 144517 (2014).

[24] M. D. Watson *et al.*, *Phys. Rev. B* **91** 155106 (2015).

[25] S. Kasahara *et al.*, *Proc. Natl. Acad. Sci. USA* **111** 46, pp. 16309–16313 (2014).

[26] T. Hanaguri *et al.*, *Sci. Adv.* **4** eaar6419 (2018).

[27] C.-L. Song *et al.*, *Science* **332**, pp. 1410–1413 (2011).

[28] P. O. Sprau *et al.*, *Science* **357**, pp. 75–80 (2017).

[29] R. J. Koch *et al.*, *arXiv* **1902.08732** (2019).

[30] P. Wiecki *et al.*, *Phys. Rev. B* **96** 180502(R) (2017).

[31] V. Grinenko *et al.*, *Phys. Rev. B* **97** 201102(R) (2018).

[32] P. Wiecki *et al.*, *Phys. Rev. B* **98** 020507(R) (2018).

[33] J. P. Sun *et al.*, *Nat. Commun.* **7** 12146 (2016).

[34] K. Matsuura *et al.*, *Nat. Commun.* **8** 1143 (2017).

[35] M. Cyrot and D. Pavuna, *Introduction to Superconductivity and High-T_c Materials*, World Scientific Publishing (1992).

[36] A. Bianchi *et al.*, *Phys. Rev. Lett.* **91** 187004 (2003).

[37] H. A. Radovan *et al.*, *Nature* **425**, pp. 51–55 (2003).

[38] R. Lortz *et al.*, *Phys. Rev. Lett.* **99** 187002 (2007).

[39] B. Bergk *et al.*, *Phys. Rev. B* **83** 064506 (2011).

[40] J. A. Wright *et al.*, *Phys. Rev. Lett.* **107** 087002 (2011).

[41] H. Mayaffre *et al.*, *Nat. Phys.* **10**, pp. 928–932 (2014).

[42] C. C. Agosta *et al.*, *Phys. Rev. Lett.* **118** 267001 (2017).

[43] J. R. Clem, *Physica C* **162-164**, pp. 1137–1142 (1989).

Summary

In this thesis, electrical transport experiments in low temperatures and high magnetic fields on the iron chalcogenide family FeSe$_{1\text{-}x}$S$_x$ ($0 \leq x \leq 0.25$) are presented. The bulk of the work described here has been carried out at the High Field Magnet Laboratory (HFML) in Nijmegen, the Netherlands. By means of two different orientations of the applied field with respect to the studied sample, it was possible to investigate the normal state, the magnetoresistance and the superconducting properties of the material. Because FeSe$_{1\text{-}x}$S$_x$ displays long range nematic order and superconductivity, but not magnetic order in its phase diagram, it has attracted the attention of both theorists and experimentalists and has been employed as a model system to study physical phenomena potentially caused uniquely by nematicity. In particular, it has emerged in the latest years as a candidate for exhibiting quantum critical behaviour. In the introductory chapter of this manuscript (Chap. 1), a general background on Fe-based superconductors is provided. The concepts of nematicity and quantum criticality, crucial for the rest of the book, are also overviewed in a general fashion.

The rest of the thesis is divided in two parts. In part I, the framework of the experiments discussed in part II is built. More in detail, Chap. 2 contains a state of the art of the experimental findings, and their interpretations, on stoichiometric FeSe as well as on its S-substituted series. The evolution of the nematic and superconducting phases with varying x value is treated and the presence of magnetic fluctuations in the system, demonstrated by e.g. the observation of long-range magnetic order under high applied pressure, is discussed.

In Chap. 3, the techniques for sample growth and for preparation of the samples for our magnetotransport experiments are described. The manner whereby in-plane resistivity measurements are performed is explained. The

alignment along two different orientations of the applied field employed during our experiments, namely parallel to the conducting layers of the material ($\mathbf{H}//ab$) and perpendicular to them ($\mathbf{H}//c$), is clarified. The characterization of all measured samples and in particular the determination of their superconducting transition temperature T_c and nematic transition temperature T_s, are shown. T_c is found to be roughly constant around 8-10 K, while T_s is gradually lowered by S-doping until it is suppressed to 0 K at $x_c \approx 0.16$, in accordance to the existing literature.

Part II consists of three experimental chapters. Each of them has a specific focus but their collection gives a consistent picture of the (magneto-) transport properties of $FeSe_{1-x}S_x$ across the studied portion of its x-T phase diagram. In Chap. 4, the $\mathbf{H}//ab$ measuring configuration was employed to suppress superconductivity (SC) with 35 T static magnetic fields, while minimizing the magnetoresistance (MR) of the sample and therefore being able to study the behaviour of its normal-state resistivity (ρ) below T_c. The limiting low-temperature dependence of the resistivity is found to be quadratic – as expected in a correlated Fermi-liquid – for all studied sulphur concentrations except $x = 0.16$, where $\rho \propto T$ down to the lowest temperature ($T \approx 1.5\,\mathrm{K}$) at which SC could be suppressed with the available field strength. This observation of non-Fermi-liquid resistivity in $FeSe_{0.84}S_{0.16}$, paired with a strong enhancement of the effective mass as inferred from the magnitude of the T^2-coefficient of the resistivity A, points towards the existence of a quantum critical point (QCP) at $x = x_c = 0.16$. This is the first experimental evidence for nematic-induced quantum criticality through electrical transport measurements. Moreover, the magnitude of the measured T-linear resistivity inside the quantum critical fan suggests that charge transport in $FeSe_{1-x}S_x$ is close to the so-called Planckian dissipation limit where the relevant energy scales can all be reduced to k_BT.

Chap. 5 contains measurements of the transverse (i.e. in the $\mathbf{H}//c$ configuration) MR of $FeSe_{1-x}S_x$ in magnetic field strengths up to 38 T. The raw MR is found to strongly violate Kohler's scaling rule which applies to conventional metals, nor does it follow the quadrature scaling recently discovered in other quantum critical systems, such as $BaFe_2(As_{1-x}P_x)_2$ (Ba122), close to their QCP. However, we report the discovery of two independent MR components. One of them exhibits a conventional H^2 behaviour all the way up to 38 T, while the other one has the precise quadrature form found in Ba122. In fact, once appropriately renormalized,

this quantum critical (QC) component is found to scale both with varying temperature, at a fixed x level, and with varying x when the temperature is fixed. The quadrature form of the QC component is followed to a very high degree of precision across the phase diagram, not only at or in close proximity to the QCP. The relative strength of the observed QC component peaks at the QCP itself. The comparison with a sample with a higher level of disorder reveals an interesting dependence of the two MR components on the impurity scattering. With increasing disorder, the conventional (orbital) H^2 component disappears, raising the prospect that the coexistence of the two MR components – observed in $FeSe_{1-x}S_x$ – might have been hidden in other systems by disorder.
In Chap. 6, the evolution of the irreversibility field H_{irr} and the upper critical field H_{c2} of $FeSe_{1-x}S_x$ is followed down to very low temperatures (~0.3 K), by applying magnetic fields up to 38 T in both orientations $\mathbf{H}//ab$ and $\mathbf{H}//c$. The focus of the chapter is on the exploration of the vortex liquid (VL) phase, that is the intermediate region of the T-H phase diagram of type-II superconductors where the vortices are already depinned but the superconductivity in the material has not yet been fully destroyed. The VL phase, although it can be broad at finite temperatures, is generally expected to disappear in the 0 K limit, implying that H_{irr} and H_{c2} eventually converge. In $FeSe_{1-x}S_x$, we report the persistence of a broad VL state down to the lowest measured temperatures, providing strong evidence for the development of a quantum vortex liquid (QVL) state at the effective zero-temperature axis, for x values outside of the nematic phase. The origin of this effect is believed to be the persistence of nematic fluctuations at S concentrations far from the nematic phase, coupled with a weakening of the superconducting pairing strength. Finally, in pure FeSe for $\mathbf{H}//ab$, a sharp increase of H_{c2} is reported below 1.35 K. The appearance of this phenomenon, together with the fulfilment of several criteria dictated by theory, is consistent with the formation of a modulating superconducting state surviving at very high fields, the so-called FFLO state.

The present manuscript comprises a systematic study of the low-T electronic properties of the series $FeSe_{1-x}S_x$ with $0 \leq x \leq 0.25$. The main findings, summarized above, provide a wide-angle perspective on the behaviour of the system across its nematic quantum critical point. Despite the fact that electrical transport experiments involve no particularly sophisticated techniques – they crudely consist in attaching electrical contacts to a sample and measuring its resistance – their careful realization on $FeSe_{1\text{-}x}S_x$, systematically measuring several samples in a wide range of S-doping and in different experimental conditions, allowed us to obtain a large spectrum of results. However, further theoretical and experimental efforts will be needed to explain them fully. In this spirit, future experiments on the Hall effect should be carried out to shed more light on the strange metallic nature of this materials series, and allow to test the realization of the modified Kohler's scaling across the QCP. Chap. 5 calls almost naturally for a study of the disorder-dependent evolution of the quantum critical properties in diverse materials. Another revealing experiment would be the exploration of the quantum critical behaviour in the transport properties of $FeSe_{1\text{-}x}S_x$ as a function of both varying sulphur doping and increasing pressure p. The main advantage of such an experiment would be the possibility to separate the nematic phase from the p-induced spin-density wave state, as seen in Chap. 2. A second QCP of magnetic origin might be found in the p-axis, whose features could be compared to the observed magnetic QCP in the Fe-pnictides. Moreover, in the hole-doped cuprates for example, the non-standard behaviour observed in proximity to the putative QCP at the end point of their pseudogap phase is very different and could be rather due to a progressive destruction of the quasiparticles with decreasing hole-doping, as proposed in our recent review[1]. However, the character of the observed T-linear resistivity, as suggested by the approximation to the Planckian dissipation limit, might be common to all these materials. Therefore, in conclusion, future studies should focus on the strange metallic behaviour to understand its very origin.

---

[1] N. E. Hussey, J. Buhot and S. Licciardello, *Rep. Prog. Phys.* **81** 052501 (2018).

Samenvatting

In dit proefschrift worden elektrische transport experimenten op de ijzer chalcogenide familie FeSe$_{1\text{-}x}$S$_x$ ($0 \leq x \leq 0.25$) in lage temperaturen en hoge magnetische velden gepresenteerd. Het grootste deel van het hier beschreven werk is uitgevoerd aan het High Field Magnet Laboratory (HFML) te Nijmegen, Nederland. Door twee verschillende orientaties van het toegepaste magnetische veld met betrekking tot het bestudeerde monster, is het mogelijk geweest om de normale toestand, de magnetoweerstand en de supergeleidingseigenschappen van het materiaal te onderzoeken. Aangezien FeSe$_{1\text{-}x}$S$_x$ lange afstand nematische orde en supergeleiding, maar geen magnetische orde in zijn fasediagram toont, heeft het de interesse van zowel theoretisch als experimenteel natuurkundigen aangetrokken om een modelsysteem te worden voor de studie van potentieel alleen door de nematische fase veroorzaakte fenomenen. In het bijzonder is dit materiaal in de laatste jaren te voorschijn gekomen als kandidaat voor het vertonen van kwantum kritisch gedrag. In het inleidende hoofdstuk van dit manuscript (hoofdstuk 1), wordt een algemene achtergrond over op Fe gebaseerde supergeleiders gegeven. Er wordt ook een algemeen overzicht van de concepten van nematiciteit en kwantum kritikaliteit gegeven, die voor de rest van het boek noodzakelijk zijn.

De rest van dit proefschrift wordt in twee delen verdeeld. In deel I wordt het kader gebouwd voor de experimenten waar deel II over gaat. In meer details, bevat hoofdstuk 2 een actueel overzicht van de experimentele bevindingen, en de overeenkomstige interpretaties, over zowel stoichiometrische FeSe en FeSe$_{1\text{-}x}$S$_x$ met $x \neq 0$. De ontwikkeling van de nematische en supergeleidende fasen als een functie van x wordt bestudeerd en de aanwezigheid van magnetische fluctuaties in het systeem, die gedemonstreerd zijn door bijv. de observatie van lange afstand magnetische orde onder

hoge toegepaste druk, wordt bediscussieerd.
In hoofdstuk 3, worden de technieken voor de monstergroei en voor de voorbereiding van de monsters voor onze magnetotransport experimenten beschreven. De manier waarop de afmetingen van de in-het-vlak soortelijke weerstand uitgevoerd zijn, wordt uitgelegd. Het uitlijnen langs de twee verschillende orientaties van het toegepaste veld, die tijdens onze experimenten gebruikt zijn, wordt toegelicht, namelijk parallel ($\mathbf{H}//ab$) en loodrecht ($\mathbf{H}//c$) op de geleidende lagen van het materiaal. De karakterisering van alle gemeten monsters en in het bijzonder de bepaling van hun supergeleidende (T_c) en nematische (T_s) overgangstemperatuur, worden beschreven. T_c is ongeveer constant rond 8-10 K, terwijl T_s door S-dotering geleidelijk verlaagd wordt totdat hij bij $x_\mathrm{c} \approx 0.16$ tot 0 K onderdrukt wordt, in overeenstemming met de bestaande literatuur.

Deel II bestaat uit drie experimentele hoofdstukken. Elk heeft een specifieke focus maar ze stellen een consistent beeld samen van de (magneto-) transport eigenschappen van $\mathrm{FeSe}_{1\text{-}x}\mathrm{S}_x$ met betrekking tot het bestudeerde deel van zijn x-T fasediagram. In hoofdstuk 4 wordt de meetconfiguratie $\mathbf{H}//ab$ gebruikt om de supergeleiding (SC, uit het engelse woord *superconductivity*) door middel van statische magnetische velden van 35 T uit te schakelen, terwijl de magnetoweerstand (MR, engels *magnetoresistance*) van het monster geminimalizeerd wordt. Op die manier was het mogelijk om de soortelijke weerstand (ρ) in de normale toestand te bestuderen onder T_c. De limietsvorm van de soortelijke weerstand bij lage temperaturen is kwadratisch – zoals verwacht voor een gecorreleerde Fermi-vloeistof – voor alle onderzochte zwavelconcentraties behalve $x = 0.16$, waarvoor $\rho \propto T$ tot de laagste temperatuur ($T \approx 1.5\,\mathrm{K}$) waarbij SC kon worden uitgeschakeld door middel van de beschikbare veldssterkte. Deze observatie van non-Fermi-vloeistof-achtige soortelijke weerstand in $\mathrm{FeSe}_{0.84}\mathrm{S}_{0.16}$, gekoppeld met een sterke toename van de effectieve massa die afgeleid is door de grootte van het T^2-coëfficiënt van de soortelijke weerstand A, wijst naar het bestaan van een kwantum kritisch punt (QCP, engels *quantum critical point*) voor $x = x_\mathrm{c} = 0.16$. Dit is het eerste experimentele bewijs van nematisch-geïnduceerde kwantum kritikaliteit door elektrische transport experimenten. Bovendien suggereert de grootte van de gemeten T-lineaire soortelijke weerstand binnen de kwantum kritische waaier dat de ladingstransport in $\mathrm{FeSe}_{1\text{-}x}\mathrm{S}_x$ dichtbij de zogenaamde Planckse dissipatie limiet ligt, waar alle relevante energieschalen tot $k_\mathrm{B}T$ kunnen worden

teruggebracht.
Hoofdstuk 5 bevat metingen van de transversale (d.w.z. in de configuratie $\mathbf{H}//c$) MR van $\mathrm{FeSe}_{1\text{-}x}\mathrm{S}_x$ in magnetische velden tot en met 38 T. De onbewerkte MR overtreedt sterk de schalingsregel van Kohler, die voor conventionele metalen geldt, noch volgt de kwadratuur schalingsrelatie die recent dichtbij de QCP van andere kwantum kritische systemes, bijv. $\mathrm{BaFe}_2(\mathrm{As}_{1\text{-}x}\mathrm{P}_x)_2$ (Ba122), werd ontdekt. Echter melden wij de ontdekking van twee onafhankelijke componenten van de MR. De ene heeft een conventioneel H^2 gedrag tot 38 T, terwijl de andere dezelfde kwadratuurvorm, die voor Ba122 geldt, volgt. Door een passende renormalisatie verschaalt deze kwantum kritische (QC, engels *quantum critical*) component zowel als een functie van de temperatuur, bij vaste zwavelconcentratie, als als een functie van de zwavelconcentratie, bij vaste temperatuur. De kwadratuurvorm wordt met hoge precisie gevolgd niet alleen op of dichtbij de QCP, maar overal in de bestudeerde portie van het fasediagram. De relatieve sterkte van de waargenomen QC component is gemaximaliseerd bij de QCP. Door de vergelijking met een monster met een hoger niveau van wanorde konden we een interessante afhankelijkheid van de twee componenten van de MR door de verontreinigingsverstrooiing ontdekken. Hoe hoger de wanorde, hoe zwakker de conventionele H^2 component; in het monster met hogere wanorde verdwijnt deze component volledig dus deze observatie stelt dat het gelijktijdig bestaan van de twee componenten van de MR – in $\mathrm{FeSe}_{1\text{-}x}\mathrm{S}_x$ waargenomen – in andere systemes waarschijnlijk door wanorde verborgen is.
In hoofdstuk 6 wordt de ontwikkeling van het onomkeerbaarheidsveld H_{irr} (engels *irreversibility field*) en van het tweede kritische veld H_{c2} (engels *upper critical field*) tot hele lage temperaturen (~0.3 K) bestudeerd door middel van magnetische velden tot 38 T, toegepast in beide orientaties $\mathbf{H}//ab$ en $\mathbf{H}//c$. Het hoofdstuk focust op de verkenning van de *vortex* vloeistof fase (VL, engels *vortex liquid*), wat de tussenliggende regio van het T-H fasediagram van een type-II supergeleider is, waar de *vortices* al onthecht zijn maar de supergeleiding in het materiaal nog niet volledig afgebroken is. Hoewel de VL fase bij eindige temperaturen breed kan zijn, zal hij in de 0 K limiet meestal verdwijnen zodat H_{irr} en H_{c2} gaan convergeren. Wij melden de hardnekkigheid van een brede VL toestand in $\mathrm{FeSe}_{1\text{-}x}\mathrm{S}_x$ tot de laagst gemeten temperaturen. Dit levert sterk bewijs voor de ontwikkeling van een kwantum vortex vloeistof (QVL, engels *quantum vortex liquid*) toestand op de effectieve nul-temperatuur as, voor waarden van x buiten de nematische

fase. De oorsprong van dit effect ligt waarschijnlijk in de combinatie van twee verschijnselen: de hardnekkigheid van nematische fluctuaties bij S concentraties die ver weg van de nematische fase zijn en het verzwakken van de supergeleidende bindingssterkte. Ten laatste melden we een scherpe stijging van H_{c2} onder 1.35 K. De manifestatie van dit verschijnsel en de vervulling van verschillende criteria opgelegd door de theorie, hangen samen met de vorming van een modulerende supergeleidende toestand die tot heel hoge velden in stand blijft, de zogenaamde FFLO toestand.

Dit manuscript bevat een systematische studie van de elektronische eigenschappen bij lage temperaturen van de serie FeSe$_{1\text{-}x}$S$_x$ met $0 \leq x \leq 0.25$. De hoofdbevindingen, hier samengevat, geven een breed perspectief over de gedragingen van het systeem aan beide kanten van zijn kwantum kritisch punt. Ondanks het feit dat elektrische transport experimenten niet bijzonder verfijnd zijn – ze kunnen uitgevoerd worden door het simpelweg bevestigen van elektrische contacten aan een monster en door het meten van zijn weerstand – heeft hun zorgvuldige realisatie op verschillende monsters van FeSe$_{1\text{-}x}$S$_x$, met meerdere zwaveldoteringen en in diverse experimentele omstandigheden, ons toegestaan om een groot spectrum van resultaten te krijgen. Verder theoretisch en experimenteel werk zal niettemin nodig zijn om een complete verklaring van deze resultaten te bereiken. In deze richting zullen in de toekomst Hall effect experimenten uitgevoerd worden om een diepere kennis over het vreemde metaalachtige karakter van dit materiaal te krijgen en om de gewijzigde schalingsregel van Kohler (engels *modified Kohler's scaling*) dwars door de QCP te testen. Het natuurlijke vervolg van hoofdstuk 5 zou een studie naar de ontwikkeling, als een functie van wanorde, van de kwantum kritische eigenschappen in verschillende materialen zijn. Meer inzicht in de transportseigenschappen van FeSe$_{1\text{-}x}$S$_x$ zou behaald kunnen worden door het veranderen van zowel de zwavelconcentratie als de druk p tijdens hetzelfde experiment. Het grootste voordeel van zo'n experiment zou de mogelijkheid zijn om de nematische fase en de p-geïnduceerde spin-density wave fase van elkaar te scheiden, zoals in hoofdstuk 2 is uitgelegd. Een tweede QCP met magnetische oorsprong zou kunnen worden gevonden in de p-as; zijn kenmerken zouden kunnen worden vergeleken met degenen van het magnetische QCP in de Fe-pnictides. Verder, bijvoorbeeld in de gat-gedoteerde cupraten, zijn de bijzondere gedragingen die dichtbij het vermeende QCP aan het einde van hun pseudogap fase waargenomen zijn, heel anders en worden waarschijnlijk door een geleidelijke afbraak van de quasideeltjes met afnemende gat-dotering veroorzaakt, zoals in ons recente overzichtsartikel[1] wordt voorgesteld. Toch zouden de eigenschappen van de geobserveerde T-lineaire weerstand in al deze materialen dezelfde kunnen zijn, zoals door de benadering tot de Planckse dissipatie limiet wordt gesuggereerd. Dus ter conclusie, toekomstige studies zouden op de vreemde metaalachtige gedragingen moeten focussen om hun echte oorsprong te begrijpen.

---

[1] N. E. Hussey, J. Buhot and S. Licciardello, *Rep. Prog. Phys.* **81** 052501 (2018).

Acknowledgements

So it is finally done. I have completed my PhD project and managed to encompass it in this thesis. It has certainly been quite a ride. I can safely say that this ride would not have been possible without the support and help that I got through the years from several people; without acknowledging them, I would feel like if this book were somehow incomplete.

I remember when I first began my journey at the HFML as a fresh PhD student, having to deal with a whole new world of scientific research. From that very starting point, up until the end of my contract four years later, I was lucky to be supervised by Nigel, who was always there to patiently teach me the art of electric transport, to transfer to me part of his immense knowledge and expertise in the field, to bring me back on track when I was wandering about and to even measure with me during some exhausting magnet-time shifts (a prof. in the lab? Yes, it's a thing!). He has been a guide and a great co-worker rather than a boss.

Of course, the contribution of a team of scientists who I carried out all my experiments with, was fundamental for this thesis. Jonathan, Jake, Jianming, Matija and all the other co-authors of my first-author papers (see List of publications) well deserve to be on this page.

During the first year of my PhD project, I could benefit from the help of Saman who introduced me to the everyday lab life and made me familiar with superconductor magnets and with the high field installation.

It would be impossible to do science at the HFML without the daily work of a team of specialized engineers and technicians who basically make the facility running. In particular, essential in these years have been Lijnis and Michel for solving all sort of problems with the probes, Frans and Arjan for their prompt help with installation problems during experiments, Peter Albers for being a joker a bit for everything, Frits for the whole lot of helium and Hung for all the IT stuff (and for the laughter).

To the administrative staff – Martin, Ine and Thera – thanks for taking care of the paperwork and all organizational matters (I could not imagine having to do that myself).

Furthermore, there are many other people who did not support me directly with my research and work, but certainly have been an important part of my PhD.
The office 01-35 has been an awesome place to spend long days of data analysis and papers/thesis writing. Francesca, it was great to sit next to you and benefit from your help with Dutch and Italian. Maarten van Delft, despite your quiet presence, you gave a sort of special aura to the office, and you definitely were the real Dutch expert in there. Marion, thank you for showing mercy and only injuring me when you could have killed me, and for our very useful conversations in Dutch. Jonathan, your *ça m'énerve* and your good stories have been unmissable ingredients in our office's recipe. Anatol, the small guy with a big luck in table football and the one always able to see the glass half full. Thanks to both of you guys for your valuable help in Dutch...ah, no. Maryam, we incited each other during the months of thesis writing and we both reached try.
Commissione borrelli, how many billions of euros did we spend in food and drinks through the years? I am glad it was not our own money. Laurens, Thomas, Mariana and Bryan, it was fun to deep-fry things together, prepare surreal presentations and quizzes for the christmas parties, dress up as *zwarte Piet* and invent new ways of borrelling.
Sergio, I enjoyed listening to your bizarre musical tips and mutually trading magnet-time.
Fabio, you have been like a flashback to my student life, awakening all those dormant but good Erasmus feelings.
Lucas, Alex, Andrea, Maarten Berben, Dima and adopted Bence – your office was second only to ours. If I wanted to take a walk and breath some different air, that was the place to go. A real living room corner, bowls of *pepernoten* all year round, a miniature rugby ball and a lot of exhausted batteries: what could you possibly want more?
And of course to many other colleagues, even though I don't mention them all here: it has been nice to be part of the same "house" and share many coffee and lunch breaks. It has indeed been quite a ride.

List of publications

- **S. Licciardello**, J. Buhot, J. Lu, J. Ayres, S. Kasahara, Y. Matsuda, T. Shibauchi and N. E. Hussey, "Electrical resistivity across a nematic quantum critical point", *Nature* **567**, pp. 213–217 (2019).
- **S. Licciardello**, N. Maksimovic, J. Ayres, J. Buhot, M. Čulo, B. Bryant, S. Kasahara, Y. Matsuda, T. Shibauchi, V. Nagarajan, J. G. Analytis and N. E. Hussey, "Coexistence of orbital and quantum critical magnetoresistance in $FeSe_{1\text{-}x}S_x$", submitted. Preprint at *arXiv* **1903.05679** (2019).
- **S. Licciardello**, M. Čulo, S. Kasahara, Y. Matsuda, T. Shibauchi and N. E. Hussey, "Possible evidence for a quantum vortex liquid in $FeSe_{1\text{-}x}S_x$", in preparation.
- J. Lu, X. Xu, M. Greenblatt, R. Jin, P. Tinnemans, **S. Licciardello**, M. R. van Delft, J. Buhot, P. Chudzinski and N. E. Hussey, "Emergence of a real-space symmetry axis in the magnetoresistance of the one-dimensional conductor $Li_{0.9}Mo_6O_{17}$", *Sci. Adv.* **5** eaar8027 (2019).
- N. E. Hussey, J. Buhot and **S. Licciardello**, "A tale of two metals: contrasting criticalities in the pnictides and hole-doped cuprates", *Rep. Prog. Phys.* **81** 052501 (2018).
- C. Putzke, J. Ayres, J. Buhot, **S. Licciardello**, N. E. Hussey, S. Friedemann and A. Carrington, "Charge order and superconductivity in underdoped $YBa_2Cu_3O_{7\text{-}\delta}$ under pressure", *Phys. Rev. Lett.* **120** 117002 (2018).
- S. Ghannadzadeh, **S. Licciardello**, S. Arsenijević, P. Robinson, H. Takatsu, M. I. Katsnelson and N. E. Hussey, "Simultaneous loss of in-

terlayer coherence and long-range magnetism in quasi-two-dimensional $PdCrO_2$", *Nat. Comm.* **8** 15001 (2017).

- C. Collignon, S. Badoux, S. A. A. Afshar, B. Michon, F. Laliberte, O. Cyr-Choiniere, J. S. Zhou, **S. Licciardello**, S. Wiedmann, N. Doiron-Leyraud and L. Taillefer, "Fermi-surface transformation across the pseudogap critical point of the cuprate superconductor $La_{1.6\text{-}x}Nd_{0.4}Sr_xCuO_4$", *Phys. Rev. B* **95** 224517 (2017).

Curriculum Vitae

Salvatore Licciardello

1989	Born on May, 24th in Catania, Italy
2002-2007	High school diploma (marks 100/100) at Liceo Classico "Gulli e Pennisi", Acireale, Italy
2007-2011	Bachelor of Science in Physics (marks 110/110 cum laude) at Università degli studi di Catania, Italy
2011-2014	Master of Science in Condensed Matter Physics (marks 110/110) at Università degli studi di Catania, Italy
2015-2019	Ph.D. researcher at the High Field Magnet Laboratory in the Strongly Correlated Electron Systems group under the supervision of prof. dr. Nigel E. Hussey, Radboud University, Nijmegen, the Netherlands